UNIVERSITY OF SOUTHAMPTON

FACULTY OF NATURAL AND ENVIROMENT SCIENCES

Chemistry

High Voltage Positive Electrodes for High Energy Lithium-ion Batteries

by

Michael Graham Palmer

Thesis for the degree of Doctor of Philosophy

May 2016

DECLARATION OF AUTHORSHIP

I, Michael Graham Palmer declare that this thesis and the work presented in it are my own and has been generated by me as the result of my own original research.

High Voltage Positive Electrodes for High Energy Lithium-ion Electrodes

I confirm that:

1. This work was done wholly or mainly while in candidature for a research degree at this University;
2. Where any part of this thesis has previously been submitted for a degree or any other qualification at this University or any other institution, this has been clearly stated;
3. Where I have consulted the published work of others, this is always clearly attributed;
4. Where I have quoted from the work of others, the source is always given. With the exception of such quotations, this thesis is entirely my own work;
5. I have acknowledged all main sources of help;
6. Where the thesis is based on work done by myself jointly with others, I have made clear exactly what was done by others and what I have contributed myself;
7. [Delete as appropriate] None of this work has been published before submission [or] Parts of this work have been published as: [please list references below]:

Signed:.....

Date: .....

Abstract

Lithium-ion high voltage cathode materials are discussed within this thesis, with $LiCoPO_4$ as a composite electrode evaluated for use as the active compound within lithium half-cells. A comprehensive literature review on lithium containing cathode materials with a focus on high voltage materials is provided. The majority of the materials within this work were synthesised using solvothermal techniques, which were characterised through XRD and SEM. Composite type electrodes were prepared through mainly using PTFE as the binder material, and different electrolytes were also investigated.

Composite electrodes were electrochemically evulated with competitive capacites obtained compared to the literature. The performance of the $LiCoPO_4$ composite electrodes was found to be significantly different and attributed to the use of different synthesis solvents and heating conditions used for synthesis. The rate performance and electrochemical cycling was found to depend highly on the surface area and particle size of the composite electrode. XANES and *in-situ* XRD was performed at Diamond Light Source (UK synchrotron), where the $LiCoPO_4$ charge profile was fully characterised. It was found that $LiCoPO_4$ undergoes transient lattice parameter changes during charging, and that phase recovery during any relaxations was observed.

Acknowledgements

Firstly, I would like to thank my supervisors; Professor John Owen and Professor Andrew Hector and also Doctor Nuria Garcia-Araez for their help and support throughout my time at Southampton University. Without their advice, guidance and friendship this thesis would not be possible. I would like to thank the Southampton University staff used to place me into Electrochemistry for my 3rd year undergraduate project, although my former self as a keen organic chemist at the time may not agree.

I would like to extend my graditude to the past and present members of the Owen and Hector group, as well as the whole of the Southampton Electrochemistry Group, who have always been a great help. I have had great experiences at different conferences around the world and I want to show my appreciation to all the people I was with, making each conference memorable.

I would like to thank QinetiQ and the EPSRC for funding this research and Dr. Girts Vitins, Dr. Gary Mepsted and Dr. Thierry Le Gall for their support and useful discussions. After many vital (and sometimes pointless) trips to the Diamond Light Source, I would like to thank Dr. Jonathan Rawl, and Dr. Chris Nicklin for their help during relentless *in-situ* XRD studies.

My acknowledgements section would not be complete without thanking all of my friends for offering me great distractions away from a PhD. I would like to thank all members of Friday's 4 o'clock club for taking me around the world, and onto the Edge of glory.

Finally, a special thanks go to my family and to Dominika, who have always been very supportive and trusting me to just get on with it. Although, it is about time I got a job.

List of Symbols

A = Area of electrode (cm^2)
C = Capacitance (F)
C = C-rate (h^{-1})
C_{dl} = Double layer capacitance (F)
D = Diffusion coefficient ($cm^2\ s^{-1}$)
d = Distance between crystal planes (m)
E = Cell potential (V)
e = Charge of an electron (1.602×10^{-19} C)
E_0 = Amplitude (variable units)
F = Faradays constant (96485 C mol^{-1})
f = Frequency (Hz)
G = Gibbs free energy (kJ mol^{-1})
h = Planck's constant ($6.626 \times 10^{-34}\ m^2\ kg\ s^{-1}$)
I = Current (A)
i = $\sqrt{-1}$
M = Mass of active material (g)
M_w = Molecular mass of material (g)
n = Number of electrons
$Q_{Measured}$ = Measured capacity (mA h)
$Q_{Specific}$ = Specific capacity (mA h g^{-1})
QT = Theoretical capacity (mA h g^{-1})
R = Resistance (Ω)
R_{ct} = Charge transfer resistance (Ω)
R_u = Uncompensated resistance (Ω)
t = Time (s)
V = Accelerating voltage (V)
Z = Impedance (Ω)
Z′ = Real component of impedance (Ω)
Z′′ = Imaginary component of Impedance (Ω)
μ = Chemical potential (J mol^{-1})
μ = Refractive index
θ = Incident angle (degrees)
λ = Wavelength (m)
σ = Conductivity of electrolyte (S m^{-1})
ω = Radial frequency (rad s^{-1}) or (2πf)
ϕ = Phase shift

List of Abbreviations

AC – Alternating current
AFM – Atomic force microscopy
BET - Brunauer–Emmett–Teller (surface area calculation method)
BSE – Back scattered electrons
CPE – Constant phase element
CV – Cyclic Voltammetry
DEC – Diethyl carbonate
DEG – Diethylene Glycol
DMC – Dimethyl carbonate
DME – Dimethoxy ethane
EC - Ethylene carbonate
EDS – Energy dispersive X-ray spectroscopy
EIS – electrochemical impedance spectroscopy
EMC – Ethyl methyl carbonate
FEC – Fluoroethylene carbonate
HF – Hydrofloric acid
ICSD – Inorganic Crystal Structure Database
LIB – Lithium-ion battery
$LiBF_4$ – Lithium tetrafluoroborate
LiBob – Lithium bis(oxalate)borate
LiF – Lithium fluoride
LP57 – Electrolyte solution of 1 M $LiPF_6$ in EC: EMC (3:1, w/w)
$LiPF_6$ – Lithium hexafluorophosphate
NMP – N-methyl-2-pyrrolidone
OCV – Open circuit potential
PC – Propylene carbonate
ppm – Parts per million
PFA – Perfluoroalkoxy alkanes
PTFE – Polytetrafluoroethylene
PVDF – Poly-vinylidene fluoride
rpm – Rotations per minute
RuO_2 – Ruthenium Oxide
SE – Secondary electrons
SEI – Solid electrolyte interphase
SEM – Scanning electron microscopy (microscope)
TMS – Tetramethylene sulfone
TMSP – Tris(trimethylsilyl)phosphate
VMP – Variable multi-channel potentiostat
XRD – X-ray diffraction

Table Of Contents

Chapter 1:

Aims, Background and Introduction

1.1 Project Context

The demand for a sustainable, clean, cost effective and high energy density power source has driven the battery materials market for the last 60 years. The high gravimetric and volumetric energy density of lithium-ion systems allows for the production of compact lightweight batteries for portable electronic devices such as mobile phones, laptop computers and power drills.

The new advances in mobile phone technology and the ultimate goal of economically viable electric vehicles provide the demand for the development of new higher energy density battery systems. Over the last 25 years, lithium-ion batteries utilising traditional materials have improved, but are reaching a practical limit in terms of energy density.

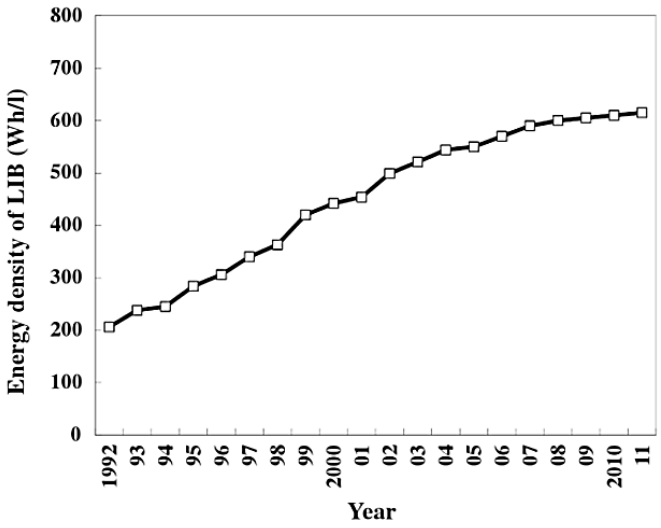

Figure 1.1 - Energy density of lithium-ion batteries between 1992 and 2011, reproduced from reference[1] with permission.

Research into new lithium-ion battery systems is a necessity to allow for batteries with higher energy densities to be realised. The positive electrode is a crucial component which needs to be addressed as it has a low capacity return compared to the negative electrode. For a given amount of charge, a higher voltage directly relates to more energy being stored. High voltage cathode materials are of great interest in terms of advancing the electrochemical market and developing the next generation of lithium-ion batteries.

1.2 Aims and Objectives

The aim of this project was to investigate materials to act as the positive electrode for high voltage lithium-ion batteries. The project was started after consideration of a number of systems, before focussing on $LiCoPO_4$ as a positive electrode material.

The work aimed to synthesise, characterise and electrochemically test $LiCoPO_4$ and modify the system in various ways to study the differences which may occur. Initially the composite electrode was optimised, and the best working electrode was selected for further studies. Different electrochemical techniques were used to probe the system, whilst suggesting why certain behaviour was observed under certain conditions with sound reasoning. Synchrotron beam time gathered vital information into how the system operates, with proof of concept ideas analysed.

1.3 Background

1.3.1 Brief History of Lithium-ion Development

Lithium is the lightest (equivalent weight of 6.94 g mol^{-1}) and most electropositive metal, that provides the largest specific energy per weight for energy storage systems.[2] The overwhelming appeal of lithium-ion electrochemistry lies in its small ionic radius and low redox potential which are ideal properties for solid state diffusion. The advantage of using lithium metal was first demonstrated in the 1970s with the assembly of primary lithium cells which were power sources for watches and implantable medical devices.[3] During this time period, the concept of electrochemical intercalation and its potential use in battery systems became increasingly defined.

In 1972, Exxon focussed on a project involving TiS_2 as the positive electrode, lithium metal as the negative electrode and lithium perchlorate in 1-3-dioxolane as the electrolyte which attracted significant interest and was initially researched by M. Stanley Whittingham.[3] The structure of TiS_2 comprises of layers of hexagonal close-packed octahedral atomic groups, formed by a layer of titanium atoms between two layers of sulphur atoms.[4] Rechargeable batteries with lithium metal as the anode were able to provide high energy densities; however it was discovered in the mid-1980s that a lithium metal/liquid electrolyte combination led to unwanted dendrite formation during cycling.[5] Dendrite formation is the random growth (characteristically tree-like) of lithium metal fibres on the surface of the lithium metal electrode due to lithium plating. The continuous growth of these fibres during cycling can bridge the gap between the positive and the negative electrode which could lead to short-circuiting within the cell. A combination of a short circuits coupled with volatile flammable organic electrolytes could lead to fire hazards.

The inherent instability of lithium metal led to the development of non-metallic intercalating negative electrodes, leading to the development of the modern 'lithium-ion' or 'rocking chair' battery. In 1991 SONY™ introduced the first commercial lithium-ion battery, which consisted of $LiCoO_2$ as the positive electrode, soft carbon as the negative electrode and an electrolyte of 1 M $LiPF_6$ in a mixture of propylene carbonate (PC) and diethyl carbonate (DEC).[6] Because lithium was in its ionic state

rather than its metallic state, the dendrite problem was overcome, making lithium-ion cells safer than lithium-metal cells.

Within the structure of $LiCoO_2$, lithium ions form layers between CoO_2 sheets which contain edge shared CoO_6 octahedra. The lithium ions occupy octahedral sites between the CoO_2 layers allowing for two dimensional lithium transport pathways parallel to the layered structure with octahedral Co^{3+} ions (d^6) in a low spin state. Upon charge, lithium removal results in the formation of Co^{4+} (d^5). This cathode material can provide a working voltage of ~ 4 V *vs.* Li/Li^+.[7]

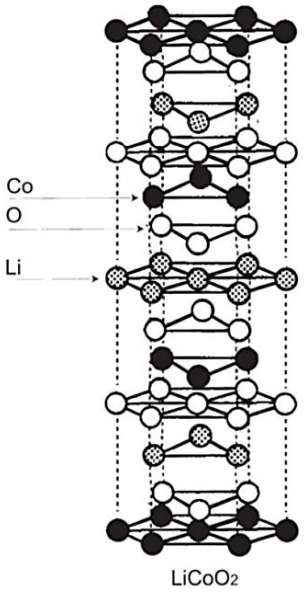

Figure 1.2 – Layered structure of $LiCoO_2$. Reproduced from reference[8] with permission.

The use of graphitic carbon was a breakthrough for use as a lithium negative electrode.[9] Reversible intercalation of lithium ions into graphite initially experienced problems of exfoliation caused by co-intercalation of electrolyte solvent molecules between the layers of graphite. A stable passivation layer was formed on the surface of graphite by the decomposition of ethylene carbonate (EC) as an electrolyte solvent. This layer prevented both further solvent intercalation and further solvent decomposition.[10] Graphite has a greater charge storage capacity and operates at a lower voltage compared to soft carbons.

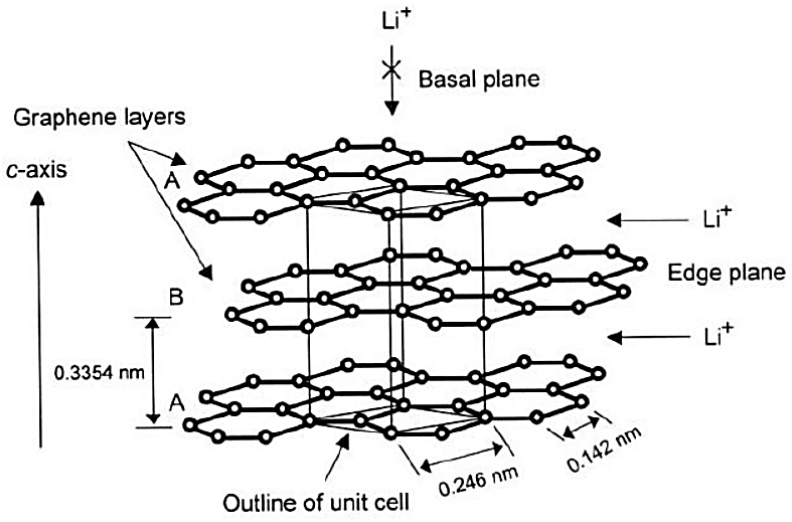

Figure 1.3 – Hexagonal crystal structure of graphite showing the ABAB stacking of graphene sheets and the unit cell. Reproduced from reference[11] with permission.

Lithium-ion batteries are constructed in the discharged state with lithium embedded into the positive $LiCoO_2$ structure. The battery must first be charged, whereby lithium ions are partially extracted from the positive electrode and inserted into the graphite negative electrode. Since then lithium-ion batteries have been recognised as high energy and high operation voltage rechargeable power sources by outperforming other available battery systems.[12]

1.4 Battery Fundamentals

1.4.1 Cell Voltage

Voltage can be defined as the work required to move 'charge' between two points. The voltage of a cell is related to the Gibbs free energy of the redox reaction.[7] When a redox reaction occurs, there is a change in the free energy of the system, and a subsequent change in cell voltage as the reactants are converted into products described by **Equation 1.0**. A redox reaction occurs due to the electrochemical potential that is setup between the positive and negative electrode. The tendency for a reaction to reach equilibrium is driven by the Gibbs free energy (ΔG), and has been defined by the relationship;

$$\Delta G = -nFE \qquad \textbf{Equation 1.0}$$

ΔG = change in free energy (J mol^{-1}), n = number of electrons, F = Faradays constant (96485 C mol^{-1}), E = Potential (V)

The potential is related to the thermodynamic driving force for the reaction. **Equation 1.0** can be related to a lithium-ion cell using **Equation 1.1**; the free energy can be expressed in terms of the chemical potential of lithium.[7]

$$\partial G = (\mu_{Li}^{+} - \mu_{Li}^{-}) \qquad \textbf{Equation 1.1}$$

∂G= change in free energy (J mol^{-1}), μ_{Li}^{+} = chemical potential of lithium in the positive electrode (J mol^{-1}), μ_{Li}^{-} = chemical potential of lithium in the negative electrode (J mol^{-1})

By combining **Equation 1.0** and **Equation 1.1** the difference in chemical potential of lithium in two electrodes is equivalent to the free energy change associated with the transfer of lithium between the two electrodes.[13]

$$E = -\frac{(\mu_{Li}^{+} - \mu_{Li}^{-})}{nF} \qquad \textbf{Equation 1.2}$$

E = cell potential (V), μ_{Li}^{+} = chemical potential of lithium in the positive electrode (J mol^{-1}), μ_{Li}^{-} = chemical potential of lithium in the negative electrode (J mol^{-1}), n = number of electrons (1 as 1 electron is transferred per lithium), F = Faradays constant (96485 C mol^{-1})

The chemical potential of lithium within the graphite negative electrode is close to that of lithium metal ($\mu_{Li}^{Metal} = 0$). The chemical potential of a positive electrode, for example, $\mu_{Li}^{LiCoO_2}$ is significantly below that of graphite, resulting in a negative Gibbs free energy for the transfer of lithium from the negative electrode to the positive electrode at a high cell potential.[14]

To understand the voltage profile across a cell, and how it may vary with the state of charge or discharge due to lithium intercalation, the application of the Gibbs phase rule needs to be considered.

1.4.2 Gibbs Phase Rule

The Gibbs phase rule is written as;

$$F = C - P + 2 \qquad \textbf{Equation 1.3}$$

F = number of degrees of freedom (thermodynamic parameters), C = number of components present, P = number of phases present within the system

The thermodynamic parameters that need to be considered must be intensive variables, so that their values are independent of the amount of material present. From a lithium-ion perspective, the most useful variables are temperature, overall pressure and chemical potential.

As an example, within a lithium-ion battery, there will be two components; the lithiated and unlithiated states of the host metal complex. If the host material were $LiCoO_2$, which is a one phase material, the number of degrees of freedom will be three. Therefore when the pressure and temperature are controlled, the other remaining degree of freedom (in this case the chemical potential) will vary. However with $LiFePO_4$ which is a two phase material, the number of degrees of freedom is two. Thus, when the temperature and pressure is controlled, there are no degrees of freedom remaining, so the chemical potential of the system should remain constant during charge and discharge of the cell.[15]

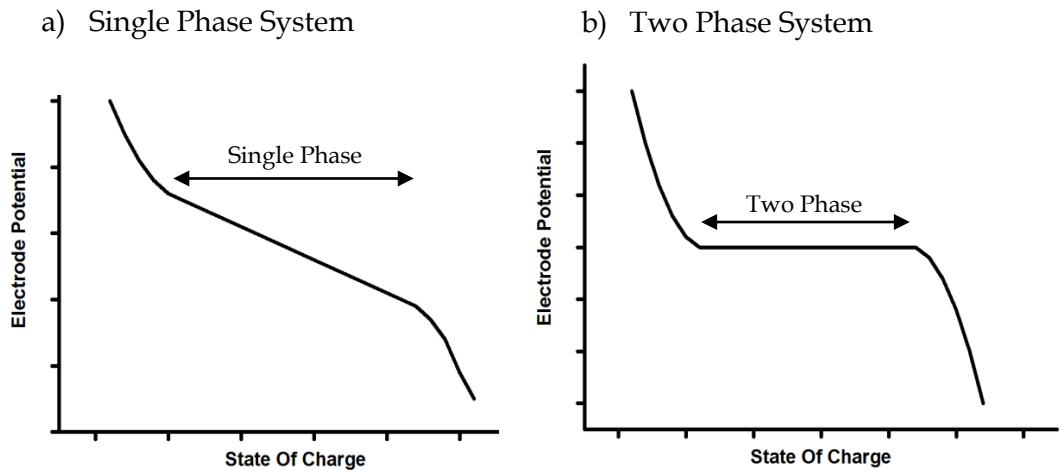

Figure 1.4 - Plots indicating the change in potential during discharge of a) single phase and b) two phase material.

1.4.3 Cell Capacity

The theoretical capacity is equivalent to the theoretical maximum amount of charge stored per unit mass or volume of the material. In the case of lithium-ion batteries, this would relate to the number of lithium ions that can be stored within the material structure and can be quantified in coulombs. However, specific capacity is more commonly reported as the technical non-SI unit of mA h g^{-1} in the field of battery science.

The theoretical specific capacity can be calculated from **Equation 1.4**

$$q = \frac{nF}{3.6\ X\ M} \qquad \textbf{Equation 1.4}$$

q = capacity in mA h g^{-1}, n = moles of electrons (mol), F = Faradays constant (96485 C mol^{-1}), M = molecular mass (g)

The moles of lithium ions passed is equivalent to the moles of electrons passed. The specific capacity is the capacity that can be practically obtained, which can be calculated from knowing the mass per gram of active material inside a composite electrode.

1.4.4 Rate Capability

By applying a range of different currents to a battery, the ability of a battery to charge or discharge over different timescales can be tested. As the rate of charge/discharge increases, the efficiency of the system will decrease.

Standardised rates of charge/discharge are used to allow for comparison between various materials, electrode designs and cells. The term C-rate is used to represent the standardised rate of charge or discharge. Charging a cell at a rate of 1 C is equivalent to passing a current which would result in the complete charge of a cell within one hour, assuming the theoretical capacity of the active material was achieved. C-rate is defined by **Equation 1.5**.

$$C = \frac{I}{M \; X \; Q_T} \qquad \textbf{Equation 1.5}$$

C = C-rate (hr^{-1}), I = applied current (mA), M = mass of active material (g),
Q_T = theoretical capacity of active material (mA h g^{-1})

Common battery rates that are applied to a cell are in the range of 0.1 C (ten hours) to 10 C (six minutes).

1.4.5 Electronic Conductivity

The electronic conductivity of a sample can be calculated from knowing the thickness, surface area and gradient from a cyclic voltammogram of the active material (bulk powder without electrolyte).

$$\sigma = \frac{L}{A} \; X \; \frac{I}{V} \qquad \textbf{Equation 1.6}$$

σ = conductivity (S cm^{-1}), L = thickness of electrode (cm), A = area of electrode (cm^2), I = current (A)
V = voltage (V)

The gradient of a CV will give the value of I/V, and hence the electronic conductivity of a bulk powder can be calculated.

1.5 The Lithium-Ion Battery

Rechargeable lithium-ion batteries have a charge/discharge process, in which a reversible reaction of the extraction/insertion of lithium ions takes place within a host matrix of electrode material.[16]

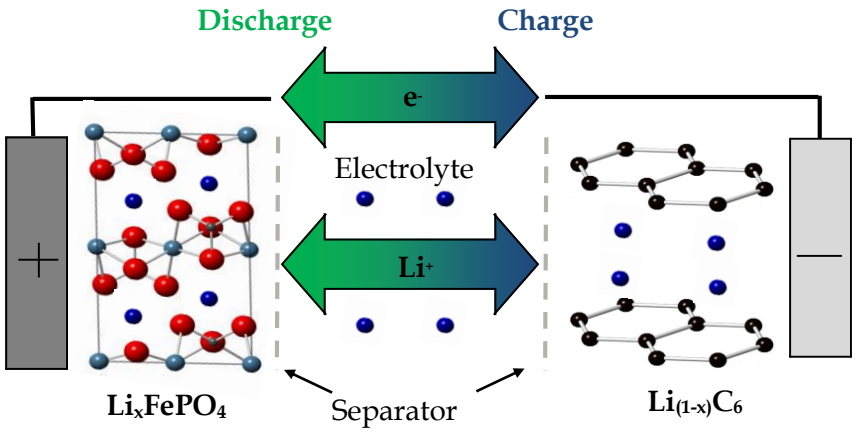

Figure 1.5 - Electrochemical operation of a lithium-ion battery.

Lithium-ion batteries provide a higher energy density compared to other rechargeable batteries such as the lead-acid battery, or nickel metal hydride batteries.[16] The higher the energy density of a battery, the more energy can be transported or stored within the same structural volume. Lithium-ion batteries have a high gravimetric and volumetric energy density, which would induce a high cell output that can be achieved by using non-aqueous electrolytes. The electrolyte is typically a solvent that contains dissolved salts to allow for good ionic conductivity. Non-aqueous electrolyte solutions are normally used because elemental lithium reacts vigorously with water and these electrolytes also have a wider temperature range of operation.

1.5.1 Charge and Discharge

During charge, a voltage is applied from an external source which is higher than that of the battery. This would drive the lithium ions out of the host cathode material (in the discharged state) and flow through the electrolyte to the anode, allowing the available electrons to do work around the external circuit. The loss of lithium from the host metal complex results in oxidation of the metal centre, and the lithium ions are embedded into the carbon. Upon discharge, the lithium ions spontaneously move in the reverse direction from the anode to the cathode when electronically connected.

$LiFePO_4$ / Graphite example;

During Charge

Positive electrode: $LiFePO_4 \rightarrow FePO_4 + Li^+ + e^-$

Negative electrode: $Li^+ + e^- + C_6 \rightarrow LiC_6$

During Discharge

Positive electrode: $FePO_4 + Li^+ + e^- \rightarrow LiFePO_4$

Negative electrode: $LiC_6 \rightarrow Li^+ + e^- + C_6$

Overall

$$LiFePO_4 + C_6 \leftrightarrow FePO_4 + LiC_6$$

(Discharged) (Charged)

The overall equation is balanced within this model. However in practice, not all of the lithium ions are transported back and forth within the system. Confusion can arise when referring to an electrode as a cathode or anode, as although during discharge an electrode may function as a cathode, when the current is reversed and the cell is charged, it becomes an anode. This is avoided by referring to the electrode that acts as a cathode during discharge of a cell as a positive electrode, while referring to the electrode that acts as an anode during discharge as a negative electrode.[17]

1.5.2 Properties of a Cathode Material (Positive Electrode)

There are many key requirements a cathode material must have to be a successful electrode that can achieve a high energy density and long cycle life. The energy and power density of a lithium-ion battery is largely determined by the cathode material, which stores the lithium ions by incorporating them into their crystal structure.[18] Below is a list of some of the criteria that a cathode material must meet to be a suitable electrode.[19]

- **Requires a high lithium chemical potential** referring to the ability of the cathode material to produce a change in a system (intercalation of lithium ions). This implies that the transition metal involved must have a readily available

oxidation state, which would allow for the lithium to be inserted / extracted into the host structure at the expense of the metal atoms redox states.

- **React with lithium in a reversible manner** to allow for the battery to be rechargeable. Minimising structural changes during lithium intercalation would improve the cycle life of the battery as the lithium ions would occupy unchanged host lattice sites (less loss of charge).
- **Allow for a large amount of lithium to be inserted/extracted rapidly** to maximise the cell capacity. This would depend on the number of lithium ion sites available and the range of diffusion pathways available within the host material.
- **Combination of good electronic and ionic conductivity** so that the material readily inserts/extracts lithium ions during the electrochemical reaction.
- **Low cost and environmentally benign**
- **Redox energy of the cathode must lie within the stability window of the electrolyte (work within an appropriate voltage range)**. This would prevent any unwanted side reactions involving the oxidation or reduction of the electrolyte which would have detrimental effects on the cell performance.

The energy and power density of a lithium-ion battery is largely determined by the cathode material, because the capacity values obtained compared to the anode are much smaller. This effectively makes the cathode the limiting factor in terms of performance. The Ohmic losses within a battery are related mostly to the cathode material as within conventional batteries, carbon on the anode has a high electronic conductivity.

1.5.3 Anode material (negative electrode)

The anode must have similar properties to the cathode; good stability, conductivity, and good efficiency in terms of lithium intercalation. In commercial cells the anode material is typically composed of graphite where one lithium ion can be intercalated into the graphite's molecular structure per six carbons (LiC_6).

Lithium metal can also be used as an anode, which would provide an excess source of lithium ions for the system. However this was ultimately rejected commercially due to the possibility of dendrite formation as described earlier.[20] If a battery is charged too

quickly, the lithium ions could deposit on these fibres rather than being inserted into the lithium metal.

Within this project, metallic lithium will be used as the anode in the lithium cells (known as half-cells). This is because the redox couple of metallic lithium to lithium ions has a stable voltage which means that the electrode can also be used as the reference electrode. The cells that are constructed are on a relatively small scale which would minimise any potential hazards.

1.5.4 Electrolyte and the Solid Electrolyte Interface (SEI) Layer

The electrolyte plays a crucial role within lithium-ion batteries, allowing for both the transfer of lithium ions between the electrodes and the formation of stable passivation layers at the surface of the electrodes. The electrolyte acts as a lithium ion carrier by solvating the lithium ions for transport through the liquid medium to the respected electrode.

A common electrolyte salt is lithium hexafluorophosphate ($LiPF_6$), which is a metal salt that can conduct lithium ions in the presence of a solvent. $LiPF_6$ is used within batteries due to a combination of well-balanced properties in terms of relatively high dissociation and good mobility, resulting in high ionic conductivity in comparison to the other electrolyte salts.[21]

Average Ionic Mobility

$LiBF_4$ > $LiClO_4$ > **$LiPF_6$** > $LiAsF_6$ > LiTf > LiIm

Dissociation Constant

LiIm > $LiAsF_6$ > **$LiPF_6$** > $LiClO_4$ > $LiBF_6$ > LiTf

$LiPF_6$ based electrolytes form a passivation layer on aluminium current collectors which are commonly used in positive electrodes. One drawback to using $LiPF_6$ is that the P-F bond is rather labile toward hydrolysis, even by a trace amount of water. $LiPF_6$ can readily decompose in water to form hydrofluoric acid (HF) which would degrade the battery over time.

The solvents used in the majority of commercial lithium-ion battery electrolytes consist of organic carbonates. **Figure 1.6** shows the structure of common organic carbonates used. Cyclic carbonates have high dielectric constants which allow for relatively high concentrations of lithium salt to be dissolved, however they are also relatively viscous, giving them a high resistance (or low mobility). Linear carbonates are combined with the cyclic carbonates to reduce the viscosity, but there is a trade-off due to their low dielectric constants. In most cases, a combination of carbonates (cosolvents) are used with the lithium salt to suit the physical and chemical properties of the electrolyte.

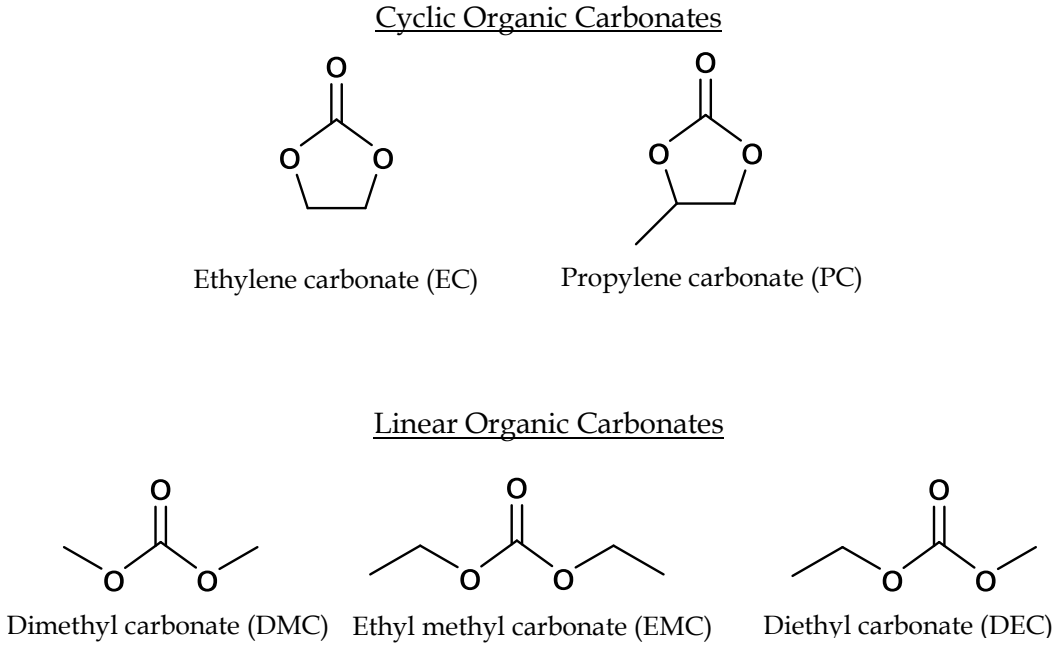

Figure 1.6 – Chemical structure of solvents commonly used within electrolytes in lithium-ion batteries.

The electrolyte decomposes through the breakdown of the organic solvents on the surface of both electrodes during cell operation; this forms a solid layer which coats the surface of the particles known as the solid electrolyte interphase (SEI) on the negative electrode. The SEI layer protects the electrodes against continuous solvent decomposition. Over time however, this low conducting layer grows on the surface of the particles as a battery is continuously cycled and eventually leads to capacity fade as sufficient ionic conductivity diminishes.[22]

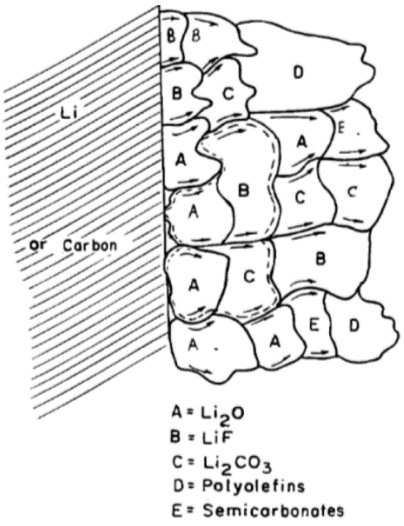

Figure 1.7 – Mosaic type model of the SEI layer formed at the surface of the negative electrode in a lithium-ion battery soaked in an electrolyte consisting of $LiPF_6$ in carbonate based solvents. Lithium transport was suggested along the grain boundaries. Reproduced from reference[23] by permission of The Electrochemical Society.

Figure 1.7 illustrates the complexity of the SEI layer on a graphite electrode. The composition and structure of an SEI layer has been found to be dynamic, varying in composition and structure. A large range of different products have been reported to be present within an SEI layer, including both organic and inorganic substances.[21] It has been generally accepted that the predominant electrolyte reduction products of graphite based electrodes in standard electrolyte solutions are made up of lithium alkyl carbonates and inorganic components LiF and $Li_xPF_yO_z$.[24] Recent applications of *in-situ* techniques on model surfaces of positive electrodes have revealed new insights into the SEI layer on the positive electrode which have been found to contain P-O containing species, lithium oxides, fluorides and carbonates.[25,26]

Oxygen release from oxygen containing cathodes upon charging to high voltages can trigger the nuceophilic attack of carbonate electrolytes by superoxide (O^{2-}), which can form upon discharge to 3 V *vs.* Li/Li^+ and lower, which leads to SEI film formation.[27] Pioneering work by Aurbach *et al.*[28] and recent work on Li-oxygen batteries[29,30,31] have shown that superoxide can attack carbonate solvents, forming inorganic species such as Li_2CO_3, or RCO_2Li and $R(OCO_2Li)_2$.

The current understanding on SEI layers is derived largely from studies of composite electrodes that contain addictive carbon and binder, which can influence the formation of SEI layers and lead to ambiguities in the compositions reported. In positive

electrodes, the fraction of carbon used is low, but the surface area of conducting carbon is extremely high and its reactivity toward the electrolyte could dominate the SEI on the surface of the electrode.[32]

Progress in understanding SEI layers has been achieved using techniques such as X-ray photoelectron spectroscopy (XPS), Fourier transform infrared spectroscopy (FTIR), X-ray diffraction, atomic force microscopy (AFM) and scanning tunnelling microscopy (STM). Although significant work has been studied on SEI layers, there is much that needs to be understood on a fundamental level. There is still limited understanding of the full characterisation of these layers, by which mechanisms they are formed and how they influence a batteries performance.

1.5.5 Battery Design

Battery design is an important aspect to consider to assure optimum and safe operation of a commercial battery. Factors such as cell uniformity, the number of cells, battery case design, effects of temperature and charge/discharge conditions can significantly alter the performance of a range of batteries. The difficulty of scaling up newly developed battery technology must also be considered when attempting to manufacture larger cells on a production line. Rechargeable batteries should be built using cells that have matched capacities. If the cells are not balanced, the battery will not perform to its designed capacity.

If a cell were to fail, it would commonly result in an increase in the internal pressure, resulting in a rupture or an explosion of the battery. Battery failure can result from short-circuiting, excessive high charge/discharge rates and improper charge control. Control of the charge process is critical to maintain good life and safety of the battery. The current and voltage must be controlled to prevent over charging and the temperature of the battery must stay within the working temperature range for that particular battery.

1.5.6 Commercial Lithium-ion Batteries

1.5.6.1 Cell Types

Commercial lithium-ion batteries are usually produced in one of three designs; cylindrical, prismatic or a polymer/pouch type.[33] The design of the battery depends on the requirements of the application. All commercial cells have common features of non-aqueous electrolytes, a microporous polyolefin separator and composite electrodes attached to metal foil current collectors.

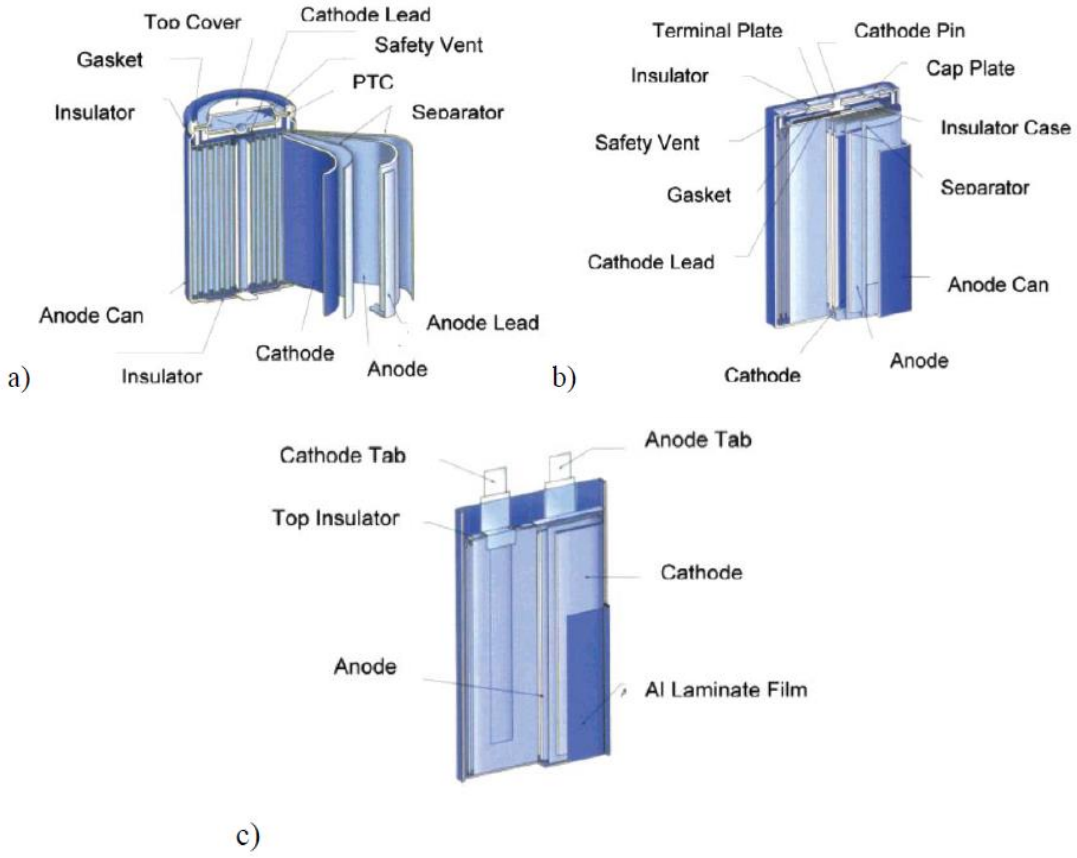

Figure 1.8 - Commercial lithium-ion battery designs a) cylindrical b) prismatic c) polymer/pouch. Reprinted with permission from reference[33] Copyright 2004 American Chemical Society.

1.6 High Voltage Lithium-Ion Batteries

High voltage lithium-ion batteries have been a recent new focus in the current energy storage market due to the potential application of high energy density batteries for electric vehicles. In order to further increase the energy density, a high cell voltage and/or a higher capacity material must be used.[34]

$$E = \int_0^{\Delta t} IV(t)\, dt = \int_0^{V(q)} V(q)\, dq \qquad \textbf{Equation 1.7}$$

E = specific energy (W h kg^{-1}), V = cell voltage (V), I = current (A), t = Time (h), Q = capacity (A h kg^{-1})

For a given amount of charge, a higher voltage equates to more energy stored. The insertion and removal of lithium from conventional lithium-ion batteries, particularly those that operate at a relatively high voltage, face structural and chemical challenges when continually exposed to high electrochemical potentials *vs.* lithium (Li/Li^+). A major barrier to high voltage lithium-ion battery systems is the voltage stability of the electrolytes.[35] Conventional carbonate based electrolytes decompose readily through oxidation on the surface of the electrode particles when the cell is charged over 4.5 V. The electrolyte decomposition will occur at a much faster rate with high voltage systems.

The development of stable electrolytes which can operate at a high voltage (5 V *vs.* Li/Li^+) is a key area surrounding high voltage battery systems. Non-aqueous organic electrolytes are commonly used, but to produce more stable electrolytes there must be a compromise on the viscosity and conductivity. The use of quaternary nitrogen based ionic liquids or the addition of electrolyte additives have been used to stabilise the charged cathode surface to allow for lithium intercalation at the desired 5 V region. Ionic liquids suffer from their intrinsically high viscosity, low dielectric constant and low ionic conductivity.[35]

1.6.1 Decomposition Limit of Cathode Materials

Within a lithium transition metal oxide based cathode, the intercalating mechanism can be represented as;

$$Li_xM_yO_z \rightarrow Li_{(1-x)}M_yO_z + xLi^+ + xe^- \qquad \textbf{Equation 1.8}$$

Although lithium can be removed from the material, there is also a possibility that the oxide is involved in a parallel reaction of decomposition at high potentials. For example, with lithium cobalt oxide ($Li_{1-x}CoO_2$), it has been reported that in the course of delithiation where $x > 0.5$, electrons can be transferred from the oxygen band.[36,37] This could result in the oxidation of O^{2-} ions to gaseous O_2 which would evolve from the lattice and can be hazardous within an operational cell.

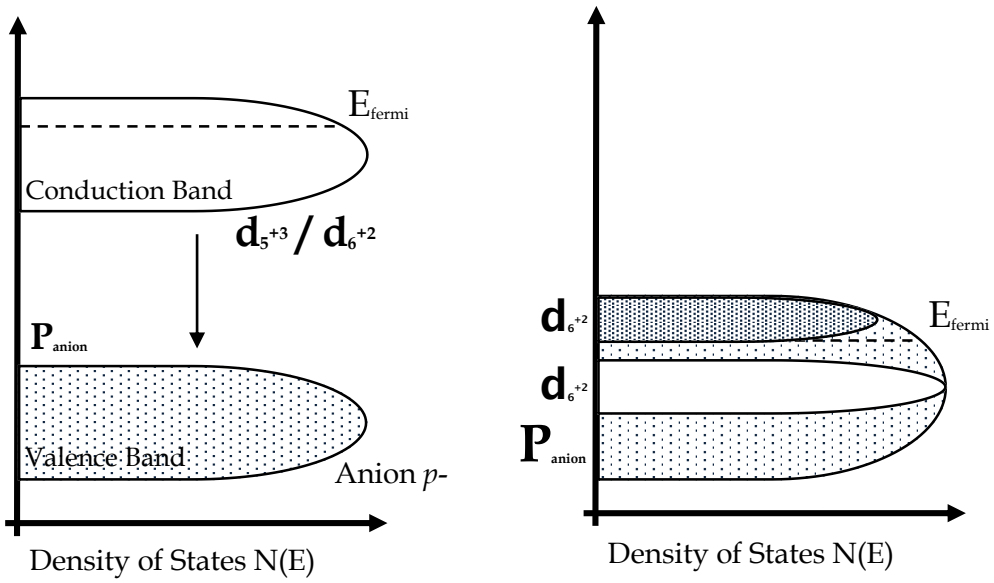

Figure 1.9 - Schematic diagram of the band levels for potential oxygen evolution within a lithium metal oxide system.

A variety of lithium insertion cathode materials can be considered as semi-conductors. Semi-conductors have a conductive band due to the metal *d*-orbitals and a valence band formed by oxygen *p*-orbitals. As oxidation of the transition metal proceeds (during charge), the redox level along the Fermi level moves down toward the valence band and the p_{anion} share in the hybridization. As higher potentials are reached, the transition metal redox couple band will eventually reach the top of the valence band; starting from this point, if further lithium extraction follows, the electrons tend to be taken from the valence band. This will allow di-anionic states like $(O_2)^{2-}$ to potentially disproportionate into oxygen gas.[36]

1.6.2 Improving Electronic Conductivity

The class of $LiMPO_4$ (M=Fe,Mn,Co) cathode materials have a low electronic conductivity which has been effectively combated by carbon coating the particle surface. Carbon is an excellent electronic conductor with a high surface area, which can improve the conductivity as well as protect the active material from direct contact with the electrolyte.[38]

The use of carbon coatings may contribute to higher capacities obtained and improved rate capability. The layer of carbon surrounding the particle ideally would have a fine uniform layer, which would enhance the intra-particle conductivity. However if the carbon layer on the particles is too thick, the lithium ions could potentially struggle to penetrate through the carbon layer and access the core of the particles.

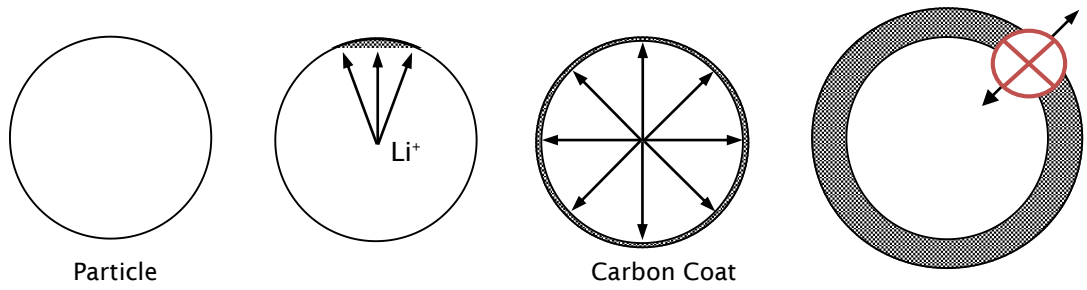

Figure 1.10 - Effects of carbon coating the active material particles.

There are a variety of different ways to carbon coat a surface; a few examples include ball milling the material with carbon, as well as the thermal decomposition of a precursor. Sucrose is typically used, expelling water in the process.[39]

$$C_6H_{12}O_6 \xrightarrow{\Delta} 6C + 6H_2O$$ **Equation 1.9**

1.7 Advances made in Lithium Containing Cathode Materials

1.7.1 Lithium Transition Metal Oxides

There are currently three major types of metal oxide structures that are used as cathode materials within lithium ion batteries.[40] These structures should maintain good ionic conductivity and be subject to minimal distortions during battery cycling so that the lithium sites remained unchanged.

- **Layered oxides (a)**
- **Oxides with a spinel structure (b)**
- **Poly-anion oxides with an olivine or olivine-related structure (c)**

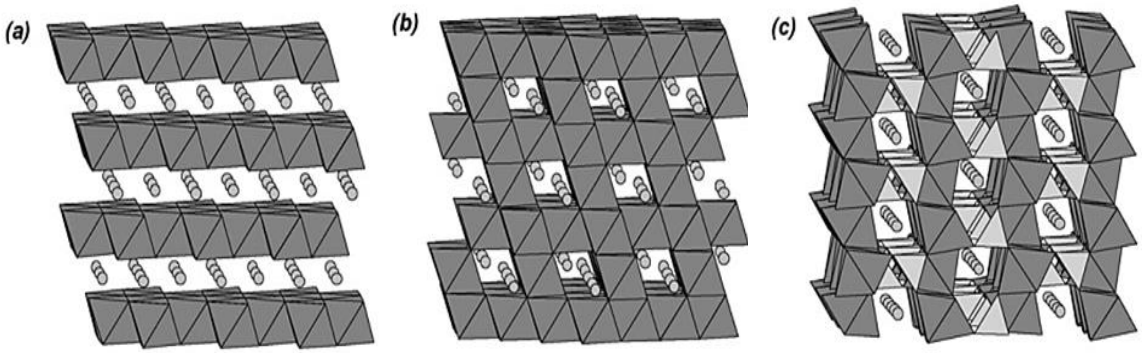

Figure 1.11 – Schematic of different lithium containing transition metal oxide structures. Reproduced from reference[41] with permission.

1.7.2 Key Examples of Cathode Materials

1.7.2.1 $LiCoO_2$

$LiCoO_2$ was first developed as a cathode material in 1980 by John B. Goodenough.[42] The structure has been described previously within this report, and the commercially used $LiCoO_2$ has reasonable power capabilities and a high energy density, making it a suitable cathode to use within lithium ion cells. A theoretical capacity of 274 mA h g^{-1} corresponds to a full lithium extraction which is possible,[43] however the reversible capacity is limited to 140 mA h g^{-1} to ensure long time cycling between 3 and 4.2 V.

Delithiation proceeds topotactically[44,45] and is reversible over the composition range $1 > x > \sim 0.5$ for x in Li_xCoO_2. The material can demonstrate hundreds of cycles within this range. Extraction of lithium to values above 0.5 results in higher capacities initially,

but often increases cycling losses.[46] The cycling losses have been associated with side reactions involving particle surfaces which increases the cell resistance and structural instabilities associated with phase changes at high amounts of lithium extraction.[47,43,48]

1.7.2.2 Spinel-Type Oxide Materials - $LiMn_2O_4$

The general formula of spinel oxides is LiM_2O_4 (M = Mn) and they are composed of octahedral-coordinated M-cations and Li-cations in tetrahedral positions of a cubic close packed O^{2-} lattice. The framework remains stable while lithium reversibly moves between the tetrahedral sites, making spinel-type oxides promising materials for lithium-ion cathodes.

The spinel structure (space-group *Fd3m*) $LiMn_2O_4$ was developed in 1984.[49] This structure has LiO_4 tetrahedra with edge-shared MnO_6 octahedra, with direct Mn-Mn interactions that offer good structural stability.[50] The $Mn^{3+/4+}$ 3d band is above the 2p O^{2-} band which would offer good chemical stability in comparison to $LiCoO_2$. The close packed oxygen array may allocate cations in tetrahedral and octahedral sites to build up the spinel structure and the lithium ions can be inserted/extracted in other sites that are unoccupied by cations.[51] This material promises good safety and manganese is also cost effective.[52]

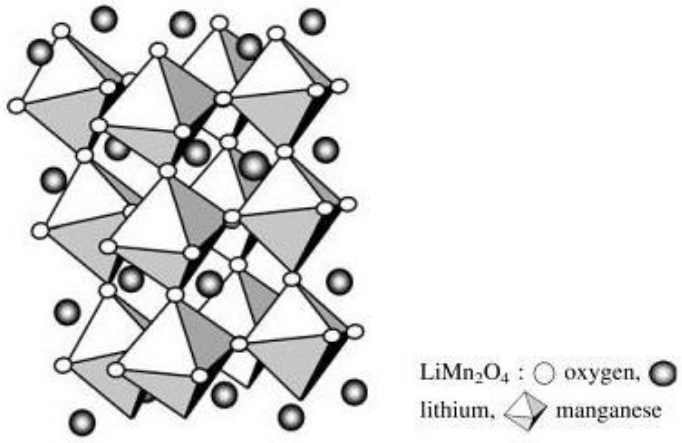

Figure 1.12 Spinel structure of $LiMn_2O_4$. Reproduced from reference[53] with permission.

Early work showed that it is possible to remove lithium using a mild acid treatment.[54] During this process, manganese is oxidised from an average oxidation state of +3.5 to

+4, and the λMnO_2 phase retains its spinel framework. In addition, some dissolution of manganese can occur:

$$2LiMn_2O_4 + 4H^+{}_{(aq)} \rightarrow 2Li^+{}_{(aq)} + Mn^{2+}{}_{(aq)} + 2H_2O + 3\,\lambda MnO_2$$

Oxidative extraction of lithium from the tetrahedral 8a sites was demonstrated to occur at slightly above 4 V and was reversible.[55] When carried out in a cell with lithium as the anode, the process occurs below 3 V *vs.* Li/Li^+, and the discharge profile indicated a two phase reaction present (flat voltage profile). The tetragonally distorted phase $Li_2Mn_2O_4$ is formed due to the cooperative Jahn-Teller Mn^{3+} ions.[56]

The octahedral to tetragonal transition results in a change in the unit cell volume; studies report the c/a ratio could increase by 16% and unit cell volume itself increases by 6.5%.[16] These changes are severe and result in particle disintegration and loss of particle contact within the composite electrode. The capacity loss is so rapid, that even after only a few cycles into the 3 V *vs.* Li/Li^+ region the cell performance was greatly compromised. However, extraction of lithium above 4 V *vs.* Li/Li^+ maintains the cubic structure and results in smaller volume changes, which is why the discharge is typically limited to 4 V *vs.* Li/Li^+.

Figure 1.13 is a crystal field diagram with the appropriate energy levels for the $3d^n$ ion. The geometric distortions occur due to the addition of an available electron from Mn^{4+} to Mn^{3+} (on discharge) which would give an unsymmetrical set of electrons in the *e* orbital. This change prompts the system to distort from the cubic arrangement to the tetragonal arrangement to reduce the energy of the overall system. The average oxidation state of Mn in $LiMn_2O_4$ is +3.5 which is on a critical point, so that even at room temperature, any external insertion of Li^+ ions can induce Jahn-Teller distortion.[57] After distortion, the tetragonal geometry would consist of longer Mn-O bonds about the *c* axis and short Mn-O bonds along the *a* and *b* axes.

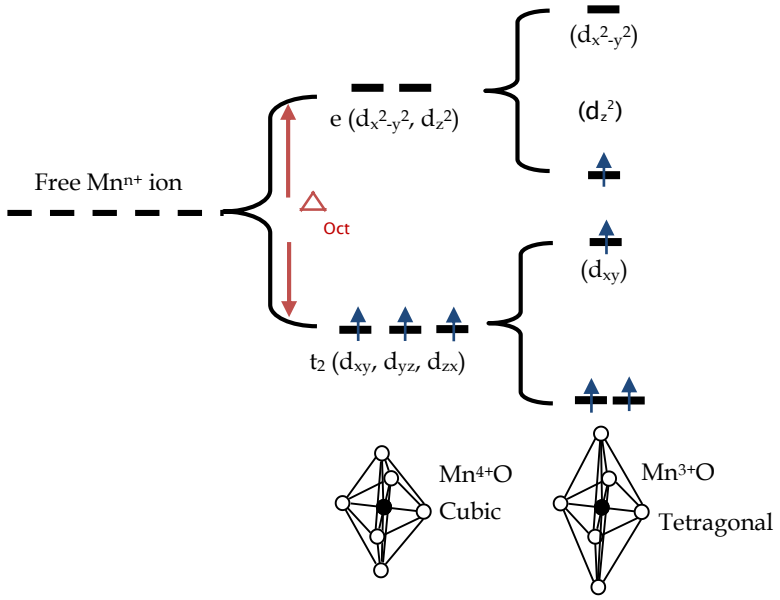

Figure 1.13 - Octahedral system undergoing tetragonal distortions via elongation of the c-axis and shortening of the *a* and *b* axes.

From the early 1990s onwards, efforts were devoted to the development of the $LiMn_2O_4$ for lithium-ion batteries. Although limiting discharges to 4 V does result in much better cycling, gradual capacity fading is still observed.[58] This behaviour has been associated with several different reasons such as electrolyte breakdown at high potentials, dissolution of the manganese, and loss of oxygen from the spinel structure.[59,60,61]

1.7.2.3 $LiFePO_4$

Iron is a metal in the first transition series which can exhibit a wide range of oxidation states. It is an appealing metal to use within lithium containing cathode materials as it is inexpensive, environmentally benign and abundant.[62] Interest in $LiFePO_4$ was initiated in 1997, and the material has been intensely studied to date.[63]

$LiFePO_4$ is in a class of materials known as phosphor-olivines, which adopt the orthorhombic structure with space group *Pnma*.[63] This structure can be considered as the hexagonal structural analogue of the spinel structure.[63] The Li^+ and Fe^{2+} occupy octahedral sites, and the phosphorus is located on tetrahedral sites in a distorted hexagonal close packed oxygen array (hcp). The FeO_6 octahedra share corners and LiO_6 octahedra share edges along tunnels down the *b*-axis, through which lithium ions can move through a one dimensional pathway.[64] The reversible lithium intercalation proceeds at around 3.45 V during charge with a theoretical capacity of 170 mA h g^{-1}.

The iron based oxides containing O^{2-} as the anion propose a problem in which the $Fe^{4+/3+}$ redox energy level tend to lie too far below the Fermi energy level of a lithium anode and the $Fe^{3+/2+}$ too close to it.[63] The use of phosphate polyanions has been shown to lower the Fe^{3+}/Fe^{2+} redox energy to useful levels. $LiFePO_4$ has drawn the most attention as several reports have demonstrated a high-rate capability with high columbic efficiency and satisfactory cycle life.[65,66,67] Furthermore it has a good thermal stability and little hygroscopicity which makes the battery relatively safe for use.[62]

$LiCoO_2$ and $LiMn_2O_4$ form solid solutions over a large concentration range. They have occasional weak first-order transitions due to electronic effects or lithium ion ordering. $LiFePO_4$ is an exception which stores lithium ions through a two phase transformation. One major drawback of $LiFePO_4$ is that it is a poor ionic and electronic conductor which can cause capacity losses at high charge/discharge currents.[68] This leads to slow diffusion of lithium ions through the $LiFePO_4/FePO_4$ interfaces. When the poor ionic conductivity of $LiFePO_4$ is overcome, the performance of this material reaches a high standard.

The single-phase transformation pathway occurs at very low overpotential, allowing the system to bypass nucleation and growth of a second phase. The $LiFePO_4$ system is

an example where the kinetic transformation path between $LiFePO_4$ and $FePO_4$ is fundamentally different from the path deduced from its equilibrium phase diagram.[18]

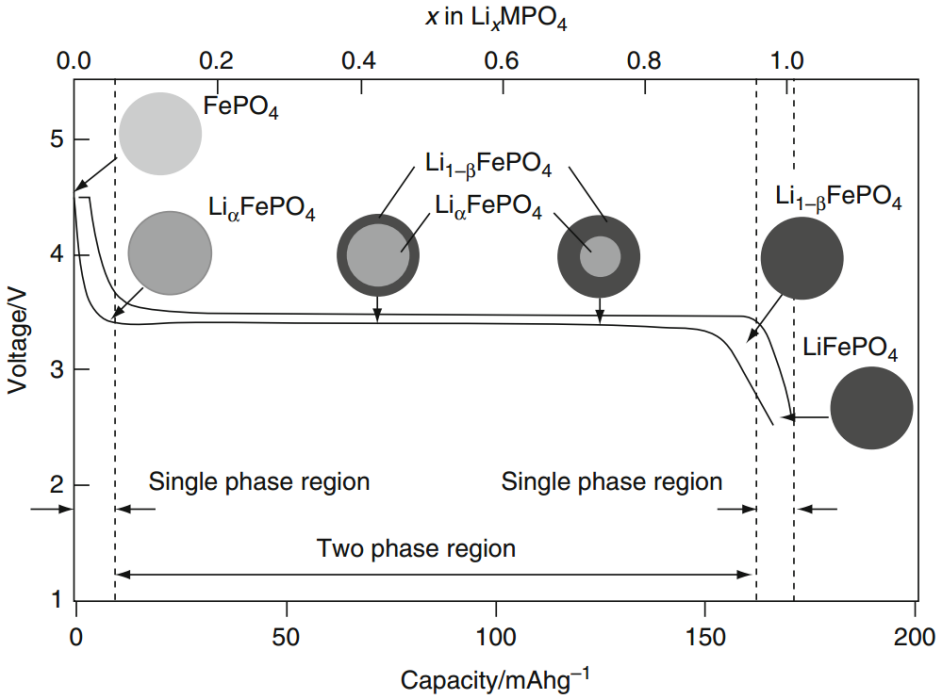

Figure 1.14 - Typical discharge profiles with phase regions highlighted within the $LiFePO_4$ particles. Reproduced from reference[69] with permission.

Figure 1.15 displays the two different structural phases present within $LiFePO_4$. The lithium ions can be extracted upon charge to leave a new phase, iron phosphate $FePO_4$. Hence, a two phase process with reference to lithium ion insertion/extraction exists.

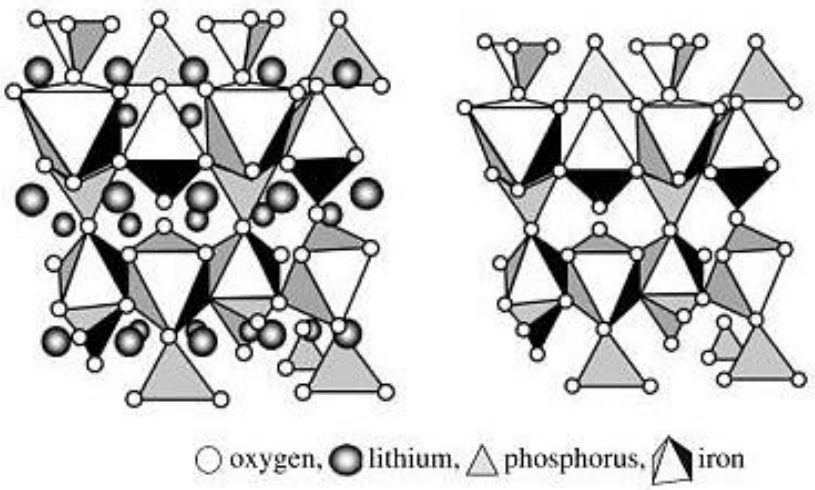

Figure 1.15 - The structure of the two phases present within $LiFePO_4$ due to lithium ion insertion (left)/ extraction (right). Reproduced from reference[53] with permission.

When the battery is fully charged, the cathode material is mainly $FePO_4$ and the lithium ions migrate from the anode to the cathode to the appropriate sites within the structure to obtain the new phase $LiFePO_4$. The insertion/extraction of the lithium ions within the framework of the ordered olivine structure has been reported to maintain its structure reasonably well with minor displacements, highlighting its structural stability.[63]

$LiFePO_4$ is an intrinsically safer cathode than $LiCoO_2$ due to the strength of the P-O bond. This bond is highly charge separated with d_π-p_π bonding which makes the oxygen much harder to be evolved as gas within a failing cell.

1.7.3 $LiNi_{0.5}Mn_{1.5}O_4$ – A High Voltage Cathode Material

The cathode materials that have been discussed to this point do not operate at very high voltages. $LiNi_{0.5}Mn_{1.5}O_4$ is a high voltage cathode material, and has a high operating potential of 4.7 V *vs.* Li/Li^+ and a reasonable capacity of 147 mA h g^{-1}.[70]

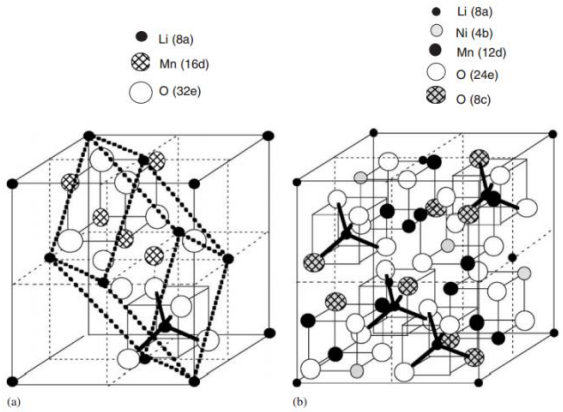

Figure 1.16 – Schematic representation of the two different structures available for $LiNi_{0.5}Mn_{1.5}O_4$. a) *Fd3m* b) $P4_132$. Reproduced from reference[71] with permission.

There are two kinds of crystal structure for $LiNi_{0.5}Mn_{1.5}O_4$; the face-centred spinel (space group *Fd3m*) and the primitive simple cubic structure (space group $P4_132$). For $LiNi_{0.5}Mn_{1.5}O_4$ with a face-centered structure, the lithium ions are located in the 8a sites of the structure, the manganese and nickel ions are randomly distributed in the 16d sites. The oxygen ions which are cubic close packed occupy the 32e positions. For $LiNi_{0.5}Mn_{1.5}O_4$ with a primitive simple cubic structure, the manganese ions are distributed in 12d sites, and nickel ions in 4a sites. The oxygen ions occupy the 24e and 8c positions, while the lithium ions are located in the 8c sites.[72] In this case, the Ni and Mn ions are ordered regularly.[73] Whether $LiNi_{0.5}Mn_{1.5}O_4$ has a structure of face-centered spinel or primitive simple cubic depends on its synthetic routes. In synthesising $LiNi_{0.5}Mn_{1.5}O_4$, annealing process at 700 °C after calcination lead to the ordering of Ni and Mn ions, making it transformed from face-centred spinel to the primitive cubic crystal structure.[72] The disordered *Fd3m* spinel was found to have superior electrochemical behaviour and structural reversibility compared to the $P4_332$ structure.[74]

For spinel $LiNi_{0.5}Mn_{1.5}O_4$, electrochemical activity occurs between 4.6 - 4.8 V *vs.* Li/Li^+, which is due to the redox $Ni^{2+/4+}$ in a two electron process. While in the 4 V region, the electrode sometimes shows some minor redox behaviour, related to the $Mn^{3+/4+}$ couple.

Gao *et al*. put forward an explanation for the origin of high voltage operational behaviour. As an electron is removed from Mn^{3+}, it is removed from Mn eg (↑) which has an electron binding energy at around 1.5–1.6 eV, and this accounts for the 4.1 V plateau. When there are no more electrons left on Mn eg (↑) (all Mn are Mn^{4+}), electrons are removed from Ni eg (↑↓) which has an electron binding energy of about 2.1 eV, and the voltage plateau moves up to 4.7 V because of the increased energy needed to remove electrons.[75]

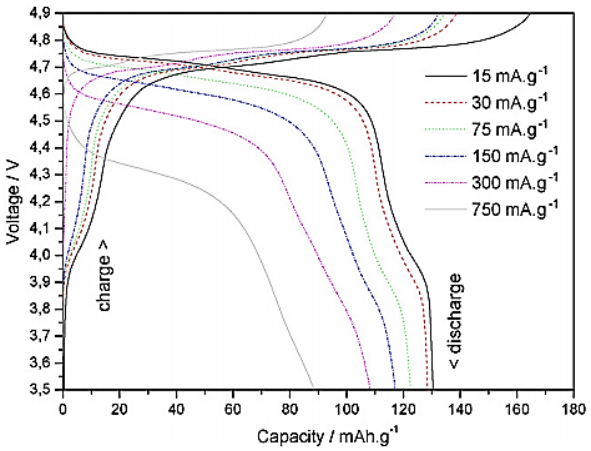

Figure 1.17 – Discharge profiles of $LiNi_{0.5}Mn_{1.5}O_4$ at various C-rates, where 750 mA h g^{-1} was given at 5 C in $LiPF_6$ EC:DMC (2:1). Reproduced from reference[76] with permission.

The rate capability and cycling performance of $LiNi_{0.5}Mn_{1.5}O_4$ has been significantly improved by doping a small amount of ruthenium into the structure, specifically $Li_{1.1}Ni_{0.35}Ru_{0.05}Mn_{1.5}O_4$.[77] The crystal volume is enlarged by doping ruthenium into the structure which is beneficial for lithium ion diffusion inside the lattice. The high performance of these doped materials is mainly due to minimised polarisation and improved electrical conductivity. **Figure 1.18** displays the cycling results of $Li_{1.1}Ni_{0.35}Ru_{0.05}Mn_{1.5}O_4$ at a very high C-rate of 10 C (six minute charge) and was maintained over a remarkable number of cycles.

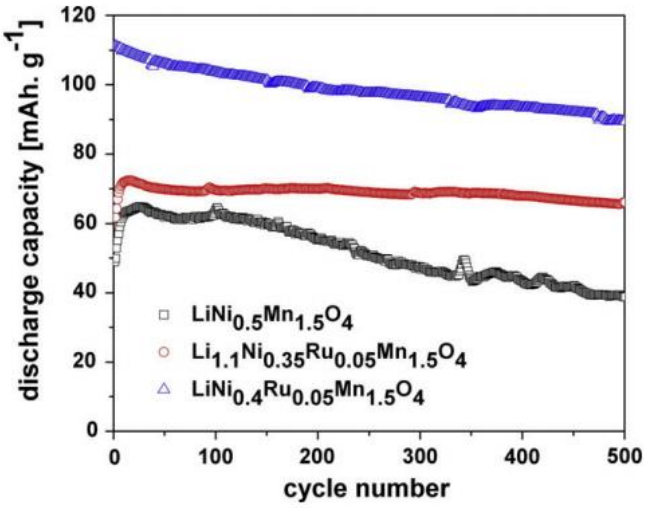

Figure 1.18 – Capacity retention of different levels of ruthenium doped $LiNi_{0.5}Mn_{1.5}O_4$ at 10 C. Reproduced from reference[77] with permission.

1.7.4 $LiCoPO_4$ Timeline of Key Events

$LiCoPO_4$ is a member of the phosphor-olivines, with a similar structure to $LiFePO_4$ but with cobalt substituted for iron. $LiCoPO_4$ is a high voltage cathode material that exhibits electrochemical activity at around 4.8 V *vs.* Li/Li^+.[78,79] The first recognised paper on the performance of $LiCoPO_4$ as an insertion material for lithium-ion batteries was in 1999 by Amine.[80] A pure olivine phase was obtained with the space group *Pmna* via the calcination of the stoichiometric mixtures of the appropriate metal salts (no carbon coating). A charge and discharge capacity of 105 and 80 mA h g^{-1} was achieved with a potential limit of 5.3 V *vs.* Li/Li^+, in which a plateau was seen at around 4.8 V. Capacity fade was associated with the decomposition of the electrolyte which was $LiPF_6$ dissolved in sulfolane.

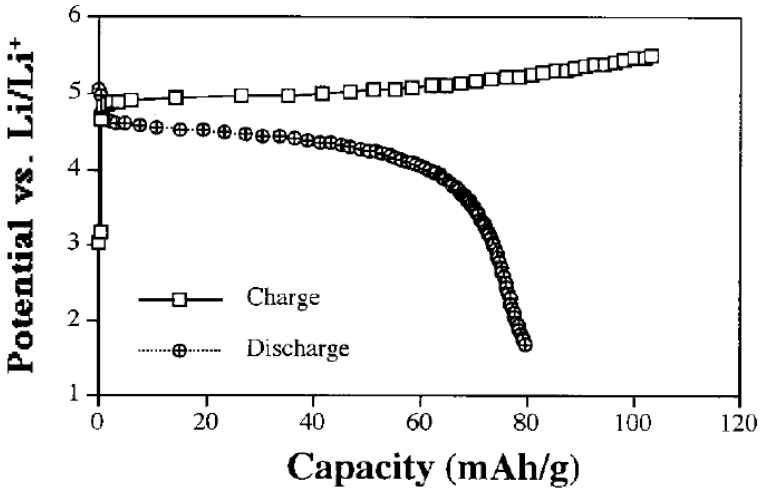

Figure 1.19 – Charge and discharge curves of $LiCoPO_4$ from 1999. **Reproduced from reference[81] with permission.**

As interest grew around the phosphor-olivine $LiMPO_4$ (M = Fe, Mn, Co), more work was carried out on the $LiCoPO_4$ cathode. A discharge capacity of 100 mA h g^{-1} was achieved in 2001 when using $LiPF_6$ EC:DMC where a single phase was observed.[82] The initial discharge capacity improved over time, with different novel synthesis procedures. A high capacity (even by today's standards) of 125 mA h g^{-1} was achieved in 2002 by Okada *et al.* through using carbon black as a temporal dispersing agent, which was later eliminated as CO_2. The carbon black addition yielded a small particle size with a finely dispersed solid, which was responsible for the improved electrochemical behaviour.[83]

Different synthesis pathways began to focus on improving the intrinsic conductivity of the material, as well as investigating various different electrolyte salts.[84] Bramnik reported that high temperature and low temperature synthesis conditions altered affected the performance of the material in terms of its capacity, which was again associated to particle size differences. Up to this point, no images of the $LiCoPO_4$ particles were shown in the work of Okada and Amine, so no comparisons could be made. Bramnik's paper in 2004 gave evidence of a two-step mechanism during charge in which two plateau regions were seen in the voltage ranges of 4.80 – 4.8 V and 4.88 - 4.93 V *vs.* Li/Li^+.[85] Upon discharge, two different phases could be seen but they were badly resolved and only became more evident in the subsequent cycles.

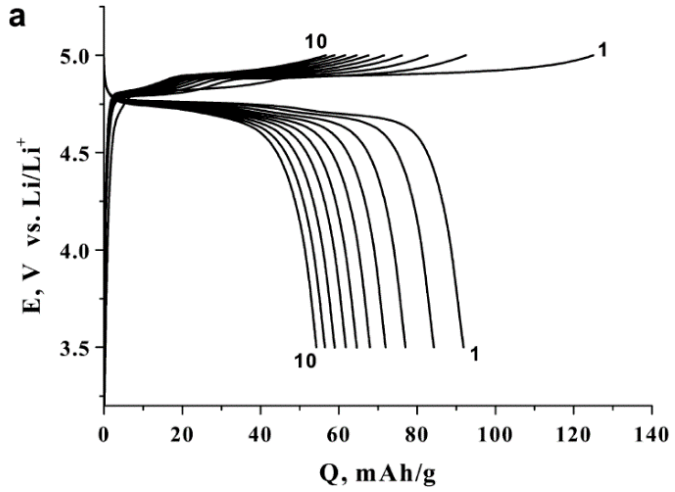

Figure 1.20 – Charge and discharge profiles of $LiCoPO_4$, highlighting the two different plateaus and cycle life degradation. Reproduced from reference[85] with permission.

Nickel was one of the first metals to be doped into the $LiCoPO_4$ system.[79,86] This was unsuccessful as the use of nickel did not allow for reversible lithium intercalation and increased the working potential to over 5 V which proved to be even more challenging. Wang *et al.* began efforts to control the size and morphology of the $LiCoPO_4$, noticing that the pH value of the starting solution had significant effects on the final product produced.[87] It was suggested that high alkalinity was in favour of the formation of $LiCoPO_4$. The particles were formed via a dissolution-recrystallisation process in which alkaline conditions promoted supersaturation of $LiCoPO_4$ and was grown through solute diffusion. Under acid conditions, the solution was not saturated for $LiCoPO_4$ all of the time leading to products deficient in lithium.

Different atmospheric heating conditions of high purity argon, air, and pure oxygen were investigated in 2005 by Wolfenstine *et. al*, which showed enhanced discharge capacities for $LiCoPO_4$.[88] It was suggested that heating under argon gave a smaller particle size of $LiCoPO_4$, due to the presence of cobalt phosphides and an increased carbon content.[89] This would increase the overall electrical conductivity of the composite electrode. The production of metal phosphides (heating under argon instead of air) has been shown to increase the electrical conductivity for $LiNiPO_4$ composite electrodes, showing similar results.[64] The $LiCoPO_4$ discharge capacity under argon was ~1.4x that for the air sample (101 mA h g^{-1} compared to 72 mA h g^{-1}). It was later discovered that having over 5% of Co_2P (cobalt phosphide) actually reduces the discharge capacity through preventing Li^+ ions from entering/leaving $LiCoPO_4$ and also having extra 'dead mass' in the composite electrode.[90]

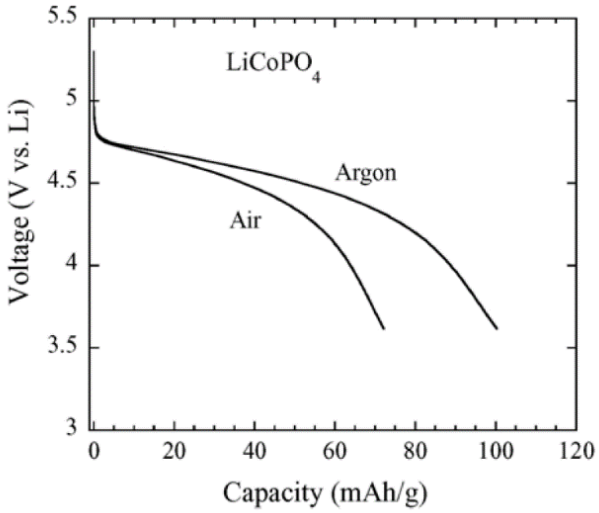

Figure 1.21 – First cycle discharge curves for $LiCoPO_4$ heated under air and high purity argon. Reproduced from reference[88] with permission.

The first *in-situ* XRD study on $LiCoPO_4$ was performed in 2005 by Bramnik *et. al*. The $LiCoPO_4$ and $CoPO_4$ phases were refined, with both phases decreasing slightly in size during charging.[91] Further *in-situ* studies in 2007 showed the presence of two two-phase regions, with the existence of an intermediate phase contradicting mechanisms previously reported for this compound and differs from the mechanisms known for $LiFePO_4$ and $LiMnPO_4$. It was proposed that the intermediate phase had a composition of $Li_{0.7}CoPO_4$, and that the $CoPO_4$ phase could only be detected under inert conditions as it becomes amorphous when exposed to air.[92]

Nano-sized $LiCoPO_4$ was synthesised through a rapid method involving microwave heating.[93] The average size of the particles were ~150 nm, and no Co_2P impurities were

detected. A discharge capacity of 144 mA h g^{-1} was achieved at 0.1 C, with a voltage window of 5.0 – 3.0 V *vs.* Li/Li^+. Only a one-step mechanism was observed (single flat plateau), and the cycle life was poor. It has been previously reported that several electrode materials, such as $LiFePO_4$ have a thermodynamic driving force toward phase separation; however this can be suppressed when the particles are nano-sized.[94] In this case, each individual particle remains monophasic.

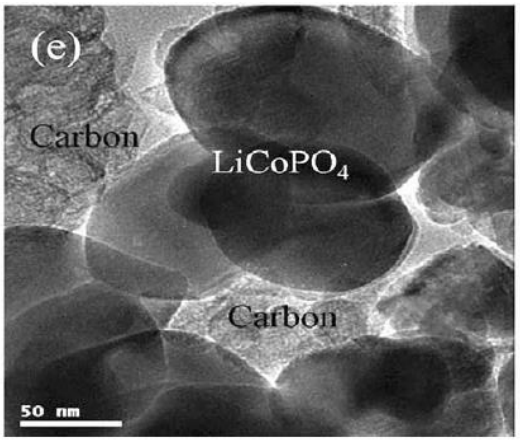

Figure 1.22 – TEM image of the nano-sized composite electrode. Reproduced from reference[93] with permission

An attempt to control the particle size through hydrothermal synthesis was conducted in 2009 by Dingguo *at el* by using poly(n-vinylpyrrolidone) (PVP) as a dispersant. The $LiCoPO_4$ particles that were produced were micro-rods that were 500 nm in length and 5 μm in length. However, the discharge capacity of these rods was 65 mA h g^{-1} at 0.1 C. Spherical nanoporous composite microparticles were synthesised by Richard *et. al;* these consisted of ~70 nm primary particles agglomerated into micron-sized spheres with an average pore size of 68 nm. These particles gave a discharge of 123 mA h g^{-1} at 0.1 C and reported excellent cycling behaviour, however only the first 20 cycles were seen within the report.[95] Plate-like $LiCoPO_4$ nanoparticles were synthesised in 2012 through a supercritical solvothermal method that were 50-200 nm in width and 100 – 300 nm in length. These plates gave a discharge capacity of ~95 mA h g^{-1} at 0.1 C, and showed capacity fade over 20 cycles.[96]

To improve the electrochemical properties, $LiCoPO_4$ was doped with manganese to produce $LiCo_{0.5}Mn_{0.5}PO_4$ through a hydrothermal route. It was suggested that the use of manganese reduces the particle size, from roughly 500 nm to 100 nm, and gave a discharge capacity of 126 mA h g^{-1} at 0.05 C.[97] The use of manganese within the system

can also enhance lattice conductance generating larger diffusion channels due to an expanded unit cell, resulting in higher lithium diffusivity.[98] Yttrium doped $LiCoPO_4$ (x = 0.01) cathodes were produced through a simple sol-gel based route by Wei *et al*. in 2013 and produced high discharge capacities of 154 mA h g^{-1} at 0.1 C, however severe capacity fade was observed across 20 cycles and the plateaus are not as well defined.[99] Yttrium doping improved the electrical conductivity of $LiCoPO_4$ by an order of magnitude, as well as enlarged the lattice volume of the unit cell.

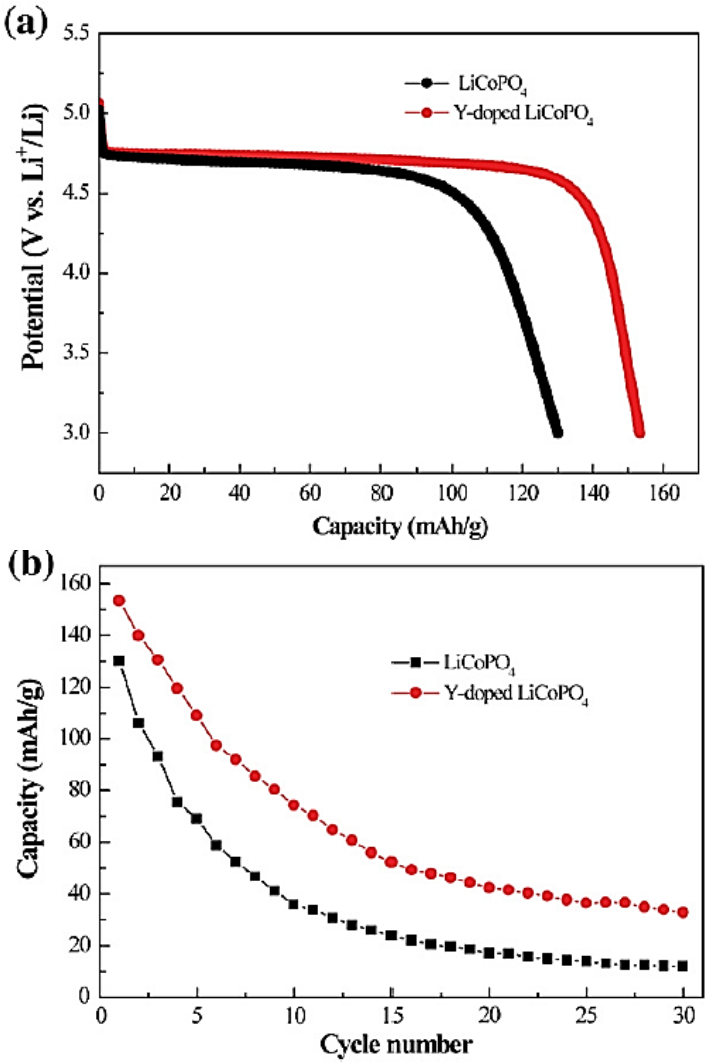

Figure 1.23 – Typical discharge profiles and cycling behaviour of pure and yttrium doped $LiCoPO_4$ samples. Reproduced from reference[99] with permission.

Further *in-situ* XRD studies in 2014 combined with ^{31}P and ^{7}Li NMR proved the existence of an intermediate phase of composition $Li_{2/3}CoPO_4$.[100] Up until this point, the nature of the intermediate phase was discussed controversially in the literature. Bramnik *et al* originally reported the existence of a $Li0.70CoPO_4$ phase based on the previous *in-situ* studies mentioned[92] whilst Ju *et al.* stated a composition of

$Li_{0.20\text{-}0.45}CoPO_4$ as the intermediate phase.[101] However in the latter case, the lithium content was derived from electrochemical data, which can be misleading due to side reactions consuming a non-negligible amount of charge. The phase evolution of phases A, B and C was refined with lattice volumes of 283, 278 and 266 Å respectively. During charge, it was proposed that delithiation is selective, with different arrangements of the Li vacancies being possible. **Figure 1.24** depicted an arrangement whereby the channels along the *b* axis were emptied in a way that alternating layers along the *c* direction are formed with full or empty Li sites in a 2:1 stacking sequence. Due to the partly oxidised cobalt, there are now two different lithium and phosphate environments. In the same year, Grey *et al.* published similar *in-situ* and NMR findings on $LiCoPO_4$ with the existence of a $Li_{2/3}CoPO_4$ phase, with similar lattice volumes for each phase being reported.[102]

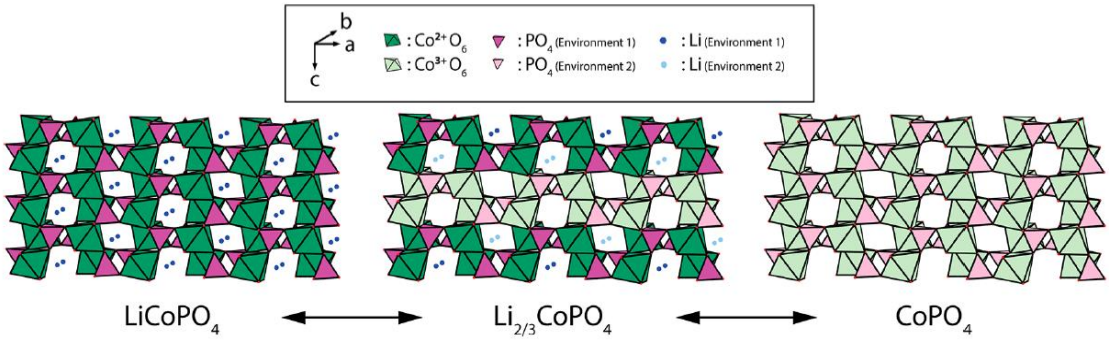

Figure 1.24 – Proposed charging/discharging mechanism of $LiCoPO_4$. Reproduced from reference[100] with permission.

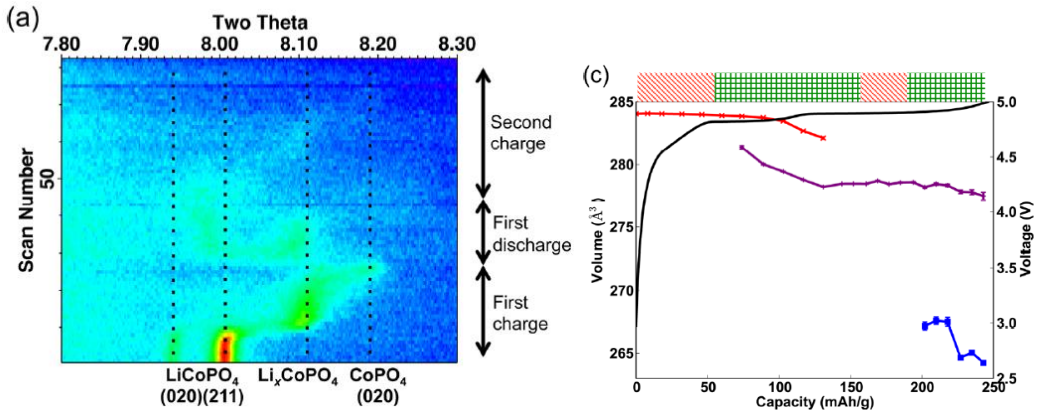

Figure 1.25 – Contour profile map showing the different phases present during charge, along with the unit cell volume lattice parameter changes. Reproduced from reference[102] with permission.

1.7.5 High Voltage Systems; Spinel-Type *Vs.* Polyanion Oxides

The best performing cathode material $LiNi_{0.5}Mn_{1.5}O_4$ allows for an operational voltage in the range of 4.7 – 4.8 *vs.* Li/Li^+,[103] and has been reported to demonstrate high cyclability (> 500 cycles 10 C) with marginal capacity fade through modification with a trace amount of ruthenium.[77] High voltage cobalt based polyanion oxides (e.g. $LiCoPO_4$) show substantially lower practical capacities than spinels,[72,104] but they do exhibit a higher operational voltage which is close to or even higher than 5 V *vs.* Li/Li^+.[105] However, it has been shown within the literature that there is substantial capacity fade after just 30 cycles.[106]

Regarding safety, $LiNi_{0.5}Mn_{1.5}O_4$ demonstrates a fair thermal stability of up to 250 °C,[107] whereas the thermal decomposition of $LiCoPO_4$ starts at temperatures below 200 °C.[108]

A fair conclusion, would be to acknowledge that although the polyanion compounds offer considerable potential for extending the cathode working potential up to 5 V *vs.* Li/Li^+ and even beyond that, currently these compounds are exceeded in practical charge capacity, cyclability and safety by the spinel-type high voltage cathode materials.[12] Much work must be continued on the enhancement of $LiCoPO_4$ based electrodes.

1.8 Summary

Lithium-ion batteries have been extensively studied, with different lithium intercalating compounds being introduced over the last 60 years. High voltage lithium-ion technology has recently been explored as a possible route to increase the energy density of battery systems, with $LiCoPO_4$ still being a relatively novel cathode material that has promise to be a leading candidate in the battery market.

The stability of the organic electrolytes is proving to a difficult problem to overcome above 4.5 V *vs.* Li/Li^+ for all high voltage battery materials. The interesting phase change processes that occur within $LiCoPO_4$ on charge and discharge is still yet to be fully resolved, and there are still many different investigations that need to be explored within the $LiCoPO_4$, such as metal doping's and different particle coatings.

This research project will focus on fully resolving the charge and discharge profile, and investigate the poor cycle life of the $LiCoPO_4$ through a variety of different techniques. Different electrolytes will be tested on $LiCoPO_4$, however this will not be the main purpose of the project, as the literature suggests that there still no known electrolytes that can be used in commercial high voltage lithium-ion batteries.

1.9 Organisation of Thesis

The following 6 chapters contain as follows:

Chapter 2 – Details of experimental procedures and characterisation methods

Chapter 3 – Initial insight into high voltage cathode materials, exploring different cathode materials and optimising experimental techniques.

Chapter 4 – Investigation into $LiCoPO_4$ composite electrodes. Exploring different synthesis routes, the origin of poor cycle life, different particle coatings and rate testing.

Chapter 5 – Insight into using a wide range of different high voltage electrolytes and doping manganese into the $LiCoPO_4$ system.

Chapter 6 – *in-situ* XRD studies of $LiCoPO_4$ composite electrodes and *ex-situ* XANES studies.

Chapter 7 – Conclusions and proposed further work

1.10 References

1 A. Yoshino, Lithium-Ion Batteries, Elsevier, 2014, 1–20.

2 D. Larcher, S. Beattie, M. Morcrette, K. Edström, J.-C. Jumas and J.-M. Tarascon, J. Mater. Chem., 2007, **17**, 3759.

3 J. M. Tarascon and M. Armand, Nature, 2001, **414**, 359–67.

4 R. R. Chianelli, J. C. Scanlon and A. H. Thompson, Mater. Res. Bull., 1975, **10**, 1379–1382.

5 J. O. Besenhard, J. Gurtler, P. Komenda and M. Josowicz, Proceedings of the Symposium on Primary and Secondary Ambient Temperature Lithium Batteries, Electrochem. Soc., Pennington, NJ, USA, 1988, 618–626.

6 Y. Nishi, J. Power Sources, 2001, **100**, 101–106.

7 P. G. Bruce, Chem. Commun., 1997, **19**, 1817.

8 Grant M. Ehrlich, Handbook Of Batteries, McGraw-Hill, 2002.

9 R. Yazami and P. Touzain, J. Power Sources, 1983, **9**, 365–371.

10 R. Yazami, Electrochim. Acta, 1999, **45**, 87–97.

11 Z. Ogumi and M. Inaba, Advances in Lithium-Ion Batteries, 2002.

12 A. Kraytsberg and Y. Ein-Eli, Adv. Energy Mater., 2012, **2**, 922–939.

13 A. R. West, in Solid state electrochemistry, ed. P. G. Bruce, Cambridge University Press, Cambridge, 1994, 7–42.

14 J. R. Owen, Chem. Soc. Rev., 1997, **26**, 259.

15 R. A. Huggins, Advanced Batteries, Springer, 2009.

16 G.-A. Nazri and G. Pistoia, Lithium Batteries: Science and Technology, Springer, New York, 2009.

17 C. Vincent, in Modern Batteries, Elsevier, 1997, 18–64.

18 R. Malik, F. Zhou and G. Ceder, Nat. Mater., 2011, **10**, 587–90.

19 M. S. Whittingham, Chem. Rev., 2004, **104**, 4271–4302.

20 B. L. Ellis, K. T. Lee and L. F. Nazar, Chem. Mater., 2010, **22**, 691–714.

21 K. Xu, Chem. Rev., 2004, **104**, 4303–4418.

22 E. Peled, J. Electrochem. Soc., 1979, **126**, 2047.

23 E. Peled, J. Electrochem. Soc., 1997, **144**, L208.

24 M. Nie, D. Chalasani, D. P. Abraham, Y. Chen, A. Bose and B. L. Lucht, J. Phys. Chem. C, 2013, **117**, 1257–1267.

25 J. F. Browning, L. Baggetto, K. L. Jungjohann, Y. Wang, W. E. Tenhaeff, J. K. Keum, D. L. Wood and G. M. Veith, ACS Appl. Mater. Interfaces, 2014, **6**, 18569–18576.

26 G. Cherkashinin, M. Motzko, N. Schulz, T. Späth and W. Jaegermann, Chem. Mater., 2015, **27**, 2875–2887.

27 N. Yabuuchi, K. Yoshii, S.-T. Myung, I. Nakai and S. Komaba, J. Am. Chem. Soc., 2011, **133**, 4404–4419.

28 D. Aurbach, M. Daroux, P. Faguy and E. Yeager, J. Electroanal. Chem. Interfacial Electrochem., 1991, **297**, 225–244.

29 D. G. Kwabi, N. Ortiz-Vitoriano, S. A. Freunberger, Y. Chen, N. Imanishi, P. G. Bruce and Y. Shao-Horn, MRS Bull., 2014, **39**, 443–452.

30 B. D. McCloskey, D. S. Bethune, R. M. Shelby, G. Girishkumar and A. C. Luntz, J. Phys. Chem. Lett., 2011, **2**, 1161–1166.

31 S. A. Freunberger, Y. Chen, Z. Peng, J. M. Griffin, L. J. Hardwick, F. Bardé, P. Novák and P. G. Bruce, J. Am. Chem. Soc., 2011, **133**, 8040–8047.

32 M. Gauthier, T. J. Carney, A. Grimaud, L. Giordano, N. Pour, H.-H. Chang, D. P. Fenning, S. F. Lux, O. Paschos, C. Bauer, F. Maglia, S. Lupart, P. Lamp and Y. Shao-Horn, J. Phys. Chem. Lett., 2015, **6**, 4653–4672.

33 M. Winter and R. J. Brodd, Chem. Rev., 2004, **104**, 4245–4270.

34 M. M. Thackeray, C. Wolverton and E. D. Isaacs, Energy Environ. Sci., 2012, **5**, 7854.

35 Z. Zhang, L. Hu, H. Wu, W. Weng, M. Koh, P. C. Redfern, L. A. Curtiss and K. Amine, Energy Environ. Sci., 2013, **6**, 1806-1810.

36 A. Kraytsberg and Y. Ein-Eli, Adv. Energy Mater., 2012, **2**, 922–939.

37 R. Gupta and A. Manthiram, J. Solid State Chem., 1996, **121**, 483–491.

38 H. Li and H. Zhou, Chem. Commun. (Camb)., 2012, **48**, 1201–17.

39 A. D. Spong, G. Vitins and J. R. Owen, J. Electrochem. Soc., 2005, **152**, A2376.

40 J. W. Fergus, J. Power Sources, 2010, **195**, 939–954.

41 T. Ohzuku and R. J. Brodd, J. Power Sources, 2007, **174**, 449–456.

42 K. Mizushima, P. Jones, P. Wiseman and J. Goodenough, Solid State Ionics, 1981, **3-4**, 171–174.

43 G. G. Amatucci, J. Electrochem. Soc., 1996, **143**, 1114.

44 T. Ohzuku, J. Electrochem. Soc., 1994, **141**, 2972.

45 J. N. Reimers, J. Electrochem. Soc., 1992, **139**, 2091.

46 Z. Chen, Z. Lu and J. R. Dahn, J. Electrochem. Soc., 2002, **149**, A1604.

47 D. Aurbach, B. Markovsky, A. Rodkin, E. Levi, Y. . Cohen, H.-J. Kim and M. Schmidt, Electrochim. Acta, 2002, **47**, 4291–4306.

48 A. Van der Ven, J. Electrochem. Soc., 1998, **145**, 2149.

49 M. M. Thackeray, P. J. Johnson, L. A. de Picciotto, P. G. Bruce and J. B. Goodenough, Mater. Res. Bull., 1984, **19**, 179–187.

50 S. Priya and D. J. Inman, Eds., Energy Harvesting Technologies, Springer US, Boston, MA, 2009.

51 D. Capsoni, M. Bini, G. Chiodelli, P. Mustarelli, V. Massarotti, C. B. Azzoni, M. C. Mozzati and L. Linati, J. Phys. Chem. B, 2002, **106**, 7432–7438.

52 M. M. Thackeray, Prog. Solid State Chem., 1997, **25**, 1–71.

53 P. P. Prosini, Iron Phosphate Materials as Cathodes for Lithium Batteries, Springer London, London, 2011.

54 R. A. Meyers, Ed., Encyclopedia of Sustainability Science and Technology, Springer New York, New York, NY, 2012.

55 M. M. Thackeray, W. I. F. David, P. G. Bruce and J. B. Goodenough, Mater. Res. Bull., 1983, **18**, 461–472.

56 M. M. Doeff, Springer Science+Business Media New York, 2013, p. 17.

57 A. Yamada and M. Tanaka, Mater. Res. Bull., 1995, **30**, 715–721.

58 Y. Xia, J. Electrochem. Soc., 1997, **144**, 2593.

59 J. M. Tarascon, J. Electrochem. Soc., 1991, **138**, 2859.

60 J. M. Tarascon, J. Electrochem. Soc., 1994, **141**, 1421.

61 D. Guyomard and J. Tarascon, Solid State Ionics, 1994, **69**, 222–237.

62 M. Takahashi, Solid State Ionics, 2002, **148**, 283–289.

63 A. K. Padhi, J. Electrochem. Soc., 1997, **144**, 1188.

64 P. S. Herle, B. Ellis, N. Coombs and L. F. Nazar, Nat. Mater., 2004, **3**, 147–52.

65 P. P. Prosini, D. Zane and M. Pasquali, Electrochim. Acta, 2001, **46**, 3517–3523.

66 H. Huang, S.-C. Yin and L. F. Nazar, Electrochem. Solid-State Lett., 2001, **4**, A170.

67 S.-Y. Chung, J. T. Bloking and Y.-M. Chiang, Nat. Mater., 2002, **1**, 123–8.

68 M. R. Roberts, G. Vitins, G. Denuault and J. R. Owen, J. Electrochem. Soc., 2010, **157**, A381.

69 A. Yamada, H. Koizumi, N. Sonoyama and R. Kanno, Electrochem. Solid-State Lett., 2005, **8**, A409.

70 Y.-M. Song, J.-G. Han, S. Park, K. T. Lee and N.-S. Choi, J. Mater. Chem. A, 2014, **2**, 9506–9513.

71 N. Amdouni, K. Zaghib, F. Gendron, A. Mauger and C. M. Julien, J. Magn. Magn. Mater., 2007, **309**, 100–105.

72 G. Q. Liu, L. Wen and Y. M. Liu, J. Solid State Electrochem., 2010, **14**, 2191–2202.

73 S. Patoux, L. Daniel, C. Bourbon, H. Lignier, C. Pagano, F. Le Cras, S. Jouanneau and S. Martinet, J. Power Sources, 2009, **189**, 344–352.

74 J.-H. Kim, S.-T. Myung, C. S. Yoon, S. G. Kang and Y.-K. Sun, Chem. Mater., 2004, **16**, 906–914.

75 Y. Gao, K. Myrtle, M. Zhang, J. N. Reimers and J. R. Dahn, Phys. Rev. B, 1996, **54**, 16670–16675.

76 U. Lafont, C. Locati, W. J. H. Borghols, A. Łasińska, J. Dygas, A. V. Chadwick and E. M. Kelder, J. Power Sources, 2009, **189**, 179–184.

77 H. Wang, H. Xia, M. O. Lai and L. Lu, Electrochem. commun., 2009, **11**, 1539–1542.

78 S. Okada, S. Sawa, M. Egashira, J. Yamaki, M. Tabuchi, H. Kageyama, T. Konishi and A. Yoshino, J. Power Sources, 2001, **97-98**, 430–432.

79 J. Wolfenstine and J. Allen, J. Power Sources, 2004, **136**, 150–153.

80 K. Amine, Electrochem. Solid-State Lett., 1999, **3**, 178.

81 M. Amine, K. Yasuda, H. Yamachi, in Lithium Batteries: Proceedings of the International Symposium, 1999, **99**, 311–325.

82 S. Okada, S. Sawa, M. Egashira, J. Yamaki and M. Tabuchi, 2001, **98**, 432–434.

83 J. M. Lloris, C. Pérez Vicente and J. L. Tirado, Electrochem. Solid-State Lett., 2002, **5**, A234.

84 A. Eftekhari, J. Electrochem. Soc., 2004, **151**, A1456.

85 N. Bramnik, K. Bramnik, T. Buhrmester, C. Baehtz, H. Ehrenberg and H. Fuess, J. Solid State Electrochem., 2004, 8, 562.

86 D. Shanmukaraj and R. Murugan, Ionics., 2004, **10**, 88–92.

87 X. Huang, J. Ma, P. Wu, Y. Hu, J. Dai, Z. Zhu, H. Chen and H. Wang, Mater. Lett., 2005, **59**, 578–582.

88 J. Wolfenstine, U. Lee, B. Poese and J. L. Allen, J. Power Sources, 2005, **144**, 226–230.

89 J. Wolfenstine, J. Power Sources, 2006, **158**, 1431–1435.

90 J. Wolfenstine, J. Read and J. L. Allen, J. Power Sources, 2007, **163**, 1070–1073.

91 N. N. Bramnik, K. G. Bramnik, C. Baehtz and H. Ehrenberg, J. Power Sources, 2005, **145**, 74–81.

92 N. N. Bramnik, K. Nikolowski, C. Baehtz, K. G. Bramnik and H. Ehrenberg, Chem. Mater., 2007, **19**, 908–915.

93 H. H. Li, J. Jin, J. P. Wei, Z. Zhou and J. Yan, Electrochem. commun., 2009, **11**, 95–98.

94 B. Orvananos, H.-C. Yu, R. Malik, A. Abdellahi, C. P. Grey, G. Ceder and K. Thornton, J. Electrochem. Soc., 2015, **162**, A1718–A1724.

95 J. Liu, T. E. Conry, X. Song, L. Yang, M. M. Doeff and T. J. Richardson, J. Mater. Chem., 2011, **21**, 9984.

96 M. K. Devaraju, D. Rangappa and I. Honma, Electrochim. Acta, 2012, **85**, 548–553.

97 J. F. Ni, Y. Han, J. Liu, H. Wang and L. Gao, ECS Electrochem. Lett., 2012, **2**, A3–A5.

98 J. Ni, Y. Kawabe, M. Morishita, M. Watada and T. Sakai, J. Power Sources, 2011, **196**, 8104–8109.

99 H. Li, Y. Wang, X. Yang, L. Liu, L. Chen and J. Wei, Solid State Ionics, 2014, **255**, 84–88.

100 M. Kaus, I. Issac, R. Heinzmann, S. Doyle, S. Mangold, H. Hahn, V. S. K. Chakravadhanula, C. Kübel, H. Ehrenberg and S. Indris, J. Phys. Chem. C, 2014, **118**, 17279–17290.

101 J. Wu, Z. Li, L. Ju, D. Li, J. Zheng and Y. Xu, Rare Met. Mater. Eng., 2013, **42**, 684–687.

102 F. C. Strobridge, R. J. Clément, M. Leskes, D. S. Middlemiss, O. J. Borkiewicz, K. M. Wiaderek, K. W. Chapman, P. J. Chupas and C. P. Grey, Chem. Mater., 2014, **26**, 6193–6205.

103 R. Santhanam and B. Rambabu, J. Power Sources, 2010, **195**, 5442–5451.

104 T. Muraliganth and A. Manthiram, J. Phys. Chem. C, 2010, **114**, 15530–15540.

105 S. Okada, M. Ueno, Y. Uebou and J. Yamaki, J. Power Sources, 2005, **146**, 565–569.

106 E. Markevich, R. Sharabi, H. Gottlieb, V. Borgel, K. Fridman, G. Salitra, D. Aurbach, G. Semrau, M. a. Schmidt, N. Schall and C. Bruenig, Electrochem. commun., 2012, **15**, 22–25.

107 S.-W. Oh, S.-H. Park, J.-H. Kim, Y. C. Bae and Y.-K. Sun, J. Power Sources, 2006, **157**, 464–470.

108 N. N. Bramnik, K. Nikolowski, D. M. Trots and H. Ehrenberg, Electrochem. Solid-State Lett., 2008, **11**, A89.

Chapter 2:

Experimental Techniques

2.1 General Methods

All chemicals were available within the laboratory, provided by the industrial sponsor or acquired from leading suppliers.

2.2 Solid State Synthesis

Solid state synthesis is a widely used method for constructing inorganic positive electrode materials. The initial solid state method within this report was to heat the reactant metal salts together for an extended period of time at high temperature. The material is usually ground to ensure a homogenous mixture with good contact between the reactant crystal faces before heating. The heating step allows for the migration of ions between these interfaces as the lattice formation energy is overcome, therefore creating the formation of new structures.

2.3 Solvothermal Synthesis

Solvothermal synthesis is a method similar to solid state synthesis apart from the heating step which requires the reactants to remain within solution. These strenuous conditions require an autoclave, which can be heated under pressure to ensure the reactants remain in solution during heating within an isolated system. Different solvents can be used inside the autoclave at different concentrations to control the size and shape of the particles being formed. This allows for complete control of the particle morphology when forming particular inorganic compounds.

2.4 Electrochemical Cell Preparation

2.4.1 PTFE Pellets

The PTFE pellets were made by manually mixing the cathode material powder with carbon and PTFE in pestle and mortar. Typically 0.2g of $LiCoPO_4$ (75 %) was ground with acetylene black (20 % by weight) and then PTFE (5 % by weight) was added. The solid lump was then hand rolled (Durston Rolling Mill) into a film of ~90 μm and cut into disks 12 mm in diameter. The pellets were dried at 120 °C under vacuum overnight to remove any moisture and then assembled into a Swagelok half-cell.

2.4.2 PVDF Inks

PVDF inks were made via a solution mixing method. The PVDF binder (10% by weight) would be pre-dissolved in N-Methyl-2-pyrrolidone (NMP) and acetylene black was then be added to the mixture with a minimum amount of NMP added (~1.5 ml) and stirred magnetically until a good mix was achieved. The active material would then be added in small aliquots whilst continually mixing. Typically the mixtures would contain 76 % active material, 12 % carbon and 12 % PVDF by weight. The mixture would then be subjected to homogenisation using a high speed shear stirrer (IKA T25) at 20,000 rpm for 5 minutes. The high impact mixing helps to bring the carbon and active material particles together and any larger solid agglomerates are also dispersed. The slurry mixture was then cast onto aluminium foil (125 μm thick, Temper annealed, 99.0 % purity, Advent Research Materials Ltd.) utilising a K bar hand coater (RK PrintCoat Instruments Ltd.) and dried at 80 °C to remove any excess solvent. These 11 mm (diameter) circular disks were then dried under vacuum at 120 °C for a minimum of 12 hours before being transferred to the glovebox and assembled into a Swagelok half-cell.

2.4.3 Preparation of Electrolyte Solutions

Electrolyte solutions other than LP57 (BASF) were prepared in-house. Carbonate solvents were purchased in the purest available form from Sigma-Aldrich. Solvents were stored in sealed polyethylene containers and dried using molecular sieves within the glove box. Lithium hexafluorophosphate ($LiPF_6$, Sigma-Aldrich, battery grade ≥99.99 %) was dissolved in mixtures of carbonate solvents. Once prepared the solutions were stored in polyethylene containers inside the glove box.

2.4.4 Method Development

The accuracy of the electrochemical data collected is dependent on obtaining an accurate mass measurement. A common method used to calculate the composite electrode mass was to weigh the PTFE pellet directly on the balance, and calculate an average disc mass (weighed out three times individually). For the PVDF slurries, a custom designed jig was produced to hold the pre-weighed metal disks. The disk would fit into circular drilled sections of the jig which is flush to the jig surface, allowing for an evenly spread slurry film to be cast over the surface. This method ensured each individual composite electrode mass was known on each individual disk.

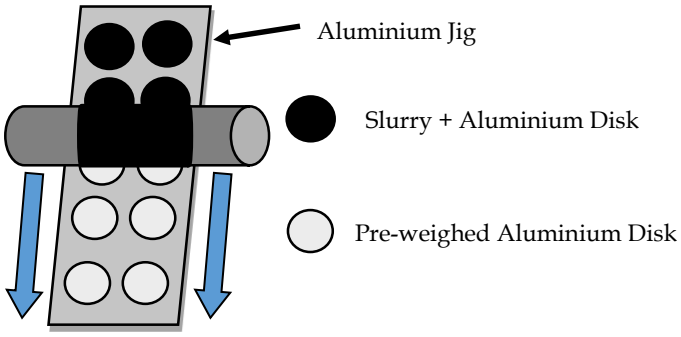

Figure 2.1 - Image of the aluminium jig and how the ink slurries were cast onto the foil.

2.5 Electrochemical Cell Construction

Cell design is an important aspect when conducting electrochemical experiments. The size, geometry and materials used can all have an impact on the results that are obtained. Cells commonly used in lithium-ion battery research include custom design cells or mainly commercial coin cells, pouch cells or Swagelok cells. Within this research, the use of Swagelok cells provided the best combination of properties to allow for the collection of accurate, reproducible and comparable data.

2.5.1 Swagelok Cell Design

The Swagelok cell components including the housing, ferrules and connectors used for this work was purchased directly from the manufacturer. The cells were constructed out of PFA (Perfluoroalkoxy alkanes) polymer. Pistons and current collectors were

machined from aluminium and copper by the workshop in-house. **Figure 2.2** displays a diagram of the components used to construct electrochemical cells utilising Swagelok components.

The electrode stack consisted of the composite electrode, 2 glass fiber separators (Whatman GF/F grade glass fiber), electrolyte and a counter electrode consisting of lithium metal (Rockwood Lithium GmbH). $LiCoPO_4$ composite electrodes were tested by using either two or three electrode Swagelok cells. The composite electrodes were dried under vacuum at 120 °C overnight and transferred into a glove box containing argon gas. (Ultrashield 99.999 %) with oxygen and moisture levels below 10 ppm.

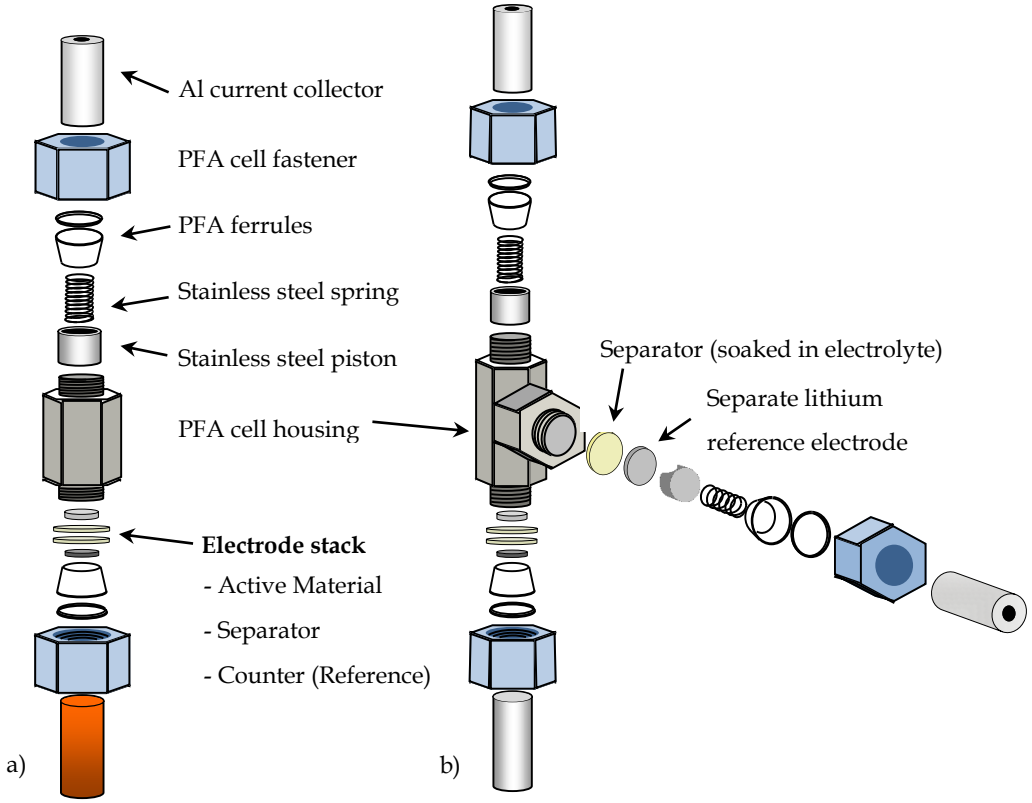

Figure 2.2 – Schematic of Swagelok type cells a) two electrode b) three electrode.

The glass fibre disks that act as separators were saturated with 8 drops of electrolyte inside the Swagelok cells during construction. The electrolyte used if not otherwise described was 1 M solution of lithium hexafluorophosphate dissolved in a 3:7 weight ratio of ethylene carbonate and ethylmethyl carbonate (1 M $LiPF_6$ EC:EMC). This electrolyte was purchased directly from the manufacturer (BASF) and is commonly known as LP57.

2.6 Electrochemical Testing

Constructed cells were transferred out of the glove box and stored inside a temperature controlled chamber set at 25 °C. The cells were then connected to a VMP2 multi-channel potentiostat (Princeton Applied Research) for electrochemical characterisation.

2.6.1 Constant Current Chronopotentiometry Technique

All potential values quoted within this work are measured *vs.* a lithium reference potential (Li/Li^+) unless stated otherwise.

2.6.2 Theory

Constant current chronopotentiometry is the application of a constant current to an electrode, whilst continually measuring the potential of the electrode *vs.* a reference potential. Galvanostatic cycling is a common name given to this technique used within battery cycling to simulate the charge and discharge of an electrochemical cell or battery.

When a constant current is applied to an electrode, the electro-active species undergoes oxidation or reduction within the operational voltage range. After either a specified period of time/charge has passed or a voltage limit is reached, the current is then reversed and the reverse reaction occurs. Electrodes are cycled under various conditions to investigate the properties of electrodes and electrochemical systems as a whole.

2.6.3 Method

Galvanostatic cycling of Swagelok cells was conducted utilising a VMP2 Biologic poentiostat (Princeton Applied Research). The potentiostat was used to apply either a positive or negative current to the working electrode of the cell and to monitor the voltage of the electrode with respect to a reference potential. Within this work, lithium metal was used as the negative and reference electrode. The reversible redox potential of lithium is a commonly used reference potential in lithium battery research. Calculation of the current to be applied to the cell is related to the mass and the theoretical capacity of the active material within the composite electrode.

2.6.4 Electrochemical Impedance Spectroscopy (EIS)

2.6.4.1 Theory

Electrochemical impedance spectroscopy is the measure of the opposition that a system presents to a current when a voltage is applied.[1] A sinusoidal voltage perturbation is applied to the circuit over a range of frequencies, and analysis of the changes in the current response allows for the investigation of the electrochemical processes occurring over various timescales via non-liner processes.

The small applied amplitude AC voltage signal can be represented by **Equation 2.1.**

$$E(t) = E_0 \sin(\omega t) \qquad \textbf{Equation 2.1}$$

E(t) = Potential at time t, E_0 = amplitude, ω = radial frequency ($2\pi f$), t = time, f = frequency (Hz)

The signal response from this applied amplitude AC voltage is shown in **Equation 2.2**.

$$I(t) = I_0 \sin(\omega t + \phi) \qquad \textbf{Equation 2.2}$$

I(t) = current at time t, I_0 = amplitude, ω = radial frequency ($2\pi f$), t = time, f = frequency (Hz), ϕ = phase

Figure 2.3 shows a diagram of an applied AC perturbation signal and the corresponding response signal.

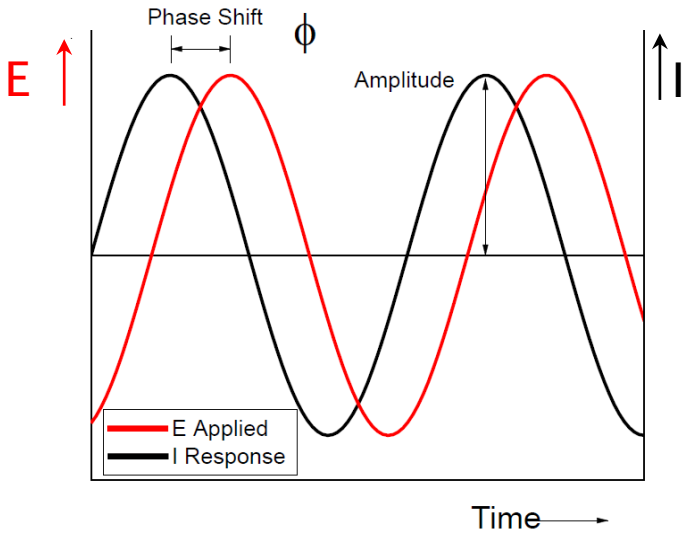

Figure 2.3 – Diagram of an applied small amplitude AC perturbation signal and response signal.

The impedance, Z, is defined by **Equation 2.3.**

$$Z = \frac{E_t}{I_t} = \frac{E_0 sin\,(\omega t)}{I_0 sin\,(\omega t + \phi)} = Z_0 \frac{sin\,(\omega t)}{sin\,(\omega t + \phi)} \qquad \textbf{Equation 2.3}$$

Z = impedance, E_t = potential at time t (V), I_t = current at time t (A), E_0 = applied signal amplitude, I_0 = response signal amplitude, ω = radial frequency ($2\pi f$), t = time, f = frequency (Hz), ϕ = phase, Z_0 = magnitude of impedance.

Using Euler's formula, Z can be displayed in complex notation as displayed in **Equation 2.4.**

$$Z = Z_0 (cos\,\phi + j \sin\phi) = Z' + j\,Z'' \qquad \textbf{Equation 2.4}$$

Z = impedance, Z_0 = magnitude of impedance, $j = \sqrt{-1}$, ϕ = phase, Z' = real component of impedance, Z'' = imaginary component of impedance.

The impedance spectrum can be plotted on a complex plane in terms of Z' and Z'' as displayed in **Figure 2.3**.

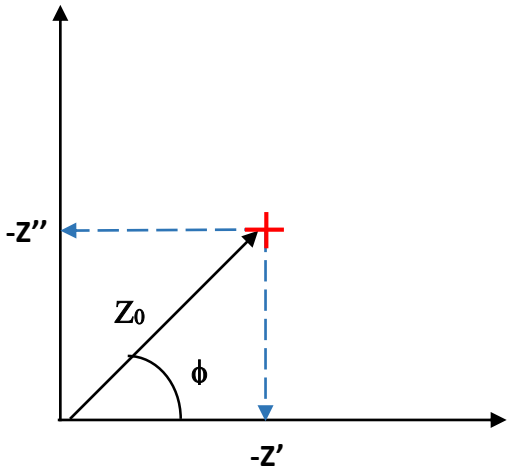

Figure 2.3 Complex plane plot displaying impedance. Z′ = real component, Z″ = imaginary component, Z_0 = magnitude of impedance, ϕ = phase.

Impedance spectra are commonly displayed using Nyquist and Bode plots. Within a Nyquist plot, the imaginary part is plotted *vs.* the real part. For a Bode plot, two plots are made of Z *vs.* frequency and ϕ *vs.* frequency. Both of these plots are then commonly modelled using a simplified equivalent circuit. These circuits are made up of simple components of known impedance responses.

Resistor

When a small AC potential is applied to a resistor, the current response from the potential is directly in phase and is related to Ohms law in **Equation 2.5**.

$$V_t = I_t R \qquad \textbf{Equation 2.5}$$

V_t, = voltage at time t (V), I_t = current at time t (A), R = resistance (Ω)

The impedance of a resistor corresponds directly to the resistance in **Equation 2.6**.

$$Z_R = R \qquad \textbf{Equation 2.6}$$

Z_R = impedance of a resistor, R = resistance (Ω)

Capacitor

For a capacitor, it is important to assume that no current ever flows between the two plates. When the AC potential is applied, the current constantly changes direction so the electrons keep forming on each plate changing between the current direction. There is an Ohms law equivalent equation for a capacitor which has an included time element in **Equation 2.7** and **Equation 2.8.**

$$V = I X_c \qquad \textbf{Equation 2.7}$$

$$X_c = \frac{1}{j\omega C} \qquad \textbf{Equation 2.8}$$

V = voltage (V), I = current (A), X_c = reactants, $j = \sqrt{-1}$, ω = radial frequency ($2\pi f$), C = capacitance (F)

Unlike a resistor, a capacity has a time element which is directly related to the reactants (resistive effect). At slower times, the charge builds up on the plate and impedes further charge that is close to the plate. However at faster times, this impedance is minimised because there is no time to have a build-up of charge on the plate because of the rapid alternating current changing the direction of charge on the plate. The impedance of a capacitor is purely imaginary and varies as a function of frequency.

For components in series the impedance response is additive. **Equation 2.9** shows how the impedance can be represented for a single resistor and capacitor in series.

$$Z_{RC\ series} = R + \frac{1}{j\omega C}$$ **Equation 2.9**

$Z_{RC\ series}$ = impedance of a resistor and capacitor in series, R = resistance (Ω), $j = \sqrt{-1}$, ω = radial frequency ($2\pi f$), C = capacitance (F)

For components in parallel, the inverse impedance is additive. The impedance response of a resistor and a capacitor in parallel is described by **Equation 2.10**.

$$\frac{1}{Z_{RC\ parallel}} = \frac{1}{R} + j\omega C$$ **Equation 2.10**

$Z_{RC\ parallel}$ = impedance of a resistor and capacitor in parallel, R = resistance (Ω), $j = \sqrt{-1}$, ω = radial frequency ($2\pi f$), C = capacitance (F)

Figure 2.4 displays a Nyquist plot showing the impedance response of different simple circuit element combinations.

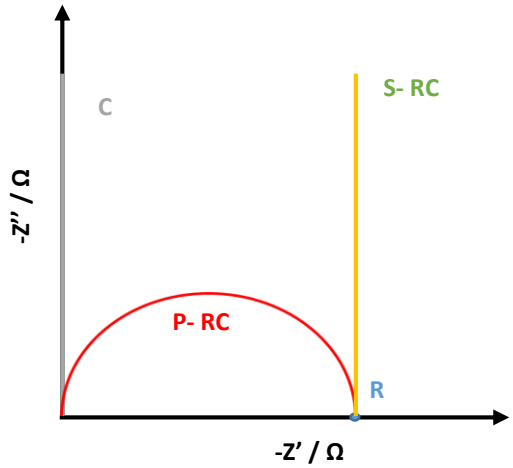

Figure 2.4 Nyquist plot displaying the impedance response of different simple circuit elements.

The capacitance is considered as an imaginary part so appears as a series of points along the imaginary y-axis. The resistance only has a real part and appears as a point along the x-axis. The different combinations of the circuit being in parallel or series leads to a resistive shift in the capacitance part or a semi-circle as shown respectively.

A constant phase element (CPE) is a single component that is used to fit impedance spectra when the capacitor part is non-ideal. A non-ideal capacitor is one that in practice is not perfect (i.e. charge may pass between the plates). The CPE can be represented by **Equation 2.11** and is displayed on a Nyquist plot in **Figure 2.5**.

$$Z_{CPE} = \frac{1}{Q(j\omega)^n}$$ **Equation 2.11**

Z_{CPE} = impedance of a CPE, Q = capacitance (when n = 1) ($s^n\ \Omega^{-1}$), $j = \sqrt{-1}$, ω = radial frequency ($2\pi f$), n = varies between 0 and 1 (0 = resistor, 1 = capacitor)

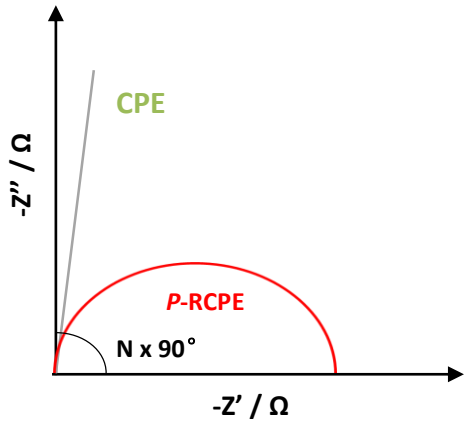

Figure 2.5 Nyquist plot displaying the impedance response of a CPE and parallel combination of a resistor showing a depressed semicircle.

At intermediate *n* values from **Equation 2.11**, CPE cannot be equated to a capacitor; however the capacitance of a parallel combination of a resistor and CPE can be calculated from the R-CPE time constant.

$$RQ = \tau^n$$ **Equation 2.12**

R = resistance (Ω), Q = ($S^n\ \Omega^{-1}$), τ = time constant (s), n = varies between 0 and 1

The time constant of a capacitor in parallel with a resistor is defined by **Equation 2.13**

$$\tau = RC$$ **Equation 2.13**

R = resistance (Ω), τ = time constant (s) $C = capacitance\ (F)$

Combining **Equation 2.12** and **Equation 2.13** gives **Equation 2.14**

$$RQ = (RC)^n$$ **Equation 2.14**

R = resistance (Ω), Q = ($S^n\ \Omega^{-1}$), $C = capacitance$ (F), n = varies between 0 and 1

The true capacitance can then be calculated using **Equation 2.15**

$$C = \frac{(R(Q))^{\frac{1}{n}}}{R}$$ **Equation 2.15**

R = resistance (Ω), Q = ($S^n\ \Omega^{-1}$), $C = capacitance$ (F), n = varies between 0 and 1

Another important element used to model diffusion behaviour is called the Warburg element. The Warburg element is a CPE element with an n value of 0.5. The impedance response of a Warburg element can be described by **Equation 2.16**.

$$Z_w = \sigma\omega^{-0.5} - j\omega\sigma^{-0.5} \qquad \textbf{Equation 2.16}$$

ZW = Warburg impedance, σ = Warburg coefficient, j = √-1, ω = radial frequency (2πf)

The Warburg coefficient, σ, describes the relative diffusion coefficients of the oxidised and reduced species and is described by **Equation 2.17**.

$$\sigma = \frac{RT}{n^2F^2A\sqrt{2}}\left(\frac{1}{D_O^{0.5}c_O^{blk}} + \frac{1}{D_R^{0.5}C_R^{blk}}\right) \qquad \textbf{Equation 2.17}$$

R = Gas constant (J K^{-1} mol^{-1}), T = Temperature (K) F = Faradays constant (96485 C mol^{-1}),
n = number of electrons transferred, A = electroactive area, (cm^2)
D_O = diffusion coefficient of oxidised species, D_R = diffusion coefficient of reduced species

The Warburg coefficient can be derived from the slope of Z′ and Z′′ *vs.* 1/0.5ω.

2.6.4.2 Method

Impedance measurements were obtained using a VMP potentiostat with built in EIS analyser (VMP2 Biologic, Princeton Applied Research). Three electrode Swagelok type cells were used and cells were allowed to rest for at least 1 hour prior to measurement. A three electrode Swagelok cell design was used because the extra lithium reference eliminates any impedance data of the counter electrode. There will be SEI formation on the counter lithium electrode, but not on the lithium reference because no current is passing through the reference electrode. A sinusoidal potential perturbation with a amplitude of 10 mV was used with a frequency range of 200 kHz to 2 mHz. Measurements were obtained in triplicate and averaged automatically by the software (EC-Lab). Ten points were measured per decade and the raw data was modelled using simple equivalent circuits using Z-View software (Scribner associates Inc).

2.7 GITT

Galvanostatic intermittent titration technique (GITT) is a procedure useful to retrieve both thermodynamics and kinetic parameters.[2] In a typical measurement, a GITT experiment would consist of a series of current pulses, each followed by a relaxation period in which no current passes through the cell.

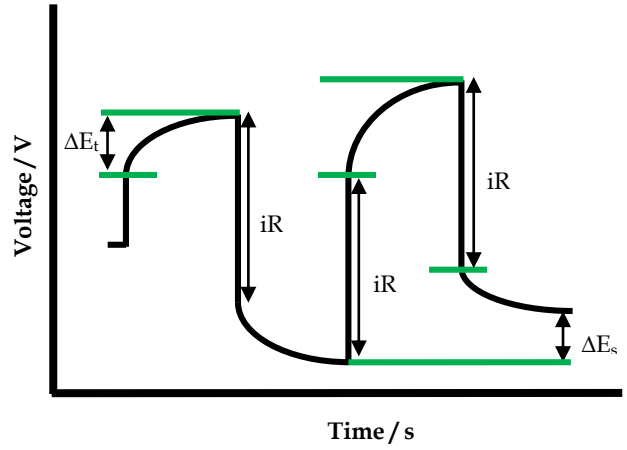

Figure 2.6 - Illustrated diagram showing two charge steps with an added relaxation time. The iR drop is highlighted, together with ΔE_t (during pulse) and ΔE_s (steady state).

During charge, a positive current will be applied and the cell potential will quickly increase from the open circuit potential to a value that is proportional to the iR drop. Afterwards, the potential will slowly increase due to the current being applied in order to maintain a constant concentration gradient in terms of lithium. When the pulse of current is switched off i.e. during the relaxation period, the composition in the electrode tends to become homogenous by lithium diffusion. Consequently the potential will first suddenly decrease to a value proportional to the iR drop, and then slowly decrease until the electrode has reached equilibrium. A secondary pulse can then be applied and the process is repeated. This sequence of pulses can be applied until the cell is fully charged. Upon discharge, the opposite holds true. The resistance from the iR drop is the sum of the uncompensated resistance (R_{un}) and the charge transfer resistance (R_{ct}).

2.7.1 Method

GITT cycling of Swagelok cells was conducted utilising a VMP2 Biologic poentiostat (Princeton Applied Research). A galvanostatic current was applied to the cell for 30 minutes with rest periods of 10 minutes in between each pulse.

2.8 Characterisation Techniques

2.8.1 Powder X-ray Diffraction

X-ray diffraction is a technique used to determine the structure and purity of a variety of crystalline materials. Monochromatic X-rays are fired at the sample and the exposure of the radiation to the ordered lattice of the crystalline solids gives rise to interference between the reflected waves. It is possible to derive the mean positions of the atoms as the direction of the scattering and relative intensities are specific to a crystal structure. Crystal structures have a regular array of atoms which X-rays can strike and scatter through the atoms electrons. An X-ray striking an electron produces secondary waves emanating from the electron (**Figure 2.7**). This elastic scattering produces waves that cancel each other out in most directions through destructive interference. Some waves however add constructively within certain specific directions. Constructive interference occurs between the X-rays when the difference in distance travelled between the reflected waves is an integer multiple of the incident wavelength. The angle at which constructive interference will occur is shown by the Bragg equation.[3]

$$\lambda = 2d_{hkl}sin\theta$$ **Equation 2.18**

λ =wavelength (nm), d_{hlj} = lattice spacing, θ = X-ray beam angle of incidence (degrees)

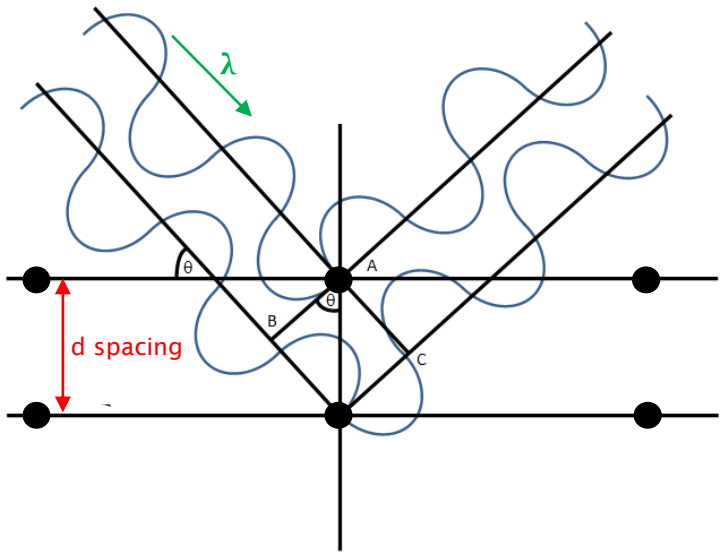

Figure 2.7 – Schematic demonstrating the principles of X-ray diffraction.

In powder X-ray diffraction a sample is exposed to a single wavelength of X-rays as the angle of incidence is swept between two angle limits. The position and number of reflections depend on the wavelength of the incidence X-rays, the cell parameters, crystal system and lattice type of the sample. If the crystallites making up a powdered specimen are small, the peaks within the diffraction pattern are broadened by an amount that is inversely proportional to the crystallite size.[4] The Scherrer equation is related to this theory.

$$B = \frac{k\,\lambda}{\epsilon\,cos\,\theta} \qquad \textbf{Equation 2.19}$$

B = average crystallite size (nm), k = constant related to crystallize size, λ = X-ray wavelength (nm) ε = peak width of the diffraction peak profile at half maximum height (rad) θ = Bragg angle (rad)

Where B is the peak width, ϵ is the apparent crystallite size, λ is the wavelength of the radiation, θ is the Bragg angle and K is the shape factor. The Scherrer equation is limited to nano-scale particles. The equation shows that as the crystallite size gets smaller, the peak size gets broader and that the crystallite size broadening is most pronounced at large angles. The apparent crystallite size in **Equation 2.19** assumes that the crystallites are of the same size, the true size of crystallites is in fact given by **Equation 2.20**.

$$p = K\epsilon \qquad \textbf{Equation 2.20}$$

P = true crystalline size (nm), K = Scherrer constant (dimensionless number), ε = apparent crystallite size (nm)

Where p is the true crystallite size, and K is the Scherrer constant. The true size of a crystallite is considered for crystallites that share the same shape. From knowing the average crystallite shape from another analysis, the correct value of K can be selected. Though the shapes of crystallites are often irregular, so they are often approximated as spherical shapes.[4] Extraction of crystallographic data from a known structure type is possible using the Rietveld refinement method.

2.8.1.1 Method

A Bruker D2 Phaser powder X-ray diffractometer with a Copper K_α X-ray source was used to collect X-ray diffraction patterns. Bragg-Brentano geometry was used, with a

selected 2-theta angle range between the X-ray source and detector throughout collection. The collection range was selected between 10 and 60 2-theta degrees. Increments of 0.012 2-theta were used with a step time of 0.6 seconds. Samples were rotated at a rate of 6 rotations per minute during collection. Bruker Eva software was used to interpret the data and the Rietveld refinements were fitted against crystal structure patterns found on the ICSD database.

2.8.2 Rietveld Refinement

Rietveld refinement is a program that uses a least squares method to refine an experimentally collected diffraction pattern against the known structural model which it acquired from literature. The method of least squares is a standard approach within data fitting to find the approximate solution over determined systems.[5,6] The method minimises the difference between an observed value and the fitted value provided by the model, adjusting the lattice parameters in the proposed structure. The refinement fitting process seemed complete upon no further significant changes to a unit cell, instrument and sample parameters with repetitive cycles, whilst maintaining a high quality fit to the data.

2.8.3 Synchrotron

X-ray adsorption measurements are almost always available at synchrotron radiation facilities. Bunches of electrons are accelerated by a linear accelerator and then fed into the inner booster ring that further accelerates them to near the speed of light and injects them into the outer storage ring. A series of bending magnets around the ring keep the electrons traveling in a closed loop. The conservation of angular momentum of the electrons results in the emission of synchrotron X-rays at tangents. These X-rays are highly intense, collimated and cover a wide range of energies.[7] A series of optics is then used to tune the X-rays to the desired energy and profile. Synchrotron based techniques are becoming increasingly important in heritage science and give an insight into structural changes that are occurring within systems during experimental applications.[8]

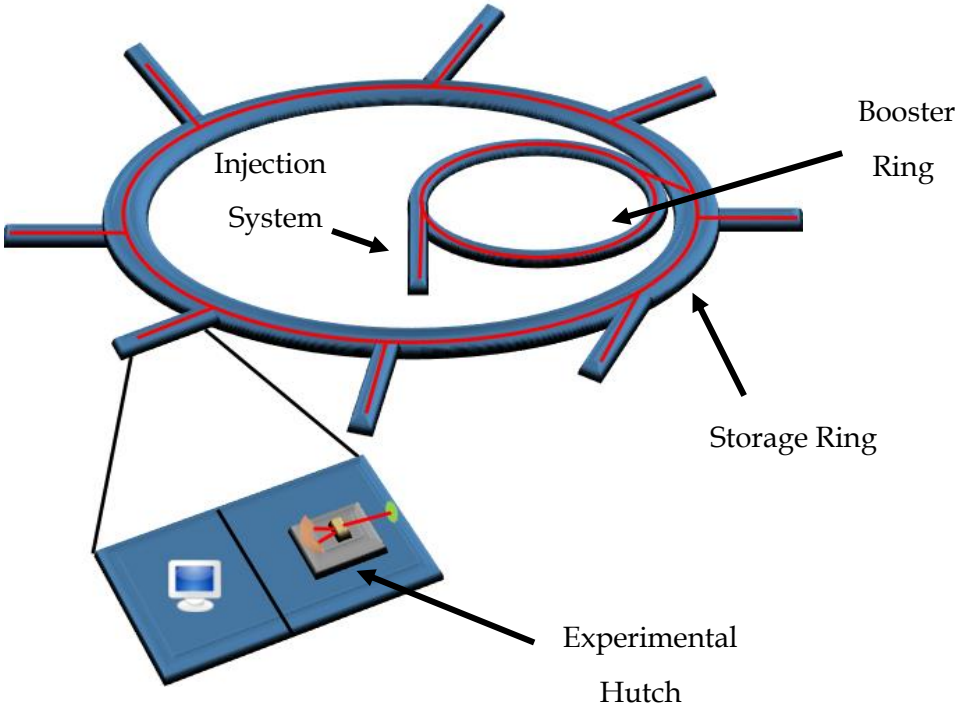

Figure 2.8 Schematic of a synchrotron beamline with an example experimental hutch.

2.8.3.1 Method

The electrochemical preparation for the *in-situ* cell was very similar to a typical Swagelok cell (described in more detail in **Section 6.2**). The same 8 mm diameter electrode pellets were used, but with a different ratio of the three components. A 50: 40: 10 weight % of $LiCoPO_4$, acetylene black and PTFE binder was used. These thin electrodes have a high dilution of active material and open pore structures so that they achieve a high level of homogeneity even with fast cycling rates, and the beam penetration is sufficient to evenly sample the entire electrode depth if required. The cell were assembled with two glass fibre separators soaked with eight drops of BASF LP57. The domed lithium metal was formed by compressing lithium foil into a PTFE mould, which was then punched out to 12 mm.

XRD patterns were collected using synchrotron radiation at Diamond Light Source (Oxford, U.K.) using Beamline I07. A 20 keV beam energy (wavelength) was used to collect patterns with a Pilatus 100k area detector. The area detector was used to collect frames of data was an exposure time of 1 minute (8 minutes rest) for galvanostatic cycling, and 10 seconds scans (45 seconds rest) for the GITT. The collected patterns were then stitched together to produce an XRD pattern ranging from 6 – 24 degrees.

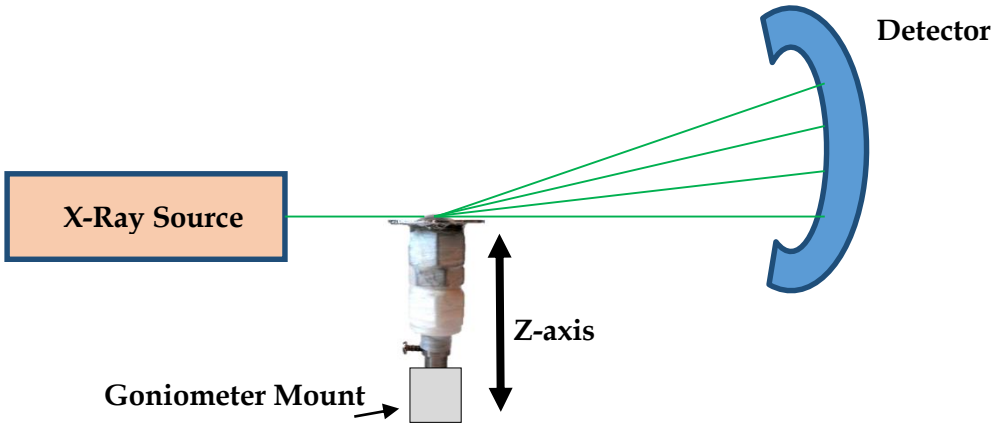

Figure 2.9 - Simple diagram of how the *in-situ* cell was mounted for XRD data collection.

The *in-situ* cell was aligned on the beam so that the X-rays were fired into the centre of the aluminium foil X-ray window. The cell height was then adjusted accordingly until the intensity of the beam was at the half way point from its overall intensity.

2.8.4 X-ray Absorption Near Edge Structure (XANES)

2.8.4.1 XANES Transmission Measurements

Beamline B18 (Diamond Light Source, U.K.) has an energy range of 2 – 35 keV, with the X-rays supplied by a bending magnet source from the synchrotron. XAS (X-ray absorption spectroscopy) measurements at the Co edge were carried out using a Si(311) crystal monochromator, with a Pt coated mirror used to reject higher harmonics.

Transmission mode XAS uses three X-ray detectors that are positioned sequentially in the beamline, as shown by **Figure 2.10**. A transmission XAS experiment measures the difference in X-ray absorption between the two detectors as the energy is changed. The X-ray adsorption edge of the sample is determined by measuring the X-rays transmitted before and after the sample by **Equation 2.21.**

$$\mu x = ln \frac{I_o}{I_t} \qquad \textbf{Equation 2.21}$$

μx = X-ray absorption edge (eV), I_o = X-rays transmitted before striking sample (nm)
I_t = X-rays transmitted after striking sample (nm)

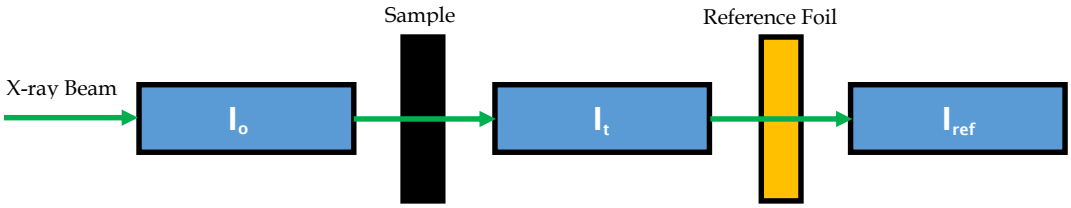

Figure 2.10 - Schematic of the X-ray detector setup for transmission XAS experiments.

The X-ray detectors are ionisation chambers that consist of a pair of electrodes that are held at a constant potential surrounded by an inert gas. The X-rays pass through the chamber and are absorbed by the inert gas forming electron/positive ion pairs. The electrons migrate to the anode and the positive ions migrate to the cathode, with the resulting current being directionally proportional to the number of X-ray photons entering the chamber.

The sample being collected must be as homogeneous as possible, as any small holes in the sample causes X-ray leakage that would result in more noise within the data. The transmission samples in this work were prepared as pellets mixed with $LiCoPO_4$, carbon and PTFE binder in the same composition as the tested pellets inside Swagelok cells. For the *ex-situ* studies, the pellets were charged within a standard Swagelok cell to a specific potential at 0.2 C before being placed in a sealed plastic coated aluminium pouch under an argon atmosphere.

2.8.5 X-Ray Photoelectron Spectroscopy

X-ray Photoelectron Spectroscopy is based on the photoelectric effect that was discovered by Hertz in 1887. It is a widely used surface analytical technique whereby the interaction of an X-ray photon of sufficient energy with a solid results in the emission of an electron from its surface. This process is described by the Einstein equation.[9]

$$E_{kin} = h\nu - E_B - \psi \qquad \textbf{Equation 2.22}$$

E_{kin} = kinetic energy of emitted electron (eV), $h\nu$ = X-ray photo energy (eK) E_B – ionisation energy related to the Fermi level (eK) and ψ = work function of the instrument (eK)

When a surface is irradiated by X-rays, the core level electrons of surface atoms absorb the X-ray photon energy hν, overcoming their binding energy E_B and are emitted out of the surface with a certain kinetic energy E_{kin}.

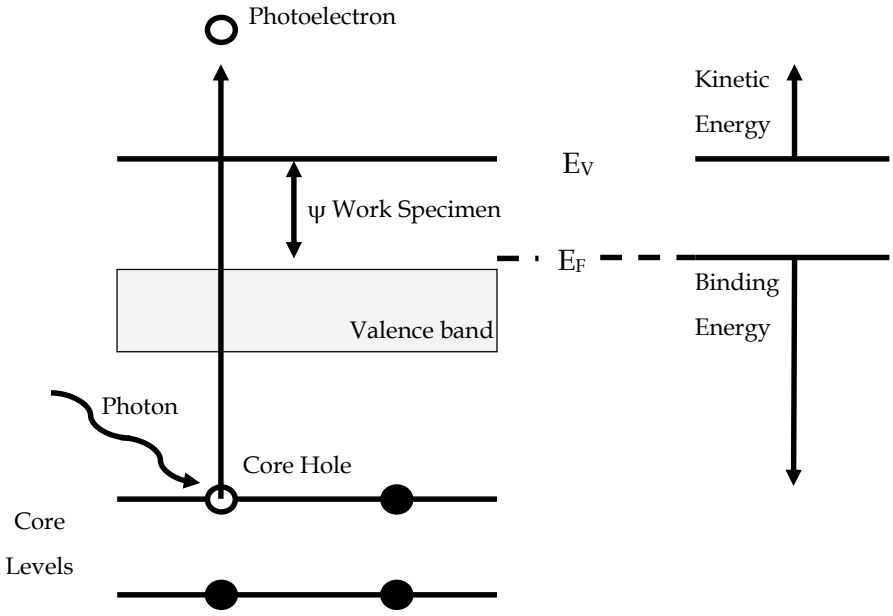

Figure 2.11 – Diagram of the photoemission process.

The surface sensitivity depends on the depth of origin of the detected species. In XPS the X-ray photons that bombard the surface penetrate deep into the solid, the resultant emitted electrons that can be detected without loss of energy are very close to the surface. Electrons generated deeper in the solid may escape, but on the way out they will have collided with other atoms and lost energy and are therefore not useful.[10] Therefore the photoelectrons that are detected for use originate only from the uppermost layers of a solid.

2.8.6 Scanning Electron Microscopy

SEM is a type of electron microscope that produces an image through scanning a sample with a beam of electrons.[11] Initially, an electron beam is created by heating a tungsten filament, which then focuses the resulting electrons into a beam using electromagnets. These electrons are then directed at the sample which is under vacuum and is scanned in a raster fashion (sweeping from left to right only). The detector can detect the presence of secondary electrons, which result from primary electrons in the beam ionising atoms in the sample which then emit secondary

electrons. The energies of secondary electrons are very low, which means that only the secondary electrons generated a few nanometres from the surface actually reach the detector and form part of the image. This would allow for the image to be made exclusively of the surface and give details of the size and topography of the particles in the sample. The atomic number of the sample affects the interaction volume of the sample with the beam of electrons.

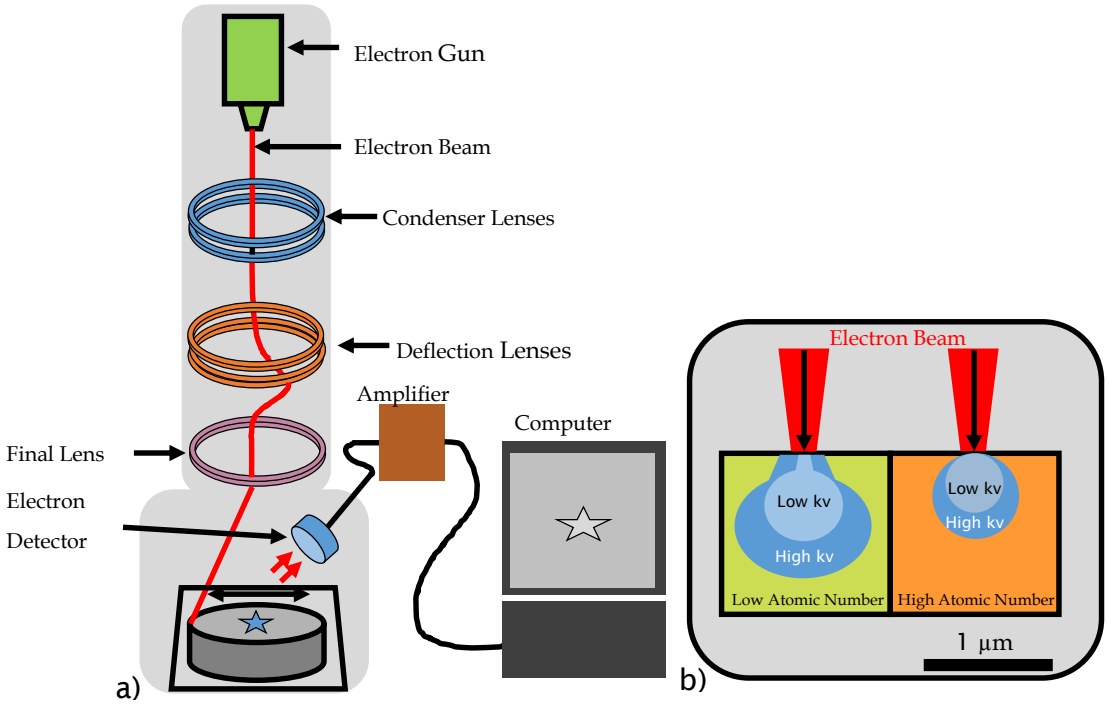

Figure 2.12 – a) Illustration of how SEM produces an image from a sample b) kV dependant interaction volume of electron beam.

Because of the nature of the technique, samples to be analysed by SEM must be conducting. Non-conducting samples allow electrons to build up on the surface of the sample, and interact with the electron beam itself which would produce a blurred image. This problem can be overcome by sputtering a thin layer of conductive material (gold) onto the surface of non-conducting samples. The structure and composition of the sample can have a large influence on the number of electrons produced. Edges and variation in the incident beam angle can allow for additional secondary electrons to be produced, the effect creates contrast in the images produced.

Images can be produced utilising the emission of backscattered electrons from the sample. These electrons are produced when a high energy electron interacts elastically with the nuclei of an atom within the sample. The probability of the production of

back scattered electrons increases as the atomic number of the nuclei increases. This variation in production allows for composition images to be produced in which atomic numbers that are higher than others within the sample appear brighter.

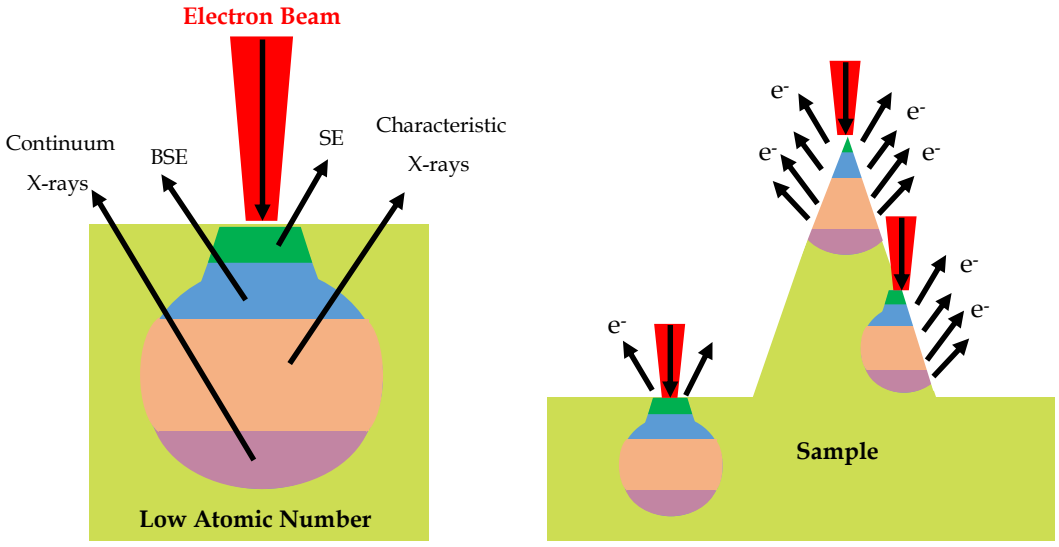

Figure 2.13 – a) interaction of a high energy electron beam with a sample b) influence of sample structure on the number and type of emitted electrons and X-ray photons.[12]

X-rays are produced *via* two main processes which occur when a sample is exposed to a beam of high energy electrons. **Figure 2.14** displays the two different methods. The Bremsstrahlung X-ray production occurs when high energy electrons experience deceleration or directional change caused by interaction with the nucleus of atoms within the sample as shown in a). Characteristic X-ray production occurs when high energy electrons eject an inner shell electron from the atom. The hole that is left from the ejected electron is filled by an electron from an outer shell to stabilise the system. The relaxation of the electron results in the emittance of an X-ray photon of energy equal to the difference in energy shells. These energies are specific and allow for identification of the material within the sample.

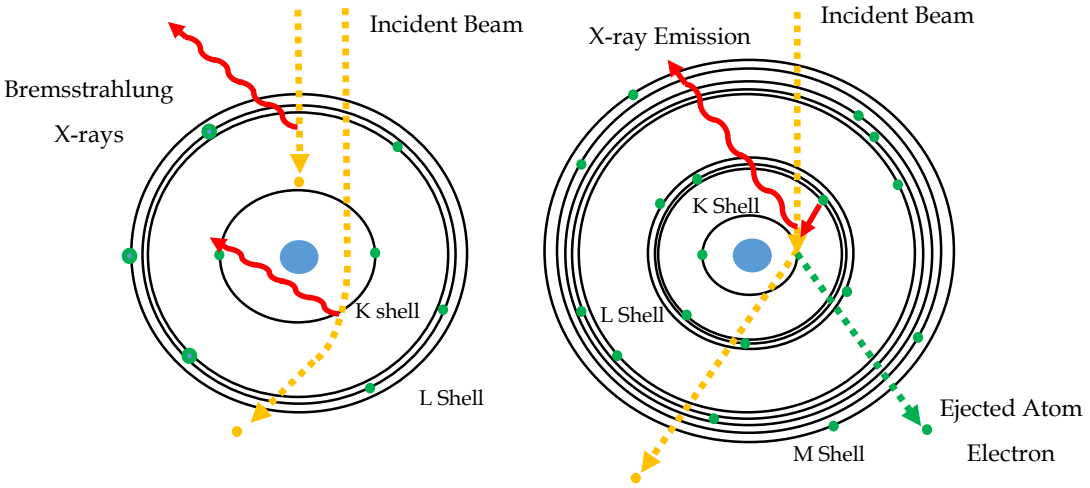

Figure 2.14 – X-ray photon generation mechanisms
a) Bramsstrahlung X-ray generation (continuum X-rays), b) Characteristic X-ray generation.

2.8.6.1 Method

A JEOL 6500F instrument with an attached EDS detector (Oxford Instruments Inca 300) and JEOL backscatter detector was used to collect images and characterise samples. The sample stage was rotated and tilted during imaging and the probe current and accelerating voltage was altered to obtain a clear image.

2.8.7 Differential Electrochemical Mass Spectrometry (DEMS)

Differential Electrochemical Mass Spectrometry (DEMS) is an analytical technique that combines electrochemical cell experimentation with mass spectrometry. Mass resolved observation of gaseous or volatile products can be detected *in-situ* by correlating the faradaic electrode current with the relevant mass ion currents.[13] The process can be broken down into three key stages: ionisation, mass filtration and detection.

Ionisation

Gas molecules are ionised by electron impact ionisation. The filaments inside the ion source create an electron beam through thermionic emission. These electrons then collide with gas particles which results in the removal of one or more electrons generating positive ions. These positive ions are then extracted from the source cage by a focus plate that is held at 90 V. Any electrons are repelled by the focus plate preventing them from entering the detector.

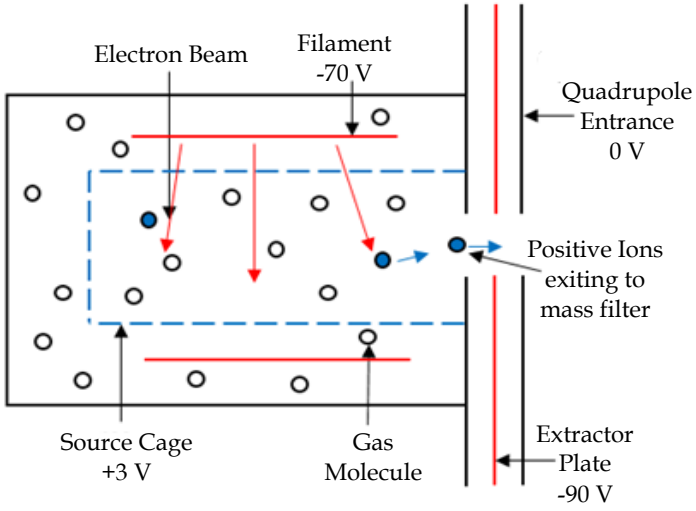

Figure 2.15 - Schematic describing electron impact ionisation.

Mass filtration

The mass filter differentiates the ions produced selecting a specific mass/ charge ratio for detection. A quadrupole detector is used in these experiments which consists of two pairs of parallel equidistant metal rods at equal but opposite potentials. These potentials contain fixed direct current and alternating radio frequency components. Any ions entering the field experience potential differences deflecting them from their original trajectory. The extent of the deflection is dependent on its *m/z* ratio. At each interval only one mass/ charge ratio resonates with the electric field passing unchanged through to the detector.

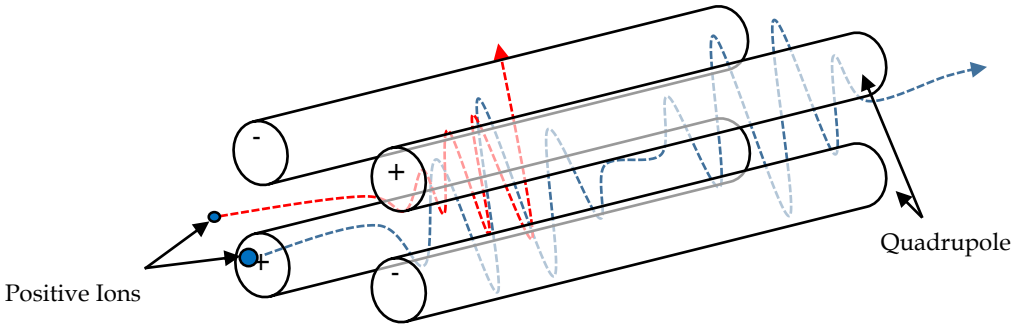

Figure 2.16 - Schematic describing quadrupole filtration.

Detection

The filtered ions then strike the detector assembly and the ion current produced is measured by a sensitive amplifier. There are two main types of detector (the faraday cup and the secondary electron multiplier). The Faraday cup is a passive conducting surface which when struck by fast moving ions causes a shower of secondary electrons. The cup shape allows for all these electrons to be collected. While only one electron is required to neutralise the ion the emission of several electrons provides amplification for the instrument. The Secondary electron multiplier uses a surface designed to generate secondary electrons. Once the ion hits the surface two or three electrons are generated each going on to emit more electrons in a cascade effect leading to greater amplification.

2.8.7.1 Method

The carrier gas (argon) was purged through 1/8″ stainless steel (Swagelok) to a mass flow controller (Bronkhorst). The mass spectrometer (Hiden Analytical) was attached via a capillary line to the sample and a small volume (1ml min^{-1}) of the outlet gas continuously flowed. Any volatile products generated by the cell would be carried in the stream and detected by the spectrometer.

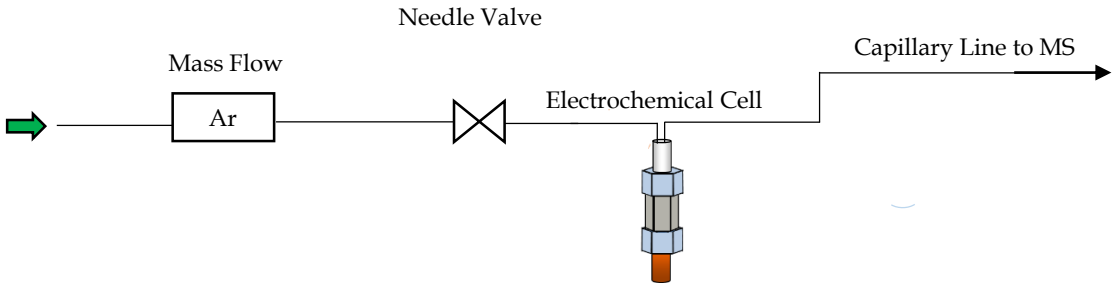

Figure 2.17 - Schematic describing the mass spectrometry arrangement.

2.9 References

1 B. M and N. G, Electrical Safety: Systems, Sustainability and Stewardship, Taylor & Franic Group, LLC, 2015.

2 W. Weppner and R. A. Huggins, J. Electrochem. Soc., 1977, **124**, 1569–1578.

3 A. L. Patterson, Phys. Rev., 1939, **56**, 978–982.

4 J. I. Langford and A. J. C. Wilson, J. Appl. Crystallogr., 1978, **11**, 102–113.

5 H. M. Rietveld, Acta Crystallogr., 1967, **22**, 151–152.

6 H. M. Rietveld, J. Appl. Crystallogr., 1969, **2**, 65–71.

7 G. Bunker, Introduction to XAFS; A Practical Guide to X-ray Absorption Fine Structure Spectroscopy, Cambridge University Press, 2010.

8 A. V. Chadwick, A. Berko, E. J. Schofield, A. M. Jones, J. F. W. Mosselmans and A. D. Smith, Int. J. Archit. Herit., 2012, **6**, 228–258.

9 J. M. Hollander and W. L. Jolly, Acc. Chem. Res., 1970, **3**, 193–200.

10 J. C. Vickerman, in Surface Analysis– The Principal Techniques, John Wiley & Sons, Ltd, Chichester, UK, 1–8.

11 I. M. Watt, The principles and practice of electron microscopy, Cambridge University Press, Cambridge, 1997.

12 W. D and B. C. C, Transmission electron microscopy: A textbook for materials science, Springer Science+Business Media New York, New York, 1996.

13 S. J. Ashton, Differential Electrochemical Mass Spectrometry, 2012, 9–27.

Chapter 3:

Initial High Voltage Cathode Material Insight

3.1 Introduction

This chapter contains the initial work in synthesising and testing different high voltage cathode materials in an attempt to target an appropriate material to investigate further. All of the work within this chapter (unless stated otherwise) was done using 1 M $LiPF_6$ EC:EMC (1:3 v/v) which was made up within the lab with glovebox water and oxygen levels < 10 ppm. EMC was distilled so that the water content within the solution was minimal. Karl Fisher Coulometry indicated < 10 ppm of water present within the EMC. The $LiPF_6$ salt was combined with the organic solvents inside the glovebox and stored in plastic bottles.

3.2 $LiCu_{0.5}Mn_{1.5}O_4$ Cathode Material

3.2.1 Introduction

$LiCu_{0.5}Mn_{1.5}O_4$ is part of the $LiCu_xMn_{2-x}O_4$ series which has a cubic spinel structure with a unit cell parameter similar and slightly smaller than that of $LiMn_2O_4$.[1] Observation of reversible lithium ion intercalation within $LiMn_2O_4$ was first observed by Goodenough in 1984[2] and has been extensively studied worldwide. The material presents several advantages as a cathode material due to its low cost and negligible toxicity in comparison to $LiCoO_2$. $LiMn_2O_4$ is subject to Mn loss and structural degradation on cycling, but partial substitution of a transition metal is recognised as an approach for improving the cathodic stability of the spinel lattice.[3]

Ein-Eli *et. al* reported for the first time $LiCu_{0.5}Mn_{1.5}O_4$ as a high voltage cathode material in 1997, and reported a discharge capacity of 71 mA h g^{-1}, noticing that a portion of the lithium can be removed from the material at 4.8 to 5 V *vs*. Li/Li^+. The structure is similar to $LiMn_2O_4$ (space group *Fd3m*) but with the inclusion of copper which enhances the electrochemical stability, allowing up to 4.9 V for a $Cu^{2+/3+}$ metal redox centre during lithium intercalation. $LiCu_{0.5}Mn_{1.5}O_4$ is a single phase spinel product, with a theoretical capacity of 144 mA h g^{-1} (assuming all the lithium is extracted).

3.2.2 $LiCu_{0.5}Mn_{1.5}O_4$ Synthesis

$LiCu_{0.5}Mn_{1.5}O_4$ was synthesised via a sol gel process by using stoichiometric amounts of CH_3COOLi (Sigma Aldrich), $Cu(OOCH_3)_2$ (Sigma Aldrich) and $Mn(OOHCH_3)_2$ (Sigma Aldrich) were dissolved in a mixture of ethanol:water (1:1 v/v) to form an homogenous solution. The solution was stirred at 80 ^oC for 4 hours before the addition of NH_4OH (28 % w/w, Sigma Aldrich) until a gel was formed. This was heated to dryness under vacuum at 100 ^oC using a liquid nitrogen trap. The powdered precursors were ground and heated for 12 hours in air at 500 ^oC, subsequently refired at 650 ^oC for 12 hours, and finally calcined at 750 ^oC for another 12 hours.[4] The heating/cooling steps was set at 5 ^oC per minute.

Figure 3.1 displays an image of the collected powder pattern fitted against published data from the ICSD database.[5] The diffraction pattern shown indicates that a single phased crystalline structure was synthesised within the sample.

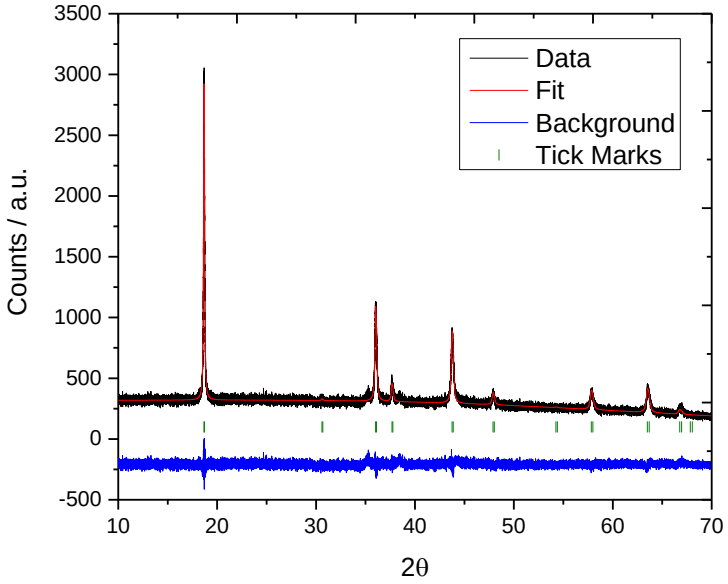

Figure 3.1 X-ray diffractiogram of $LiCu_{0.5}Mn_{1.5}O_4$, refined against data from the ICSD database.[5] Lattice constants a = b = c = 8.2991(4) Å, α = β = γ = 90°, wRp = 6.38 % Rp = 5.06 %.

Scanning electron microscope (SEM) imaging was conducted to observe the morphology of the material. **Figure 3.2** captures the image taken; the particles adopted circular agglomerates of uniform size with large bulk sized particles of 1-2 µm.

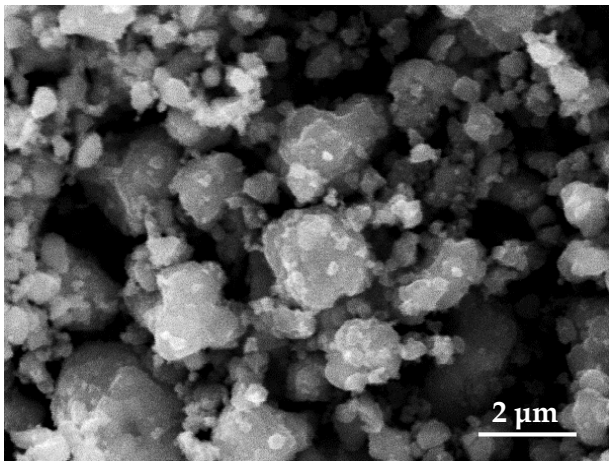

Figure 3.2 - SEM image of $LiCu_{0.5}Mn_{1.5}O_4$ containing 1–2 µm bulk sized particles.

3.2.3 $LiCu_{0.5}Mn_{1.5}O_4$ Electrochemical Tests

$LiCu_{0.5}Mn_{1.5}O_4$ powder was made into composite electrodes by preparing the samples using PTFE binder. The pellets were made up as described in **Chapter 2** as 75: 20: 5 (active material: carbon: PTFE) and incorporated into a two electrode Swagelok cell. Galvanostatic cycling (constant current) was applied to the cell at a rate of 0.1 C using 1 M $LiPF_6$ EC:EMC (1:3) as the electrolyte. The cycling data is displayed in **Figure 3.3**.

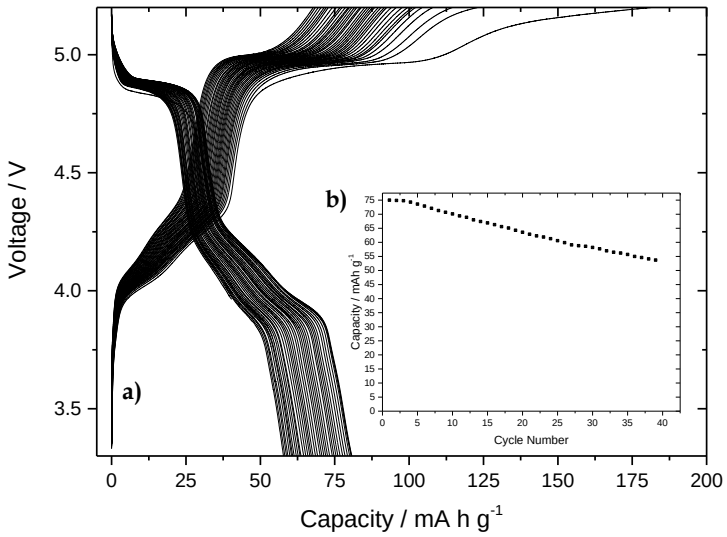

Figure 3.3 a) Galvanostatic cycling of $LiCu_{0.5}Mn_{1.5}O_4$ at 0.1 C with potential limits 5.2 – 3.3 V using 1 M $LiPF_6$ EC:EMC (1:3). b) Capacity *vs.* cycle number.

There are two distinct and well refined regions during cycling where there is a one-electron reaction occurring at each metal centre. During charge between ~4.0 - 4.4 V the manganese metal centre is undergoing oxidation from $Mn^{+3} \rightarrow Mn^{+4}$. As the voltage increases, the copper oxidation of $Cu^{2+} \rightarrow Cu^{3+}$ occurs at 4.95 V. It should be noted here that these oxidation states on the metal centres does not balance the structure during extraction and insertion of lithium. There are very few research papers published on $LiCu_{0.5}Mn_{1.5}O_4$, but Meng *et al.* observed that when more than one half of lithium ions are extracted, the charge densities of the oxygen atoms changed significantly, which may suggest the extra electrons could be provided by oxygen ions.[6] During the first cycle, there is a large amount of irreversible capacity loss particular after 5 V. This extra irreversible capacity can be possibly associated with the formation of SEI. The gradient of these charge cycles above 5 V becomes higher during subsequent cycling, which can be interpreted as a measure of the efficiency of the SEI formation.

An initial discharge capacity of 75 mA h g^{-1} matched well with reported data[4], reporting a discharge capacity of 71 mA h g^{-1}. The cyclability of the material matched with that of the literature, with 71.6 % of the discharge capacity maintained after 40 cycles.

Figure 3.4 displays a cyclic voltammogram (CV) cycled within the same potential limits as **Figure 3.3** with a scan rate of 0.05 mV s^{-1}. The CV shows three distinguishable regions which are related to the metal redox couples occurring with manganese and copper respectively. Between 4.0 – 4.4 V, there are two distinct peaks shown within the manganese redox couple expected potential range. This is characteristic of a $LiMn_2O_4$ cyclic voltammogram, in which lithium extraction and insertion occurs in two stages. The first peak is attributed to the removal of lithium ions from half of the tetrahedral sites in which Li-Li interactions occur. The latter peak is caused by the removal of lithium ions from other tetrahedral sites in which lithium ions do not have Li-Li interactions.[7] The areas of the peaks are essentially equal indicating that in each stage lithium ions occupy half of the total available crystallographic sites. The peak at ~4.95 V corresponds to the $Cu^{2+/3+}$ redox couple.[8]

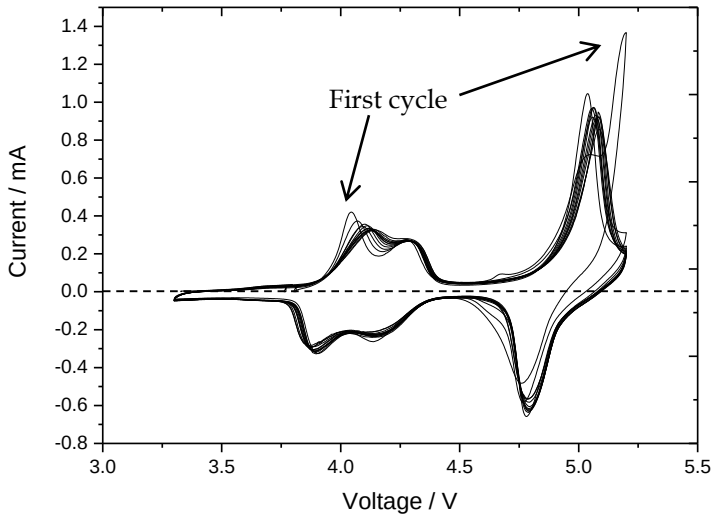

Figure 3.4 – Cyclic voltammograms obtained from $LiCu_{0.5}Mn_{1.5}O_4$ cycled in 1 M $LiPF_6$ EC:EMC (1:3) within the potential limits of 5.2 – 3.3 V. Scan rate of 0.05 mV s^{-1}.

During the first cycle, there is a second peak observed at ~5.2 V. This peak can be associated with the initial electrolyte breakdown to form an SEI layer on the particles, which protects the electrolyte from further degradation on the surface of the electrode.

3.3 $LiNi_{0.5}Mn_{1.5}O_4$ Cathode Material

3.3.1 Introduction

Following on from the $LiCu_{0.5}Mn_{1.5}O_4$ work, the industry sponsor supplied the cathode material $LiNi_{0.5}Mn_{1.5}O_4$. Over the years, the material has attracted attention because of its high intercalation potential of 4.7 V *vs.* Li/Li^+ and a theoretical capacity of 147 mAh g^{-1}. There are two kinds of crystal structure for spinel $LiNi_{0.5}Mn_{1.5}O_4$; face-centred spinel (*Fd3m*) and primitive simple cubic crystal ($P4_132$). With the face centred structure, the metal ions are randomly distributed in the 16d sites whereas for the primitive structure it is more orderly with the manganese ions distributed in 12d sites and the nickel ions in 4a sites.[9] Early work on $LiNi_{0.5}Mn_2O_4$ by J. Dahn *et. al* in 1997 demonstrated that a single phase spinel structure was produced during synthesis with a discharge capacity in excess of 100 mAh g^{-1} over a range of tens of cycles.[10]

Previous results obtained from $LiNi_xMn_{2-x}O_4$ suggested that the high voltage output within the systems originated from the oxidation of nickel.[10] Yang *et al.* proposed that a significant amount of Mn^{4+} ion in the spinel framework was essential for electrochemical activity at around 5 V *vs.* Li/Li^+.[11] The view was supported by Kawai who presented work on the manganese free spinel oxide $Li_2NiGe_3O_8$, which did not show any capacity above 4.5 V *vs.* Li/Li^+, indicating that the presence of manganese was a necessity.[12] The influence on metal doping in the $LiNi_{0.5}Mn_{1.5}O_4$ has been widely studied, with the nickel doped spinel displaying a high capacity and cyclability.[13,14,15] The redox behaviour occurs between 4.6 – 4.7 V *vs.* Li/Li^+, which can be assigned to the $Ni^{2+/4+}$ two electron process. Within the 4 V *vs.* Li/Li^+ region there can sometimes be minor redox behaviour relating to the $Mn^{3+/4+}$ couple, but generally the manganese redox is considered to be fairly inactive.[16]

3.3.2 $LiNi_{0.5}Mn_{1.5}O_4$ Electrochemical Tests

$LiNi_{0.5}Mn_{1.5}O_4$ was prepared as an electrode via an ink process using PVDF as the binder as described in **Chapter 2**. The technique involved making an electrode slurry by mixing the pre-dissolved PVDF in NMP (10 % by weight) into carbon to form a paste, and then the active material was added. No homogeniser was used to make up this first slurry. The slurry was then applied to aluminium foil and dried, forming the composite electrode. The ratio of the composite electrode was 76: 12: 12 (active material: carbon: PVDF).

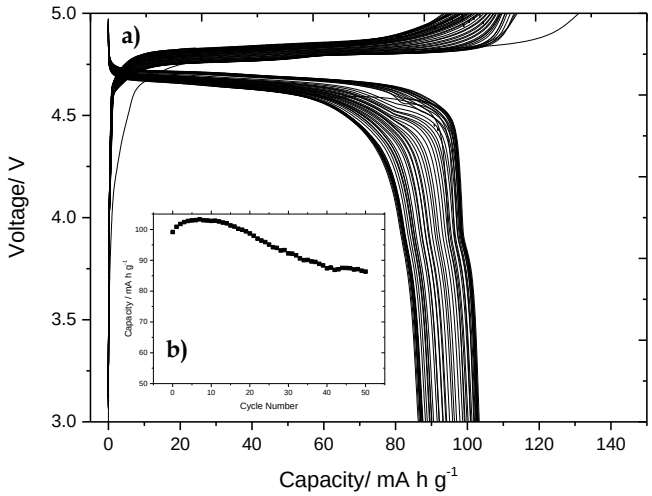

Figure 3.5 - a) Galvanostatic cycling of $LiNi_{0.5}Mn_{1.5}O_4$ with potential limits 5.0 – 3.0 V using 1 M $LiPF_6$ EC:EMC (1:3) at 0.5 C. b) Cycling data shown over 50 cycles.

Figure 3.5 shows that the capacity produced from the material was less than expected, with the industry sponsor achieving a discharge capacity of 138 mA h g^{-1} at the same C-rate. It was suspected that the reason for the lower performance was in the levels of mixing the slurry. Therefore an IKA T25 homogeniser was used in the next batch, which has a much higher mixing capability due to its small high shear blades in comparison to magnetic stirring.

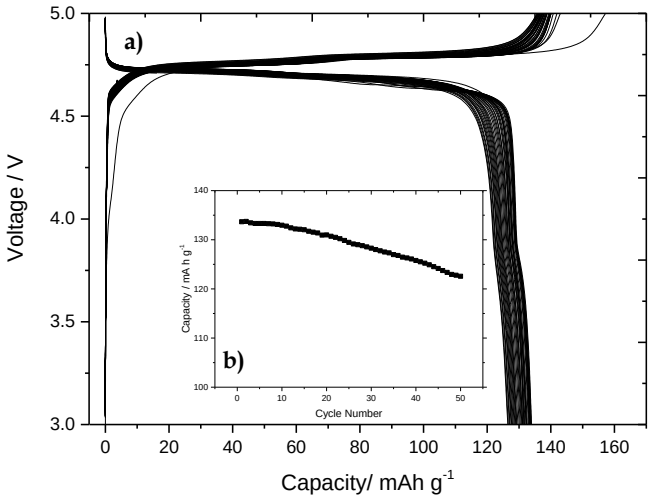

Figure 3.6 – a) Galvanostatic cycling of $LiNi_{0.5}Mn_{1.5}O_4$ with potential limits 5.0 – 3.0 V using 1 M $LiPF_6$ EC:EMC (1:3) at 0.5 C. Electrode slurry was mixed with a homogeniser. b) Cycling data over 50 cycles

Figure 3.6 show the results obtained from using the homogeniser. The capacity values were as expected, with the cycle life competitive with standards for the material. It can be assumed that a high level of mixing is essential when using PVDF slurries; good contact between the carbon and the active material is a necessity for a good bulk conductivity of the composite electrode which is linked to the cell performance.

3.4 $LiNiPO_4$ Cathode Material

3.4.1 Introduction

Substantial attention has been paid to the use of lithium transition metal phosphates with an ordered olivine structure $LiMPO_4$ (M = Fe, Mn, Co and Ni) as a cathode material. The redox potentials increase as the metals move through the 3rd row of the transition metal series in the periodic table, with the potentials of the $M^{3+/2+}$ redox potentials being predicted at 3.5, 4.1, 4.8 and 5.2 V *vs.* Li/Li^+ respectively (Fe, Mn, Co and Ni).[17,18] Research results have demonstrated that the theoretical predictions of the redox potentials are consonant with the experimental values (except for Ni). $LiNiPO_4$, has the highest redox potential, however it is least studied because it is not electrochemically active; Okada *et al.* reported that $LiNiPO_4$ had no voltage platform in the discharge profiles and no reduction peaks detected in the cyclic voltammogram at a scan rate of 0.2 mV s^{-1}.[19]

Many research groups have had difficulties in obtaining a pure phase of $LiNiPO_4$, with $Li_2Ni_3(P_2O_7)_2$, NiO and Ni_3P as common impurities.[18,21] Computer simulations have shown a favourable defect in $LiNiPO_4$ (cation antisite defect) in which there is an Li-Ni site exchange. The concentration of cation site exchange would be temperature dependent so it would be sensitive to different experimental conditions.[22] Li^+ mobility is limited to 1D channels, so any immobile lithium would effectively block lithium channels and reduce possible pathways of lithium intercalation.[23,24]

$LiNiPO_4$ exhibits very poor electrochemical activity mainly due to its low electronic conductivity and high redox operating potential. As of yet, no stable $NiPO_4$ phase is known which might be a reason for the poor reversibility of the cathode, due to the possibility of a collapse in the crystal lattice.[25] Wolfenstine and Allen were one of the first to report successful electrochemical activity of $LiNiPO_4$.[20]

3.4.2 $LiNiPO_4$ Synthesis

$LiNiPO_4$ was synthesised via a sol gel process by using stoichiometric amounts of Li_2CO_3 (Sigma Aldrich), NiO (Sigma Aldrich) and $(NH_4)_2HPO_4$ (Sigma Aldrich) which was ground in ethanol. The black paste was then transferred to an oven at 80 °C for 1 hour. The dried powder was then heated at 400 °C for 12 hours under air, before being reground and heated at 800 °C under air with heating/cooling steps at 5 °C per minute.

Figure 3.7 displays an image of the collected powder pattern fitted against published data from the ICSD database.[26] The diffraction pattern shown indicates that the $LiNiPO_4$ phase was present, but there was also a large impurity of NiO. To remove the impurity, a slower cooling down temperature was controlled at 0.5 °C a minute. The second XRD pattern within **Figure 3.7** shows that the NiO impurity was removed and that the single phased $LiNiPO_4$ was present as a majority.

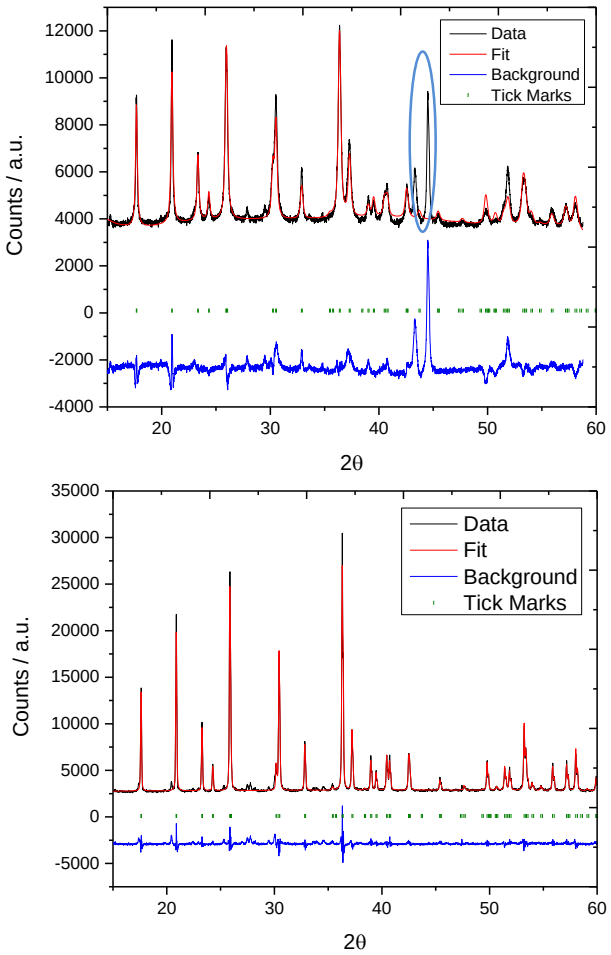

Figure 3.7 – X-ray diffractiogram of $LiNiPO_4$ with fitted data obtained from the ICSD database.[26] The large NiO impurity peak was removed by slowing down the cooling conditions during heat treatment. Lattice constants a = 10.03849(6) b = 5.85989(3) c = 4.68083(8), α = β = λ = 90° wRp = 4.45 % Rp = 3.15 %.

The high temperature is required for the sintering process, but the disadvantage of heating to such a high temperature is the loss of oxygen. A slow cooling rate is required to anneal the sample with respect to oxygen exchange, allowing for oxygen to be brought back into the structure.

Figure 3.8 displays the results obtained from two different cyclic voltammograms using two different electrolytes. The large oxidation peak suggests that lithium extraction could be occurring; however the lack of reduction peak suggests that the lithium cannot be re-inserted back into the materials structure. This evidence can be backed up by the second cycle on both CV's showing no oxidation peak.

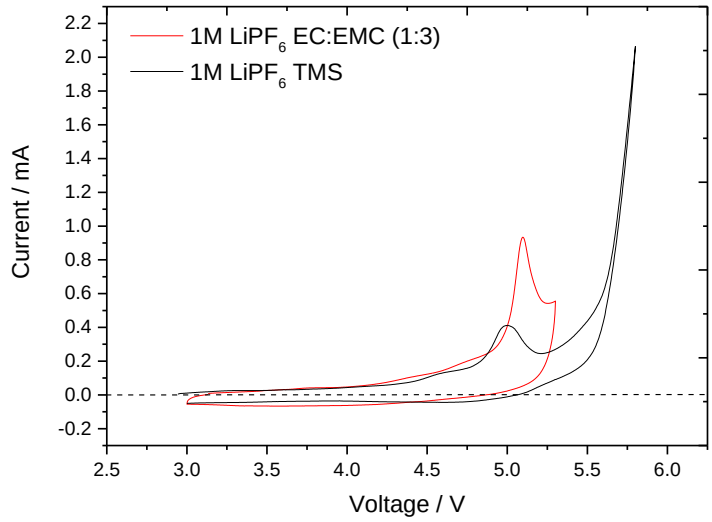

Figure 3.8 - Cyclic Voltammogram of $LiNiPO_4$ *vs.* Li/Li^+ on initial cycle using two different electrolytes at different voltage limits between 5.6 – 3.0 V (EC:EMC 1:3) and 5.8 – 3.0 V (TMS). Scan rate of 0.200 mV s^{-1}.

Figure 3.9 is a galvanostatic plot of $LiNiPO_4$. On the first cycle, there appears to be a large amount of oxidation of a species (potentially carbon) and very little lithium intercalation activity, achieving a discharge capacity of ~25 mA h g^{-1} at 0.1 C. From this result, it was decided to pursue a more readily active cathode material.

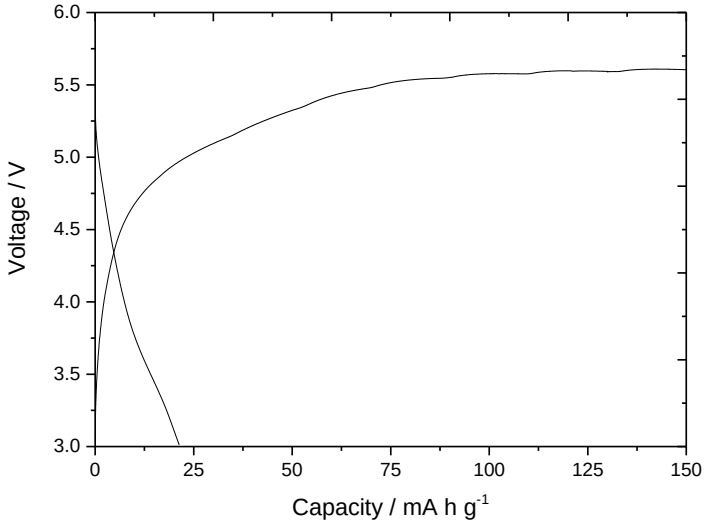

Figure 3.9 - The initial galvanostatic cycle of $LiNiPO_4$ from 5.8 – 3.0 V at 0.1 C using 1 M $LiPF_6$ in EC:EMC (1:3)

3.5 $LiCoPO_4$ – Material Selected for Further Investigation

Extensive work has been carried out on electrode materials with polyanion frameworks built of $(PO_4)^{3-}$ tetrahedral and MO_6 octahedral units as possible replacements of $LiMO_2$ (M = Co, Ni, Mn) oxide-based materials. The oxide-based materials have safety concerns in terms of releasing oxygen (uncontrolled release could lead to thermal runaway) at relatively high voltages. In phosphor-olivines, all of the oxygen ions form strong covalent bonds with the phosphorus which allows for stable operations at high temperatures and extreme safety under abusive conditions.[27]

Both $LiCoPO_4$ and $LiNiPO_4$ have difficulties readily inserting and extracting lithium within the voltage stability window of existing non-aqueous electrolytes. While efforts to improve the electrolyte stability at high voltages (> 4.8 V *vs.* Li/Li^+) have made it possible to explore the $LiCoPO_4$ compounds, the electrochemical performance of $LiNiPO_4$ is very limited due to the high voltage redox potential at ~5.3 V *vs.* Li/Li^+ (Ni^{3+}/Ni^{2+}) and the difficulty in obtaining a pure single phase of $LiNiPO_4$.[28]

3.5.1 Introduction and Reasoning

The low energy density of $LiFePO_4$ induced strong interest towards other materials of the $LiMPO_4$ series. $LiCoPO_4$ has a high theoretical energy density, up to 800 W h kg^{-1} due to its inherently high $Co^{3+/2+}$ redox potential of 4.8 V *vs.* Li/Li^+.[29] At the early stages of $LiCoPO_4$ the discharge capacity at 4.8 V was observed at 70 mA h g^{-1} which is far below its theoretical capacity of 167 mA h g^{-1}.[30]

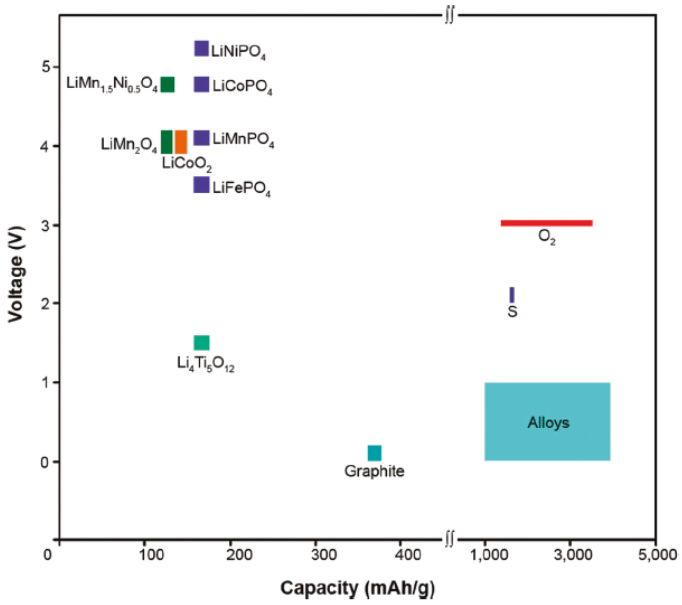

Figure 3.10 - A variety of different materials demonstrating qualitatively their potential voltage and capacity properties. Reproduced from reference[31] with permission.

The poor conductivity is one of the challenging problems which prevent $LiCoPO_4$ from being an excellent candidate for 5 V lithium ion batteries, and several different approaches have been attempted to combat this problem. Yang *et al.* reported that it is difficult to carbon coat the particle surface using a sol-gel method.[32] Wolfenstine *et al.* did demonstrate an enhancement of the electronic conductivity by carbon coating the $LiCoPO_4$ particles, but there was severe capacity fade.[33] The severe capacity fade can be due to the electrolyte being consumed at high voltages which is the main problem within high voltage lithium-ion systems.

3.5.2 Initial Synthesis

Initially, $LiCoPO_4$ was synthesised via a sol-gel method. Stoichiometric amounts of CH_3COOLi, $NH_4NH_2PO_4$ and $Co(NO_3)_2.6H_2O$ were dissolved in a minimum amount of distilled water and added into a round bottom flask. Citric acid was added to the solution under stirring (molar ratio citric acid: cobalt = 1:2). The round bottom flask was then sealed (air tight) and left to stir at room temperature for 20 hours. The clear solution was dried at 80 °C on a hotplate to obtain a xerogel. This was then ground and preheated at 300 °C for 5 hours under argon. The powder was reground and heated at 650 °C for 10 hours under flowing argon to obtain a purple powder. To carbon coat the material, $LiCoPO_4$ was ground with sucrose and heated to 650 °C under flowing argon. The high temperature heating/cooling steps were set as 5 °C per minute

Figure 3.11 displays the results from the XRD pattern. The pattern obtained was consistent with published data[34] and the corresponding lattice parameters seemed reasonable with no obvious impurities within the sample.

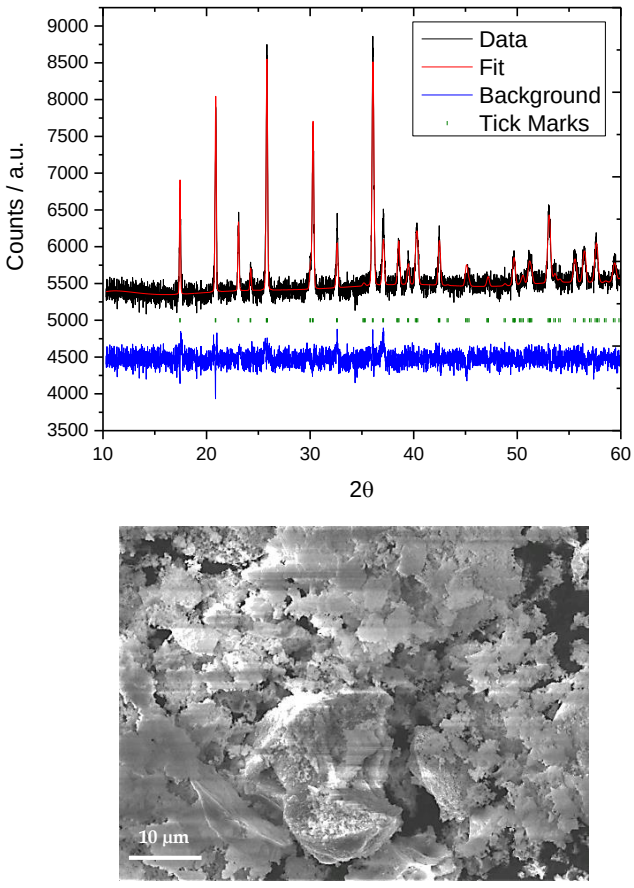

Figure 3.11 X-ray diffractiogram and SEM image of $LiCoPO_4$, refined against data from the ICSD database.[34] Lattice Constants: a = 10.2014(6) b = 5.9233(9) c = 4.7005(3), α = β = γ = 90°, R_{wp} = 1.39 %.

3.5.3 Electrochemical Tests

Uncoated $LiCoPO_4$ powder was prepared as composite electrodes using PFTE, carbon and the active material (5: 20: 75). The CV (**Figure 3.12**) shows that the material is reversible with an oxidation peak and reduction peak of the Co metal centre at 4.9 and 4.7 V respectively. It can be noted that there are two peaks present during oxidation or reduction; this is because the lithium intercalation process takes place over a two two-phase process.

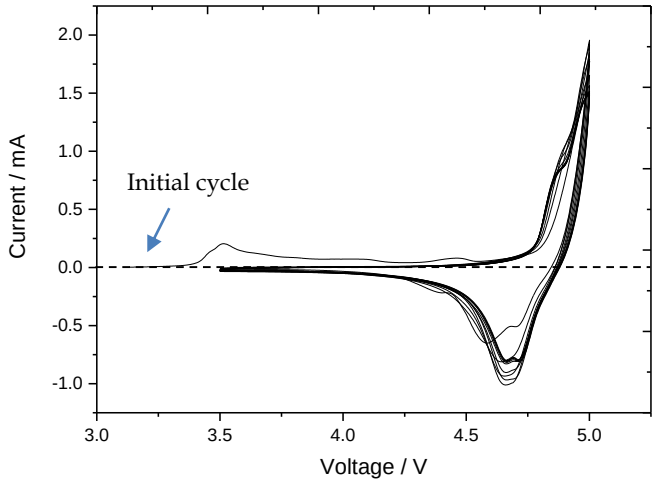

Figure 3.12 - Cyclic Voltammorgram of $LiCoPO_4$ *vs.* Li between 5.0 – 3.5 V with PTFE binder using 1 M $LiPF_6$ in EC:EMC (1:3) at 0.100 mV s^{-1}.

Galvanostatic cycling (**Figure 3.13**) was applied at 0.1 C and from these results, it can be observed that the cycle life decayed rapidly, suggesting that there is an unknown instability/ breakdown of activity within the cathode or potentially insufficient mixing of the cathode components.

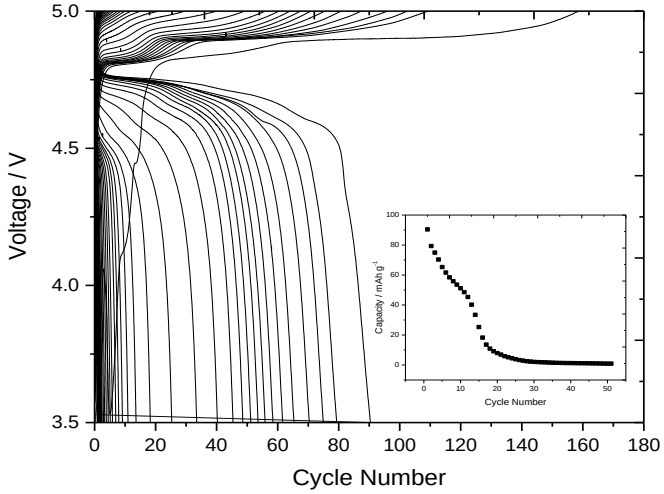

Figure 3.13 - Galvanostatic cycling of $LiCoPO_4$ *vs.* Li/Li^+ between 5.0 – 3.5 V with PTFE at 0.1 C with 1 M $LiPF_6$ in EC:EMC (1:3)

$LiCoPO_4$ was successfully synthesised using the solid-state synthesis method. When using this method, there is no control over the particle size or shape, as the solvent is evaporated off before the first heat treatment. The SEM image very large inconsistent particles are formed which can agglomerate together. This low level of particle control could be due to the low capacity values obtained; lithium accessibly is paramount within the active material particles.

3.6 Conclusions

A variety of high voltage materials have been successfully made and characterised accordingly. Different techniques have been explored for preparing the materials, as well as looking at the different particle sizes of samples and potential carbon coating. $LiCu_{0.5}Mn_{1.5}O_4$ was successfully cycled at high discharge capacities with sufficient mixing when using the homogeniser; 93 % of the theoretical capacity was achieved on the first cycle with a reasonable cycle life.

Although a pure phase of $LiNiPO_4$ was synthesised, the material did not appear to be reversibly active in terms of intercalating lithium, and was realistically not a reasonable choice to be pursued as a candidate for the next generation of Li-ion batteries.

$LiCoPO_4$ showed signs of promise, with ~ 50 % of the theoretical capacity achieved on the first synthesis attempt. The cycle life was poor, but the degradation was not a rapid decay, instead showing consistent capacity loss over the first ~10 cycles. The voltage window of activity is not above 5 V, which would also allow less strenuous conditions for the high voltage electrolytes that will be tested. It was therefore decided that $LiCoPO_4$ would be an ideal material to study further within this research project.

3.7 References

1 Y. Ein-Eli, J. Electrochem. Soc., 1997, **144**, L205.

2 M. M. Thackeray, P. J. Johnson, L. A. de Picciotto, P. G. Bruce and J. B. Goodenough, Mater. Res. Bull., 1984, **19**, 179–187.

3 J. M. Tarascon, J. Electrochem. Soc., 1991, **138**, 2859.

4 Y. Ein-Eli, J. Electrochem. Soc., 1999, **146**, 908.

5 P. Strobel, A. Ibarra Palos, M. Anne and F. Le Cras, J. Mater. Chem., 2000, **10**, 429–436.

6 M.-C. Yang, B. Xu, J.-H. Cheng, C.-J. Pan, B.-J. Hwang and Y. S. Meng, Chem. Mater., 2011, **23**, 2832–2841.

7 F. O. Ernst, H. K. Kammler, A. Roessler, S. E. Pratsinis, W. J. Stark, J. Ufheil and P. Novák, Mater. Chem. Phys., 2007, **101**, 372–378.

8 Y. Ein-Eli, J. Electrochem. Soc., 1999, **146**, 908.

9 W. A. van Schalkwijk and B. Scrosati, Eds., Advances in Lithium-Ion Batteries, Springer US, Boston, MA, 2002.

10 Q. Zhong, J. Electrochem. Soc., 1997, **144**, 205.

11 Y. Shao-Horn, Solid State Ionics, 2001, **139**, 13–25.

12 H. Kawai, M. Nagata, H. Tukamoto and A. R. West, J. Power Sources, 1999, **81-82**, 67–72.

13 Y. Ein-Eli, J. Electrochem. Soc., 1998, **145**, 1238.

14 H. Shigemura, M. Tabuchi, H. Kobayashi, H. Sakaebe, A. Hirano and H. Kageyama, J. Mater. Chem., 2002, **12**, 1882–1891.

15 K. Amine, H. Tukamoto, H. Yasuda and Y. Fujita, J. Power Sources, 1997, **68**, 604–608.

16 I. Belharouak, Ed., Lithium Ion Batteries - New Developments, InTech, 2012.

17 A. K. Padhi, J. Electrochem. Soc., 1997, **144**, 1188.

18 J. Wolfenstine and J. Allen, J. Power Sources, 2005, **142**, 389–390.

19 S. Okada, S. Sawa, M. Egashira, J. Yamaki and M. Tabuchi, 2001, **98**, 432–434.

20 J. Wolfenstine and J. Allen, J. Power Sources, 2005, **142**, 389–390.

21 C. M. Julien, A. Mauger, K. Zaghib, R. Veillette and H. Groult, Ionics (Kiel)., 2012, **18**, 625–633.

22 J. J. Biendicho and A. R. West, Solid State Ionics, 2011, **203**, 33–36.

23 M. Despotopoulou and M. T. Burchill, Prog. Org. Coatings, 2002, **45**, 119–126.

24 D. Morgan, A. Van der Ven and G. Ceder, Electrochem. Solid-State Lett., 2004, **7**, A30.

25 S. M. Rommel, N. Schall, C. Brünig and R. Weihrich, Monatshefte für Chemie - Chem. Mon., 2014, **145**, 385–404.

26 I. Abrahams and K. S. Easson, Acta Crystallogr. Sect. C Cryst. Struct. Commun., 1993, **49**, 925–926.

27 A. Yamada, M. Hosoya, S.-C. Chung, Y. Kudo, K. Hinokuma, K.-Y. Liu and Y. Nishi, J. Power Sources, 2003, **119-121**, 232–238.

28 L. Dimesso, D. Becker, C. Spanheimer and W. Jaegermann, J. Solid State Electrochem., 2012, **16**, 3791–3798.

29 D.-W. Han, Y.-M. Kang, R.-Z. Yin, M.-S. Song and H.-S. Kwon, Electrochem. commun., 2009, **11**, 137–140.

30 K. Amine, Electrochem. Solid-State Lett., 1999, **3**, 178.

31 A. Manthiram, J. Phys. Chem. Lett., 2011, **2**, 176–184.

32 J. Yang and J. J. Xu, J. Electrochem. Soc., 2006, **153**, A716.

33 J. Wolfenstine, J. Read and J. L. Allen, J. Power Sources, 2007, **163**, 1070–1073.

34 P. A, J. Pizarro, A. Goni, T. Rojo and M. Arriortua, An. Quim. 1998, **94**, 383–387.

Chapter 4:

$LiCoPO_4$ Optimisation and Investigation

4.1 Introduction

This chapter focuses on optimising the performance of $LiCoPO_4$ as a cathode material by exploring different solvothermal methods and different particle coatings. Different solvents and atmospheric heating conditions were attempted, which did improve the performance of the electrode in terms of capacity and cycle life. Different carbon coating loadings on the particle surface were investigated, as well as different percentages of active material to carbon within a composite electrode. Ruthenium oxide (RuO_2) was also used as a particle coating, and the performance was analysed.

4.2 $LiCoPO_4$ Solvothermal Synthesis

A solvothermal synthesis method may allow more control for crystallite size, shape and aggregation. The metal salts were combined and heated inside an autoclave which allows for the $LiCoPO_4$ particles to grow under a heat treatment step dispersed within the solvent solution. By changing the solvent conditions, the particle morphology can be controlled.

Figure 4.1 depicts the solvothermal synthesis steps taken. In a typical route, 0.01 mol of H_3PO_4 (85 % Sigma Aldrich) and 0.03 mol of LiOH (Sigma Aldrich) were mixed first in 40 ml of the DEG-H_2O (diethylene glycol in water) mixed solvent (6:1) with strong magnetic stirring for 20 minutes to form a white Li_3PO_4 suspension. 0.01 mol of $CoSO_4 \cdot 7H_2O$ (Sigma Aldrich) was pre-dissolved in 20 ml of the DEG-H_2O mixed solvent and added slowly. The purple solution was stirred for another 20 minutes and then transferred to an autoclave and heated at 180 °C for 10 hours and allowed to cool naturally. The resulting blue solution was filtered, and washed through with ethanol and water subsequently three times via centrifugation. The centrifuge was set at 8500 rpm and was spun for 5 minutes.

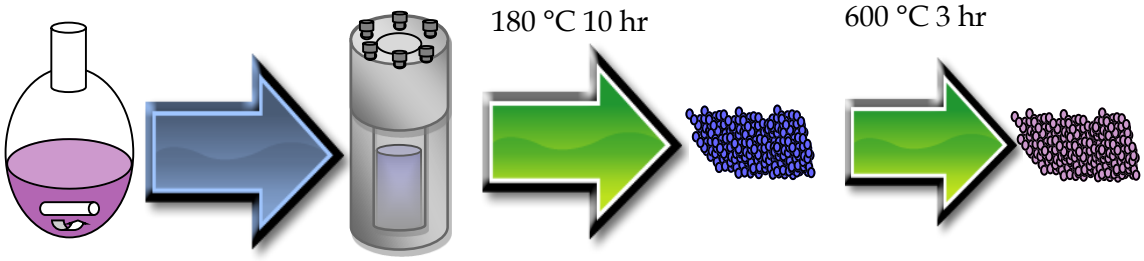

Figure 4.1 - The image depicts a typical solvothermal synthesis route taken.

The blue powder was then ground using a pestle and mortar before being heated for a second time at 600 °C under the specified atmospheric conditions. The powder was then allowed to cool naturally.

4.3 $LiCoPO_4$ Solvothermal Synthesis and Characterisation

The solvothermal synthesis method mainly used within this chapter had a solvent mixture of DEG:H_2O (6:1) and was heated under dry air in the second heat treatment step. **Figure 4.2** displays the XRD pattern obtained along with the refinement fit shown in red.

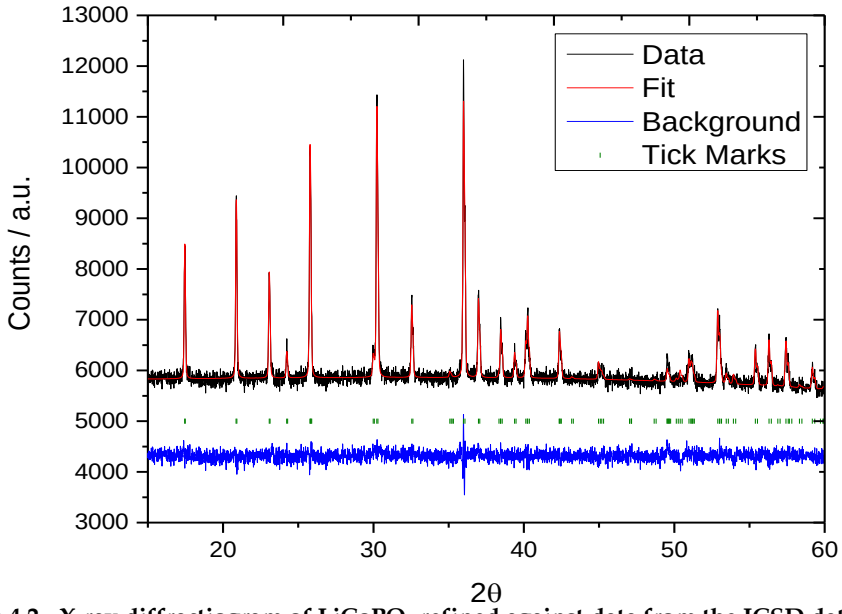

Figure 4.2 - X-ray diffractiogram of $LiCoPO_4$ refined against data from the ICSD database.[1]

Lattice constants: a = 10.20866(3), b = 5.92620(2) and c = 4.70359(9), α = β = γ = 90° wRp 1.48 % Rp 1.17 %.

Rietveld refinement was used to fit the standard triphylite model in space group *Pmna* which were similar values to those described in the literature.[1] The XRD pattern contains the olivine phase with minimal impurities.

Scanning electron microscopy (SEM) images were collected using Jeol JSM-6500 FEGSEM with 15 kV accelerating voltage and secondary electron imaging. **Figure 4.3** depicts the SEM image of the $LiCoPO_4$ particles using the mixed solvent of DEG:H_2O (6:1). The image shows elongated particles that were ~1 μm in width and 3-4 μm in length. The particles were uniform in size and shape.

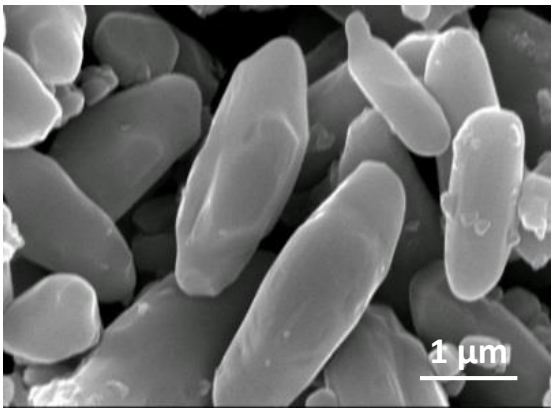

Figure 4.3 - SEM image of the $LiCoPO_4$ particles.

Previous studies on olivine structured $LiMPO_4$ (M = Fe, Mn) by solvothermal methods have shown that the addition of DEG increased the viscosity of the precursors to limit the particle size as well as inhibit the crystal growth by capping the crystal faces.[2] The source of the metal salt plays an important role in controlling the particle morphology. The use of SO_4^{2-} as a source of metal salt possesses a higher charge number than that of Cl^- and Ac^-, which may selectively adsorb on certain planes.[3] LiOH was first pre dissolved in H_3PO_4 to form a white Li_3PO_4 suspension. $CoSO_4 \cdot 7H_2O$ was pre-dissolved to aid solubility as the solvent mixture contained a minimum amount of water.

4.4 Particle Size Morphology

4.4.1 Changing the Solvent Conditions

Different solvent conditions were attempted but the volume of each solvent remained constant. **Figure 4.4** displays the SEM images obtained of the different particles as well as the cycling performance at 0.1 C using BASF LP57 electrolyte. Each XRD pattern was refined and indicated the single olivine $LiCoPO_4$ was present with minimal impurities. The different solvent conditions and atmospheric conditions show that the particle shape and size can be manipulated to gain either large (micro) or small (nano) sized particles.

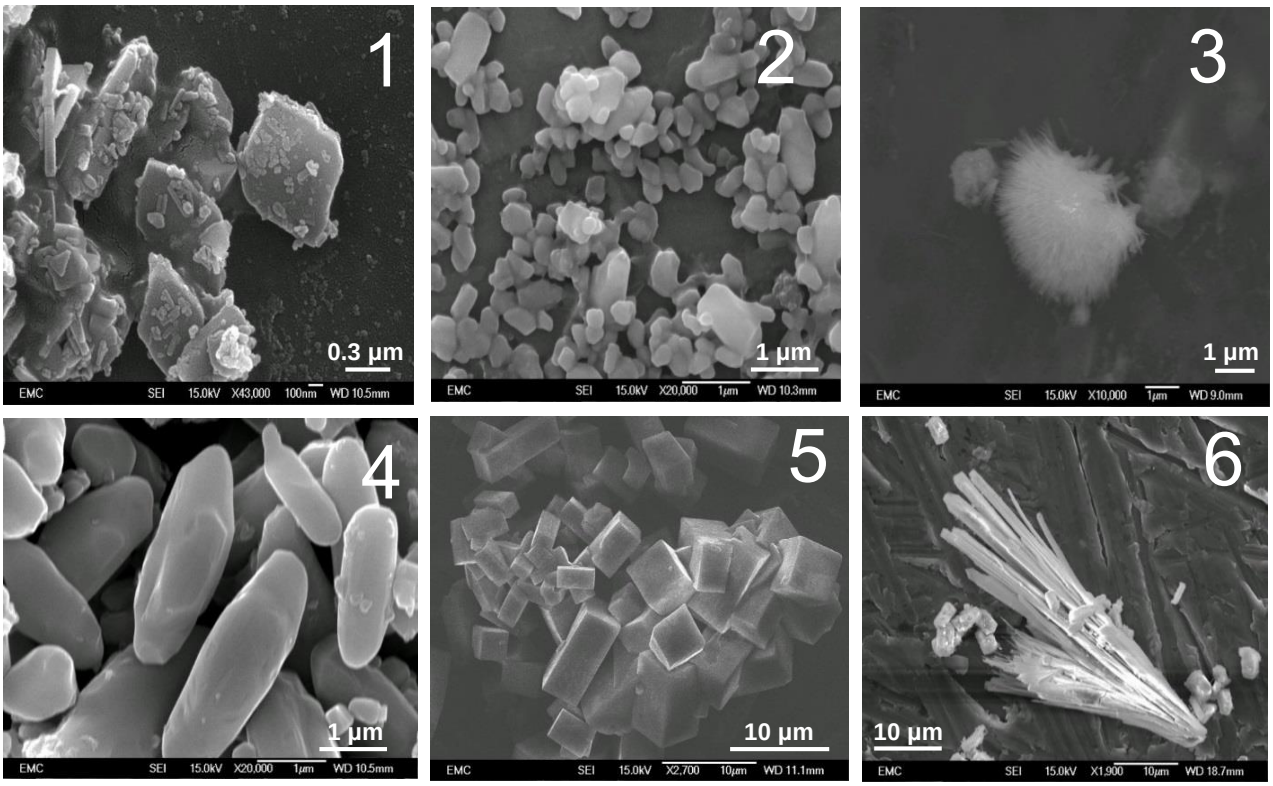

1 No Second Heat Treatment (DEG) 2 DEG – Argon 3 Benzyl Alcohol:Water (1:1) – Argon 4 DEG – Air 5 Benzyl Alcohol:DEG – Argon (1:1) 6 Water – Argon

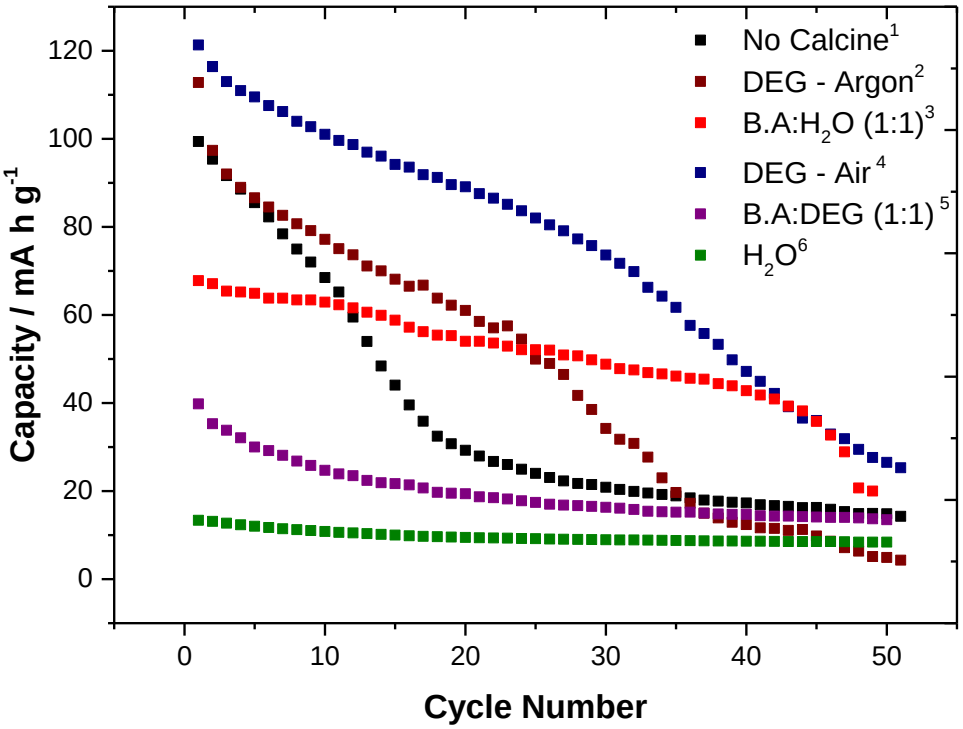

Figure 4.4 - SEM images of different $LiCoPO_4$ morphologies from different synthesis conditions along with the $LiCoPO_4$ PTFE pellet cycling performance at 0.1 C conducted in a lithium half-cell with BASF LP57 1 M $LiPF_6$ EC:EMC (3:7) electrolyte.

All the different $LiCoPO_4$ samples were refined using Rietveld refinement and XRD studies revealed that the olivine phase was present with space group *Pnma*. The powders were made into PTFE pellets and incorporated into Swagelok cells and cycled at 0.1 C using the same potential limits of 3.5 – 5.0 V using LP57 (BASF) electrolyte. The cycling performance results from **Figure 4.4** suggest an optimum particle size to achieve a good performance. If the particles are small, a good initial discharge capacity is obtained, however the large surface area may lead to more electrolyte breakdown on the surface of the particles, which could increase the resistance over many cycles and lead to capacity fade. If the particles are too big however, then lithium intercalation into the very core of the particle proves difficult. This is evident in the poorer discharge capacities obtained as not all of the lithium inside the larger particles is accessible. The best performing material was synthesised using DEG:H_2O (6:1) solvent and in the second heat treatment the atmospheric condition was under dry flowing air. It is this method that was chosen to investigate the $LiCoPO_4$ system further in the following sections.

4.5 Atmospheric Heating Conditions

4.5.1 Insight

Figure 4.5 cycling data showed a large difference when heating under dry air compared to dry argon. The particle size under dry argon is smaller, but Wolfenstine et al. observed a decrease in capacity when heated under air (~72 mA h g^{-1}) compared to argon (~101 mA h g^{-1}) using a typical solid state reaction method. It was concluded that the most likely reason for an increase in the capacity was due to a smaller particle size and an increase in the electronic conductivity due to the presence of cobalt phosphides and increased carbon content.[4] The cycling data in this report however suggests that heating under dry air in fact improves the electrochemical performance, with no carbon coatings presence.

4.5.2 $LiCoPO_4$ Performance Under Dry Air/Argon

When heating under air, the increase in performance in terms of capacity under the same conditions is ~11 %. $LiCoPO_4$ (Sigma Aldrich, Battery Grade 99.9 %) powder was purchased and heated under dry argon and also air at 600 °C for 3 hours. When heated under air, the discharge capacity increased by 31 % compared to heating under argon. The particle size and XRD patterns of each sample are very similar, suggesting an intrinsic conductivity change or changes in oxidation state of the cobalt. XANES data was collected on each powdered sample to observe any changes in the cobalt oxidation state.

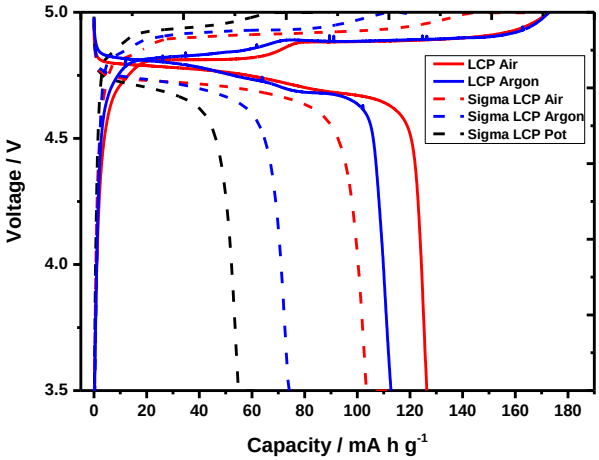

Figure 4.5 - Cycling data of $LiCoPO_4$ and shop bought $LiCoPO_4$ (Sigma Aldrich battery grade) which has been heated in either dry air or dry argon. Lithium half-cells was constructed at 0.1 C using BASF LP57 electrolyte.

XANES spectra were collected for each sample using transmission measurements from beamline B18 (Diamond Light Source, U.K.). The X-rays passed through each composite electrode pellet that was mounted onto the beamline.

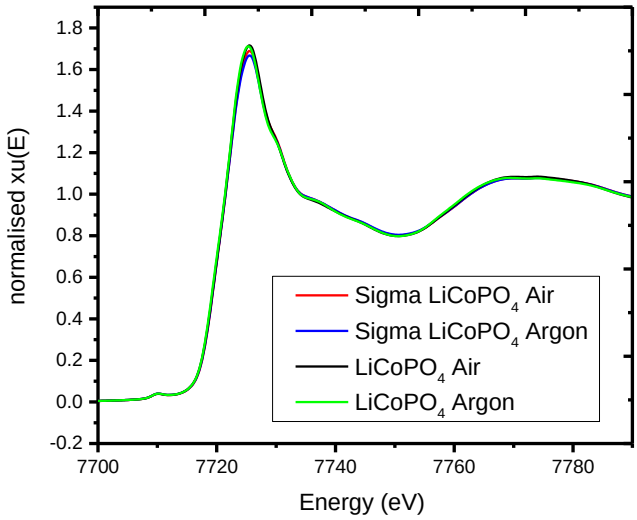

Figure 4.6 - Graph displaying the collected XANES data on the different $LiCoPO_4$ powders.

The absorption edge position is intimately related to the oxidation state of the cobalt within the samples, and the data shows that the edges are exactly superimposed regardless of the atmospheric heating conditions. This technique analyses the bulk of the pellet, and that the lack of any distinct changes does not preclude any possible oxidation state changes in a small fraction of the cobalt atoms present e.g. in a surface layer.

The performance of the shop brought $LiCoPO_4$ (Sigma Aldrich battery grade 99.9 %) was surprising low in comparison to the synthesised $LiCoPO_4$ from within this report. The poor performance was due to very large particles being found within the powdered sample, which would hinder full lithium intercalation inside the depths of the particles.

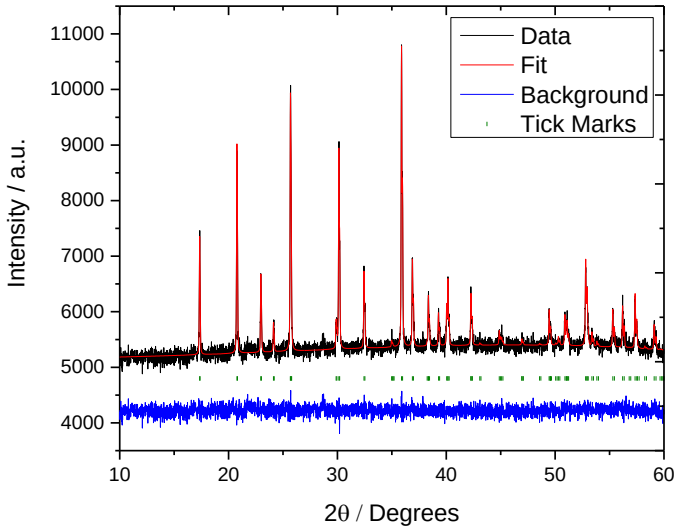

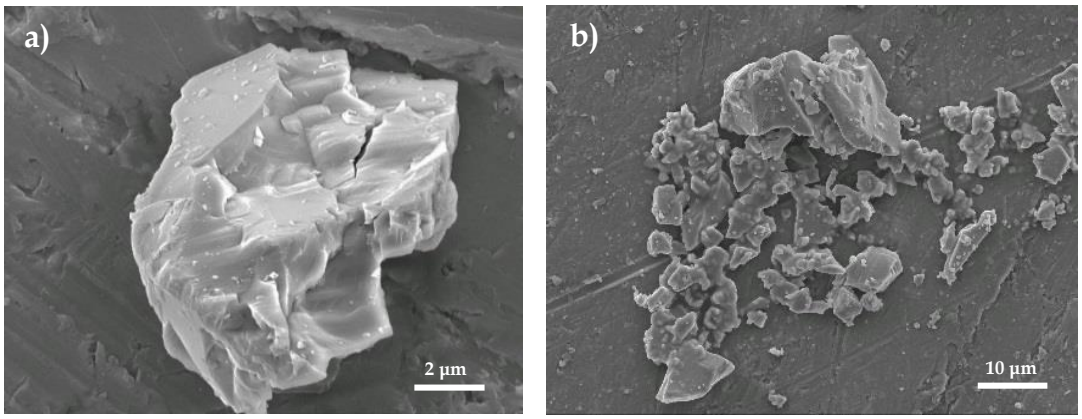

Figure 4.7 - X-ray diffractiogram of $LiCoPO_4$ (Sigma Aldrich battery grade 99.9 %) refined against data from the ICSD database[1] and obtained SEM images . Lattice constants: a = 10.20396(8), b = 5.92149(6) and c = 4.699500, α = β = γ = 90°, wRp 1.48 % Rp 1.17 %. a) From pot b) After air treatment.

4.5.2.1 Conductivity Tests

Electronic conductivity tests were carried out on each powdered sample with 10 % PTFE binder and 90 % active material by weight. The pellets (with no carbon present) were incorporated into steal Swagelok cells and cyclic voltammograms of each individual pellet were taken.

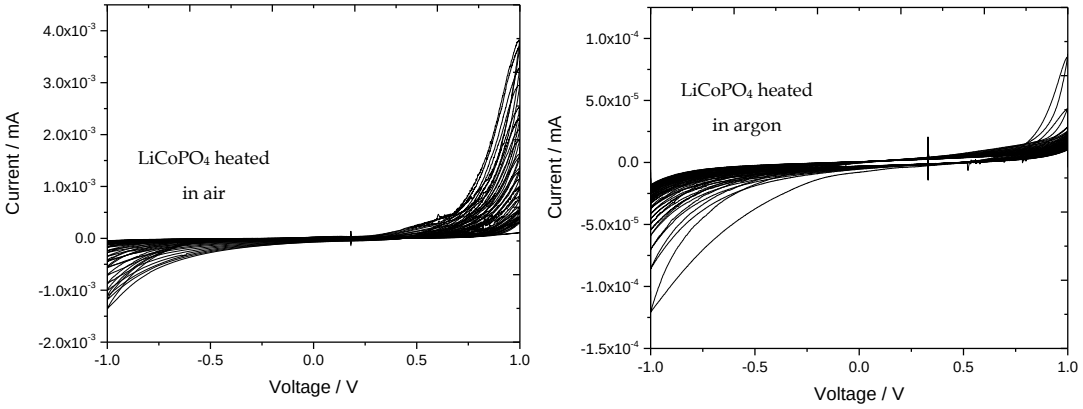

Figure 4.8 - Cyclic voltammograms of the different $LiCoPO_4$ powders heated under different atmospheric conditions. The powders were incorporated into PTFE composite electrodes with carbon as described before and cycled between -1.0 and 1.0 V at a scan rate of 10 mV s^{-1}.

From knowing the thickness, surface area of the electrode and gradient from one of the CV cycles the electronic conductivity was calculated. The 20th cycle of each CV was taken for the gradient value. The electronic conductivity of $LiCoPO_4$ when heated under air was 5.40 x 10^{-6} S cm^{-1} and when heated under argon it was 5.01 x 10^{-5} S cm^{-1}. The higher electronic conductivity for $LiCoPO_4$ heated under argon contradicts the lower capacities obtained, however the ionic conductivity is also an important aspect that needs to be taken into account for lithium-ion electrodes.

4.5.2.2 X-ray Photoelectron Spectroscopy

XPS measurements were performed in ultra-high-vacuum (10^{-10} mbar) VG ESCALAB 220i-XL photoemission spectroscopy system equipped with a monochromatic Al Kα (1486.6 eV) X-ray source. Samples were charged corrected by setting the adventitious carbon peak to the binding energy value of 284.8 eV.

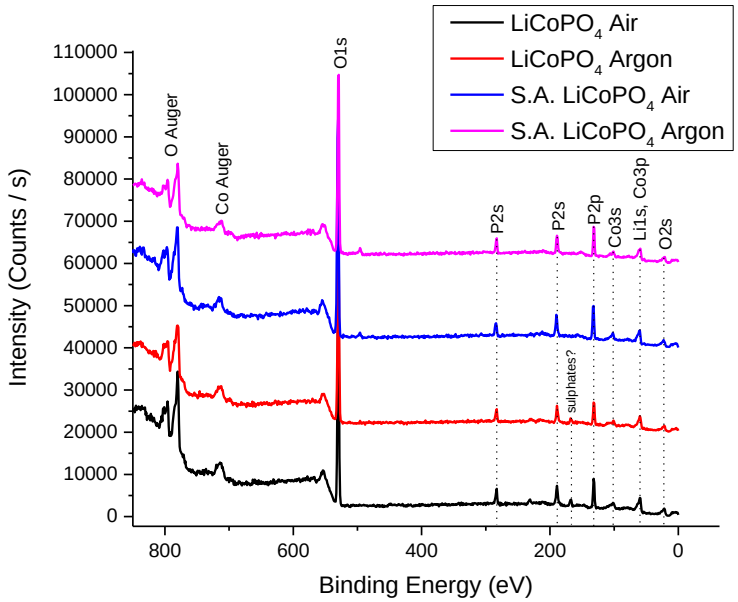

Figure 4.9 - XPS survey scan of each powdered $LiCoPO_4$ sample.

The survey scan suggests that sulphates may be present within the $LiCoPO_4$ synthesised within this report (**Section 4.2**), and the overall Co2p XPS fitted profile is difficult to fully understand. Within the literature, it is difficult to pin point Co^{2+} and Co^{3+} regions which seem to overlap, with multiple signals seen which are not discussed in detail and inconsistent about what this means.[5,6,7] The change in binding energy from Co^{+2} to Co^{+3} can be assumed as small and that many of the samples looked at in the literature contain both. A combination of small changes in binding energy and variations in XPS spectra given in the literature make it difficult to confidently extract any information about the cobalt environment.

Satellite peaks always seem to be ~6 eV away from the main signal(s) in the literature, so there is a possibility that within the samples there is $Co^{2+/3+}$ present. This would be due to surface oxidation and the effect of heating under dry air.

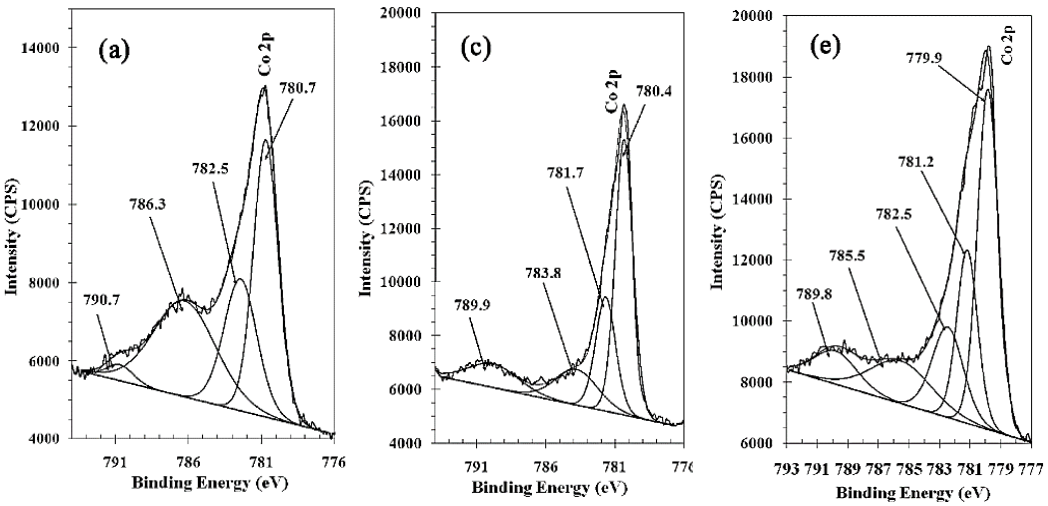

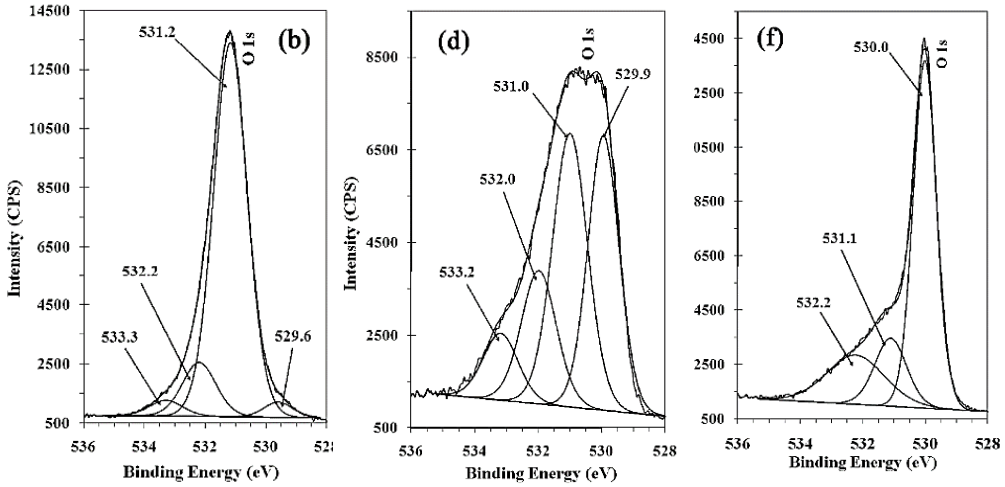

Figure 4.10 - High resolution XPS spectra of the cobalt and oxygen environments. a),b) $Co(OH)_2$, c),d) CoO(OH) and e),f) Co_3O_4 obtained from reference[5] with permission.

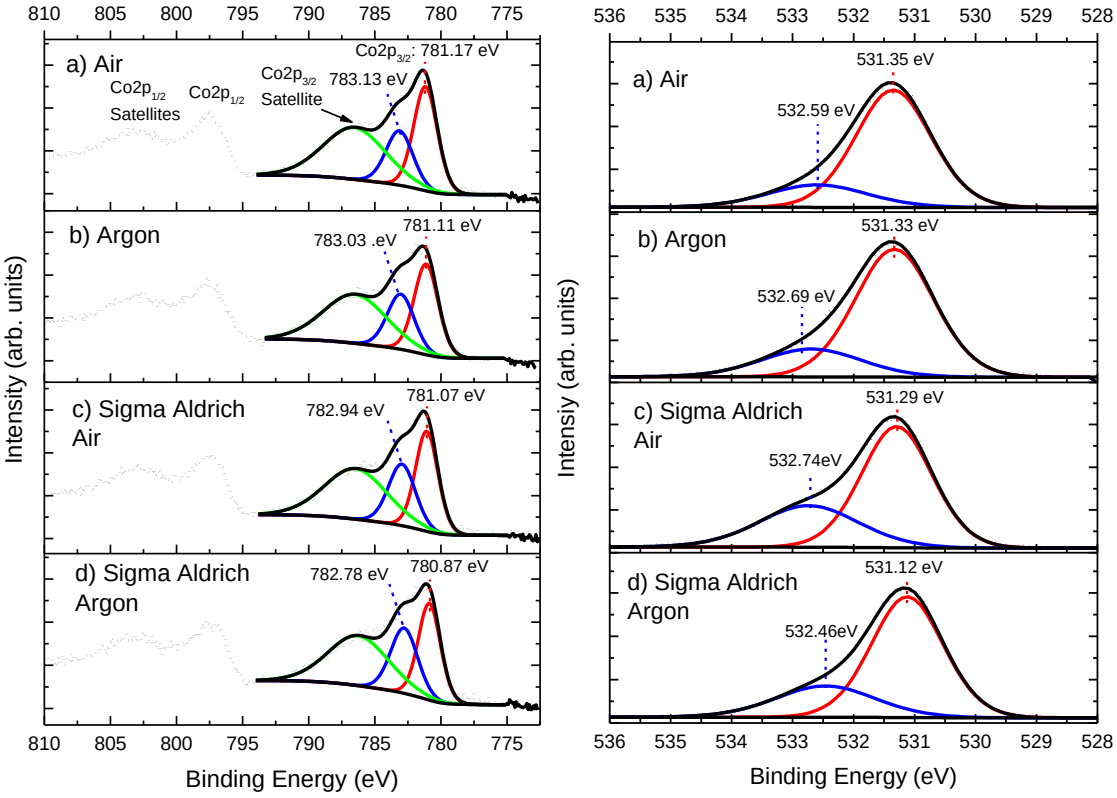

Figure 4.11 – XPS spectra of the cobalt and oxygen environments for the different powered samples.

The in-depth analysis that has been carried out on the different atmospheric heat conditions appears to suggest that differences in performances from galvanostatic cycling are purely a morphological effect.

4.6 $LiCoPO_4$ Composite Electrode

4.6.1 Electrochemical Performance

Galvanostatic cycling of the $LiCoPO_4$ pellets at 0.1 C shows two well defined plateaus connected by an intermediate region of sloping potential. These results suggest a two two-phase region that is reversible upon discharge.

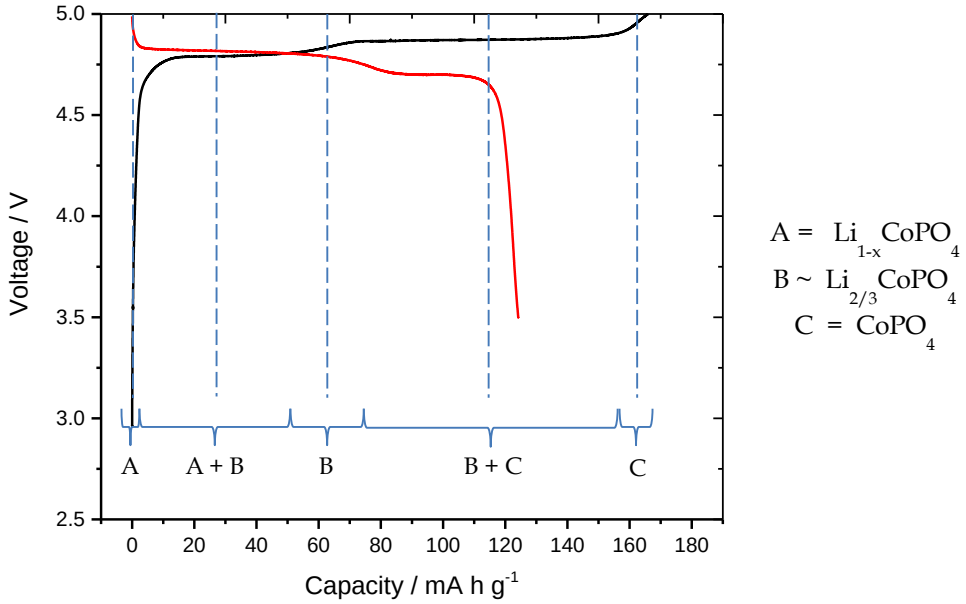

Figure 4.12 - Voltage profile of the during the first cycle conducted in a lithium half-cell with BASF LP57 1 M $LiPF_6$ EC:EMC (3:7) electrolyte. Blue lines correspond to the charge profile only.

Charging the half cell up to 5.0 V gave a capacity of 166 mA h g^{-1}. The theoretical capacity from $LiCoPO_4$ is 167 mA h g^{-1}. SEI formation would have contributed a small amount of capacity to the overall value, however the charge profile suggests that most of the particles underwent lithium extraction.

At open circuit voltage, $LiCoPO_4$ (phase A) was present. The current was then applied and lithium extraction began; phase A remained within its concentration limits in terms of lithium until phase B started to form. The first flat plateau suggests the presence of phases A and B together (at the same potential) before phase A depletes completely and only phase B is present. The voltage begins to rise as phase B reaches its concentration limits until phase C starts to grow. The second plateau shows the existence of both phases B and C together until phase B has depleted and only phase C is present. At this high potential of ~4.9 V, $CoPO_4$ mainly exists across the bulk of the electrode and lithium extraction is near completion.

During discharge, the reversible phase transformations from phase C back to phase A (through the intermediate phase B) occurs. The discharge capacity at 3.5 V *vs.* Li/Li^+ is recorded at 124 mA h g^{-1}. This is considerably higher than with the solid state synthesis method reported in **Chapter 3**. 75 % of the charge capacity was recovered upon discharge, and the irreversible capacity loss was 42 mA h g^{-1}.

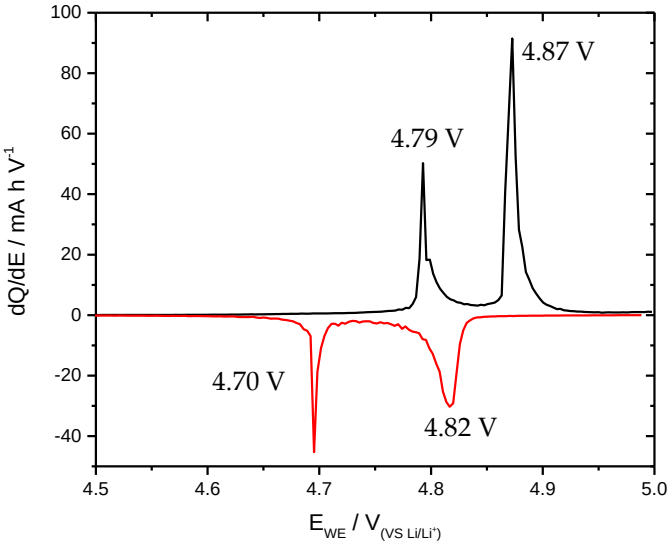

Figure 4.13 - dQ/dE plot of the first cycle of the composite electrode cycled in figure 4.12.

The majority of the charge was passed within the voltage region commonly associated with lithium extraction/insertion of $LiCoPO_4$ (4.7 – 4.9 V *vs.* Li/Li^+). The derivative of the charge passed with respect to voltage is shown in the dQ/dE plot in **Figure 4.13**. The form of the plot resembles a slow scan cyclic voltagmmogram. Analysis of the dQ/dE plot during lithium extraction highlights two peaks at 4.79 and 4.87 V *vs.* Li/Li^+. These peaks indicate an increase in the amount of charge passed, and can be associated with the beginning of the two two-phase regions that are formed upon lithium extraction. The peaks shown are asymmetric, which indicates nucleation of a new phase being formed. During discharge, two peaks are observed which are related to the reversible two two-phase formation during lithium insertion. The voltage peak positions are consistent with the flat voltage profiles shown from the galvanostatic cycling.

4.6.2 Impedance Analysis of the First Cycle

Impedance measurements were made throughout the first cycle of a three electrode cell containing $LiCoPO_4$ as the working electrode. The cell was charged or discharged to certain potentials, and then allowed to rest for 2 hours prior to impedance measurements. **Figure 4.14** shows the points at which impedance measurements were made throughout the first cycle.

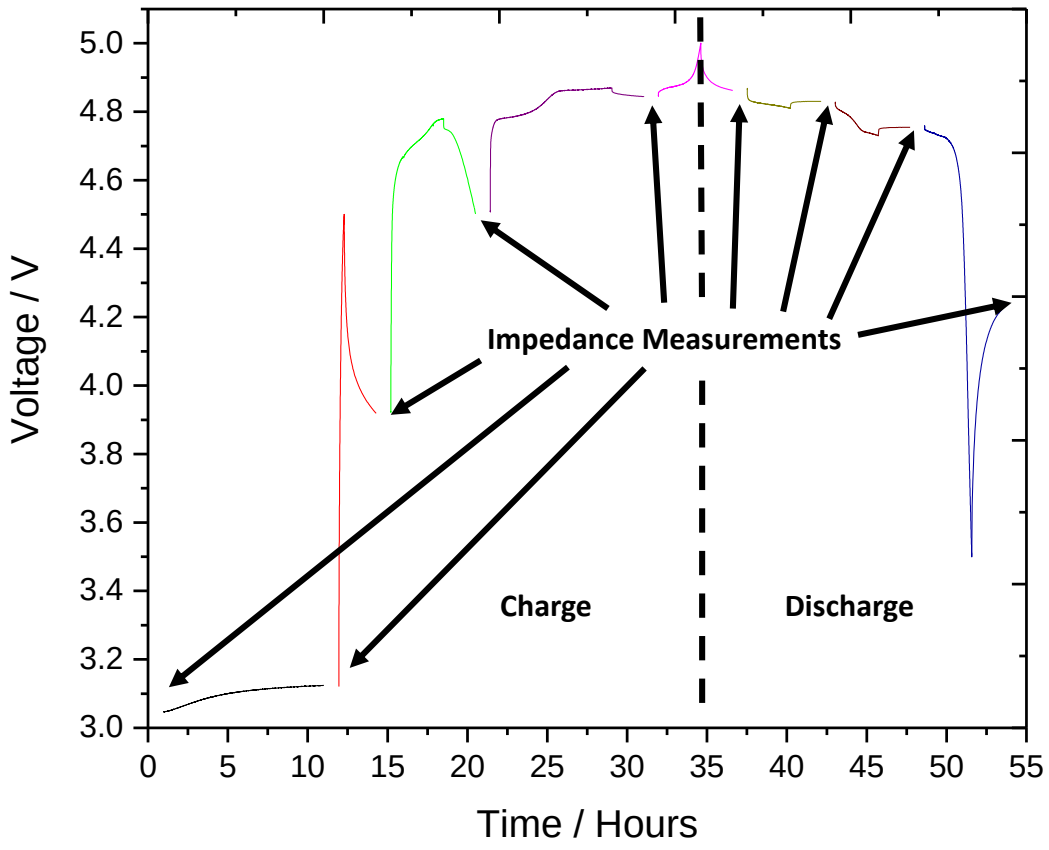

Figure 4.14 - Voltage profile of a composite electrode within a three electrode cell. Cycled at a rate of 0.1 C in BASF LP57 with rest periods of 1 hour prior to impedance measurements (arrows highlight measurement positions).

For comparison and as a control, impedance measurements were made on a three electrode cell containing a carbon pellet as the working electrode. The current applied to the carbon pellet was proportional to the amount of carbon present (by mass) within the $LiCoPO_4$ composite electrode cycled at 0.1 C.

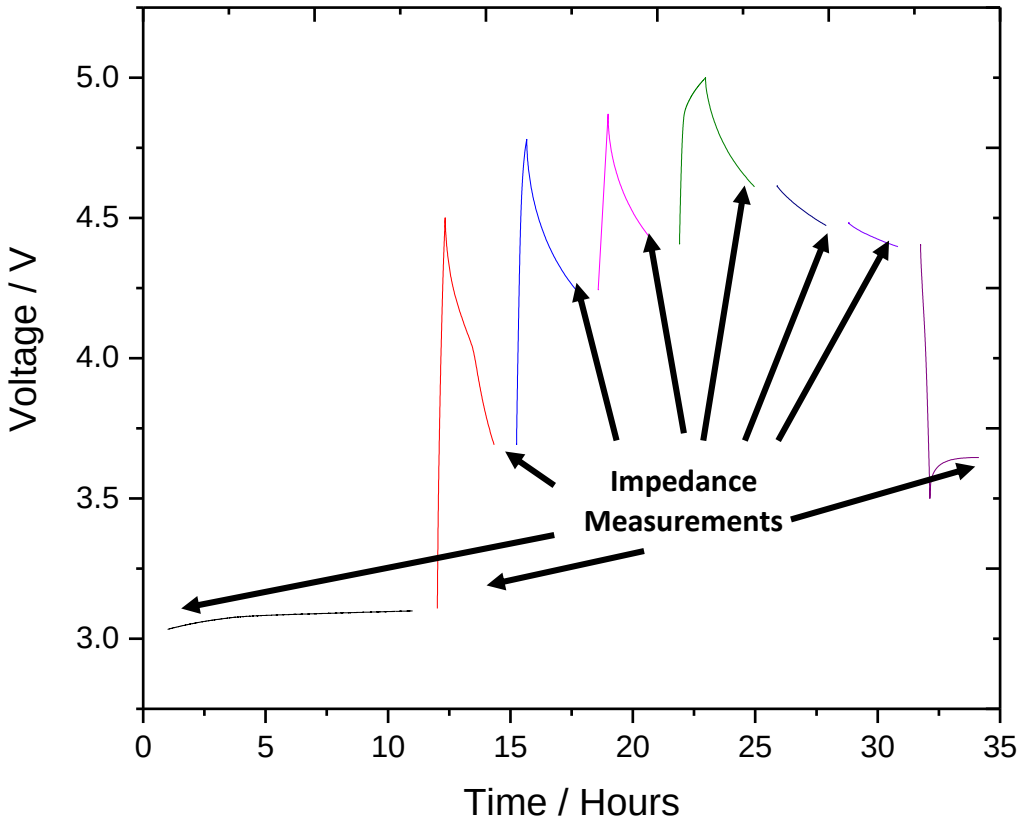

Figure 4.15 -Voltage profile of a carbon electrode within a three electrode cell. The pellet was made up of 80% carbon and 20% PTFE binder. Cycled at a rate comparable with the $LiCoPO_4$ cell (by carbon mass) in BASF LP57 electrolyte with 2 hour rest periods prior to impedance measurements (arrows highlight measurement positions).

During the open circuit period in both three electrode cells, the potential relaxed towards the equilibrium potential. In regions where no charge is being passed (OCV), the potential drops down and would eventually reach equilibrium potential. The OCV periods within the lithium intercalation regions for the $LiCoPO_4$ composite electrode, show a clear IR drop initially which suggests a significant over potential is required to extract or insert lithium ions in the $LiCoPO_4$ structure. At longer time the voltage decays towards equilibrium as the lithium concentration gradient across the electrode relaxes. The carbon pellet electrode shows large potential changes during relaxation which were expected as relatively very little charge storage occurs and the system can return to an equilibrium state quickly.

The impedance spectra obtained throughout the cycle are displayed in **Figure 4.16** as Nyquist plots. The plots display the impedance measurements obtain, the voltage was measured *vs.* a non-active lithium reference electrode.

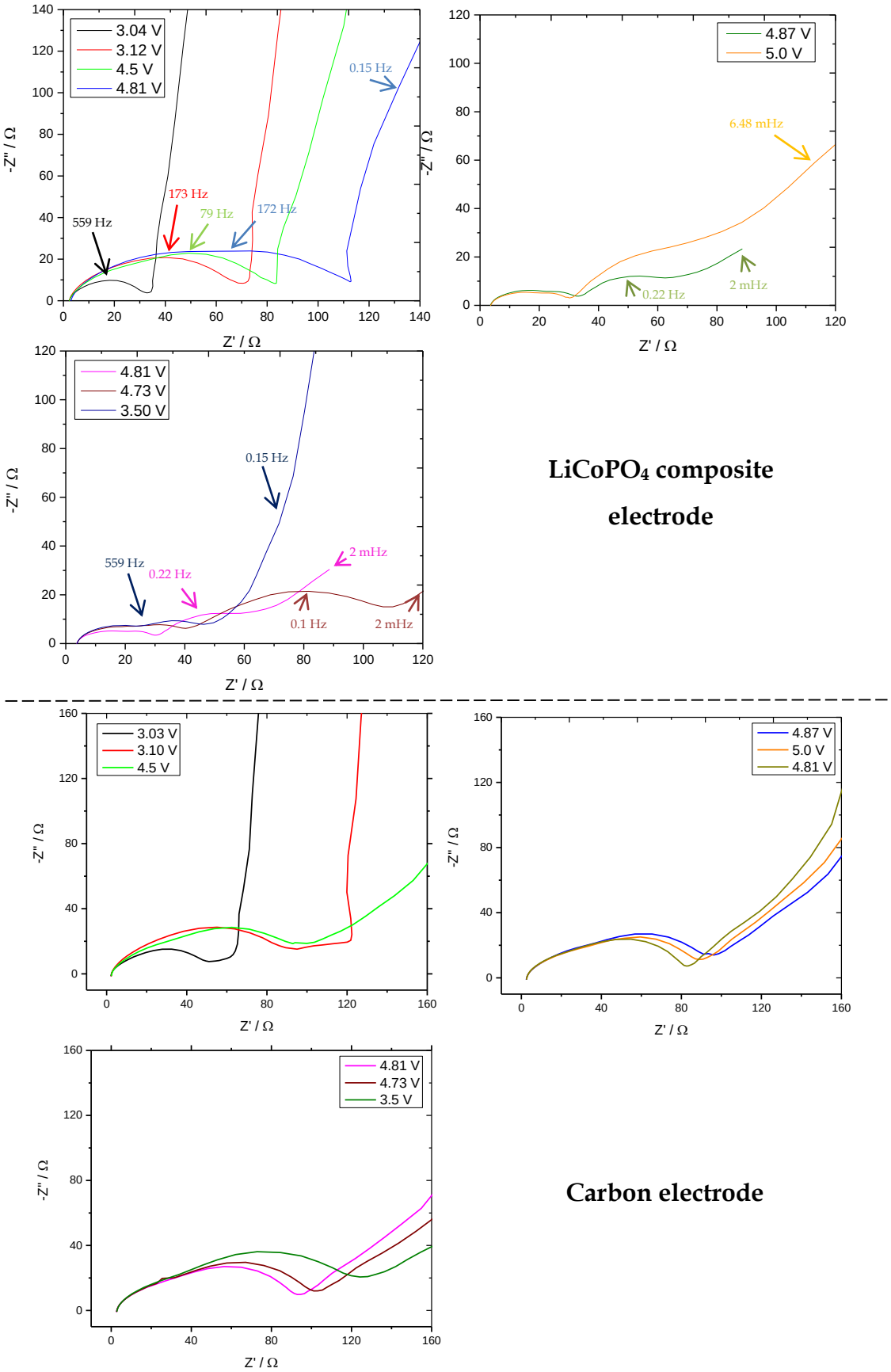

Figure 4.16 - Impedance spectra displayed in three sections in the form of a Nyquist plot. Frequency range 200 kHz to 2 mHz at 25 °C.

Carbon composite electrode

As current was applied to the carbon electrode the voltage rose steeply, the oxidising conditions and the high surface area of the carbon would likely cause reaction of surface species, adsorbed to the carbon, with the electrolyte, these type of reactions along with simple double layer charging are expected to account for the charge passed as the carbon electrode was cycled.

The carbon pellet impedance data was as expected for a high surface area carbon electrode charged to a high potential. Initially at 3.03 V *vs.* Li/Li^+ the impedance data is typical of a capacitor, at high frequencies the electrolyte resistance and contact resistance and double layer charging of the current collector dominate. At low frequencies close to ideal capacitive behaviour was observed due to the double layer charging of the high surface area electronically conductive carbon. As the voltage of the electrode increased during 'charge' the impedance response of the electrode changed, this is likely due to the oxidation of surface species and the electrolyte. A Warburg type response was observed at lower frequencies and replaced the capacitive behaviour previously observed when the electrode was at lower potential. The Warburg may be explained by the insertion of PF_6^- anions into the carbon at such high voltages which has been observed before at the same potential region.[8]

As the electrode is 'discharged' the impedance response did not return to that initially observed, this is suggested to be due to the decomposition products still present on the surface of the carbon particles and within the electrode.

$LiCoPO_4$ composite electrode

The impedance data obtained for the $LiCoPO_4$ composite electrode displayed similar trends when compared to the carbon pellet, however a significant difference was observed in the medium to low frequency region when the cell was at potentials at which lithium insertion/extraction occurs. The additional process is suggested to be associated with the reduction/oxidation of the active material, the resistance value associated with the charge transfer process and the capacitive behaviour associated with the charge stored via the redox processes.

Interestingly as the $LiCoPO_4$ electrode is discharged the low frequency response returns to more ideal capacitive behaviour, this may be due to higher porosity within the composite compared to the carbon pellet, due to larger $LiCoPO_4$ particles, which allows for fast ion movement throughout the electrode despite electrolyte oxidation and breakdown products present. **Figure 4.17** shows an example fit that was performed on the $LiCoPO_4$ composite electrode impedance data.

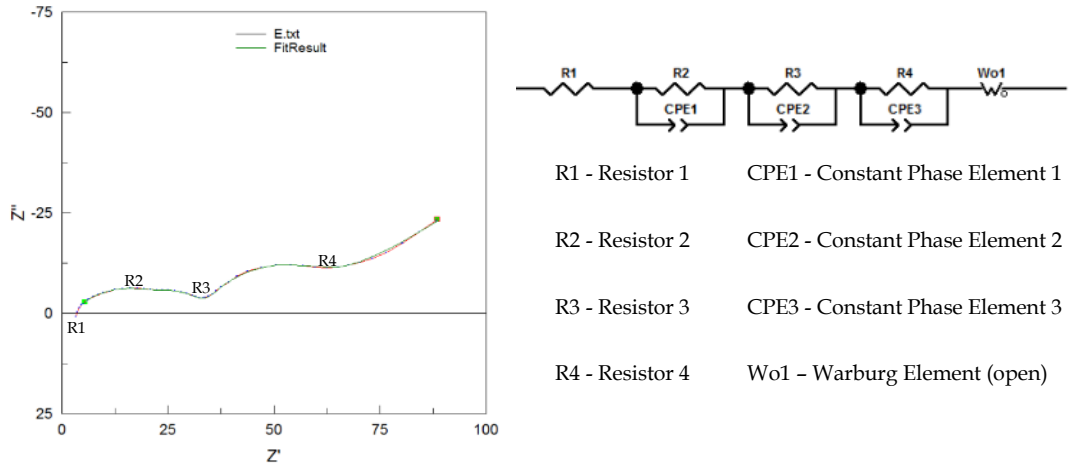

Figure 4.17 – Example of fitted Impedance spectra with the different resistance regions highlighted and the corresponding equivalent circuit for the Z-view™ data fittings.

Figure 4.18 shows the results from fitting the impedance data for the $LiCoPO_4$ composite electrode. R1, the uncompensated resistance, was observed to stay roughly constant through the charge and discharge profile. This was expected as the amount of charge carriers within the electrolyte was expected to remain relatively constant. R2 and R3 were combined (these represent contact resistance between the composite electrode and the current collector and active material – carbon particle to particle resistances) and show that this increased on charging up to the point of expected lithium intercalation. R4 is seen only during the expected lithium intercalation potential regions, which was associated with charge transfer resistance. The Warburg component is also only seen within this region, which may indicate lithium diffusion within the active material was also contributing to the observed low frequency response.

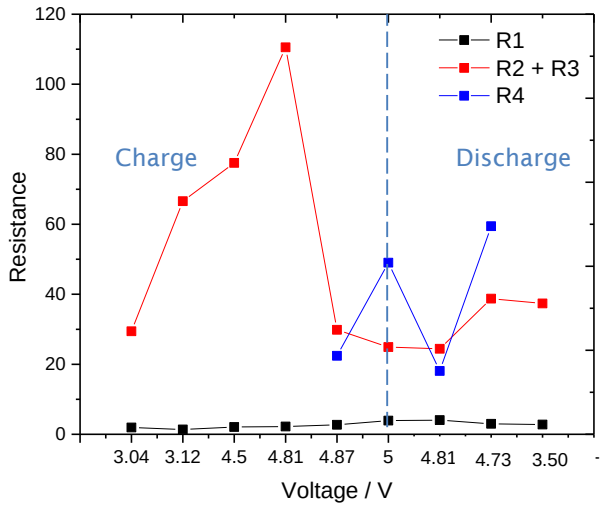

Figure 4.18 - Results from the $LiCoPO_4$ composite electrode fits of the different resistance values during charge and discharge.

At 3.50 V (end of discharge) the impedance data is very similar to the initial impedance taken before cycling, but now R2 and R3 are more much defined and the combination of R2 and R3 contribute a larger resistance (50 Ω vs. 30 Ω initially) , which could be due to a increase in particle to particle resistance or a reduction in contact area possibly caused by a layer of breakdown products present after the first charge/discharge cycle.

4.6.3 $LiCoPO_4$ Extended Cycling

Cycling of $LiCoPO_4$ composite electrode at 0.1 C was shown in **Figure 4.19**. The potentials of the two plateaus shown during charge shift up to higher potentials gradually during cycling, suggesting an increase in cell resistance. Initially, the composite electrode remains relatively stable with controlled capacity losses of 1 – 2 mA h g^{-1} per cycle. After 40 cycles, the cell is inactive, with capacities recorded at < 10 mA h g^{-1}.

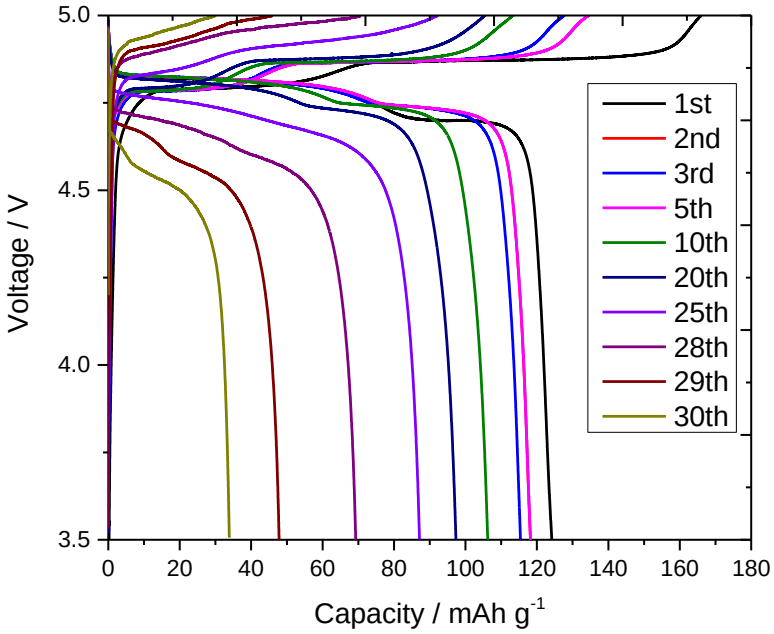

Figure 4.19 - Electrochemical cycling of a half-cell showing the first 30 cycles. Cycled at 0.1 C conducted in a lithium half-cell with BASF LP57 1 M $LiPF_6$ EC:EMC (3:7) electrolyte.

Figure 4.20 is a dQ/dE plot of the corresponding 30 cycles of the composite electrode. Peaks shift to higher potentials on charging and lower potentials on discharge, suggesting an increase in resistance. The peaks also broaden, suggesting that the resistance is distributed over different values for different particles.

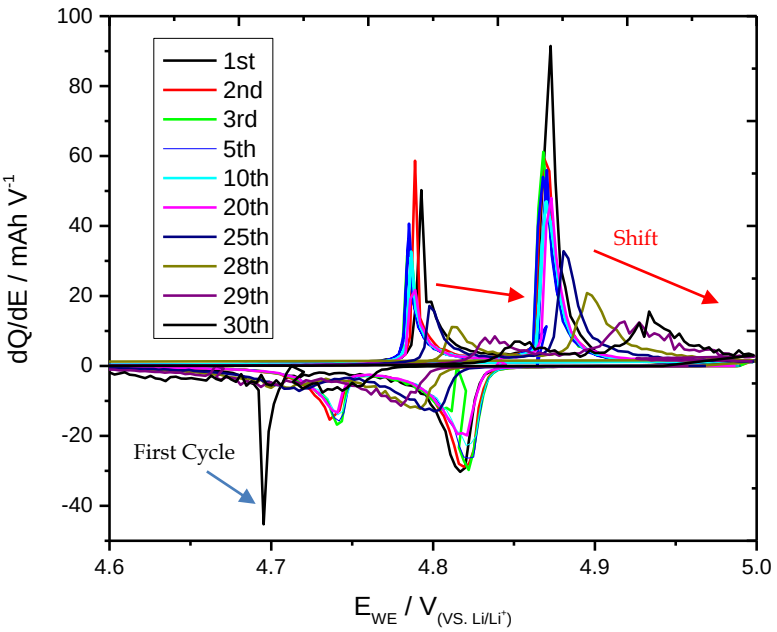

Figure 4.20 - A dQ/dE plot of the composite electrode after 30 cycles conducted in a lithium half-cell with BASF LP57 1 M $LiPF_6$ EC:EMC (3:7) electrolyte.

4.6.4 AC Impedance During Extended Cycling

Figure 4.21 highlights (red arrows) where AC impedance measurements were taken at the end of each cycle, with a 1 hour rest between cycling and impedance measurement.

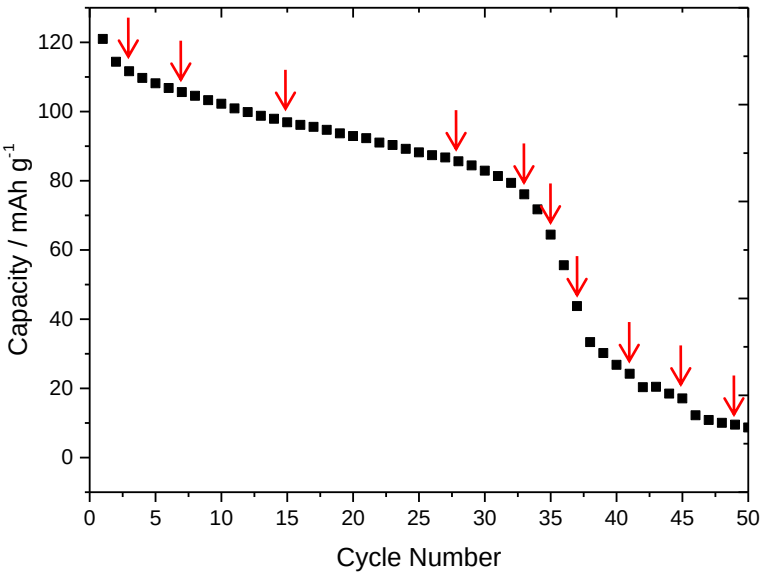

Figure 4.21 - Cycling of a composite electrode, with red arrows highlighting where the AC impedance measurements were taken.

AC impedance measurements were taken during the relatively stable capacity cycling region, and targeted more specially at the region of degradation of the half cell. **Figure 4.22** shows that the resistance has increased vastly at the point where the capacity

became to drop significantly. This large increase in resistance can be associated the growing SEI layer reaching its limit in terms of lithium permeability. It can be stipulated that the SEI layer growing has reached a limit in terms of passing lithium, and the thick SEI layer is now not penetrating towards lithium effectively ending the insertion/extraction into the host lattice and degrading the cells performance.

Fitting of the spectra was conducted using Z-view™ software and using the equivalent circuit displayed in the figure. During initial cycling, the resistance remained relatively constant, and gradually increased at low frequencies.

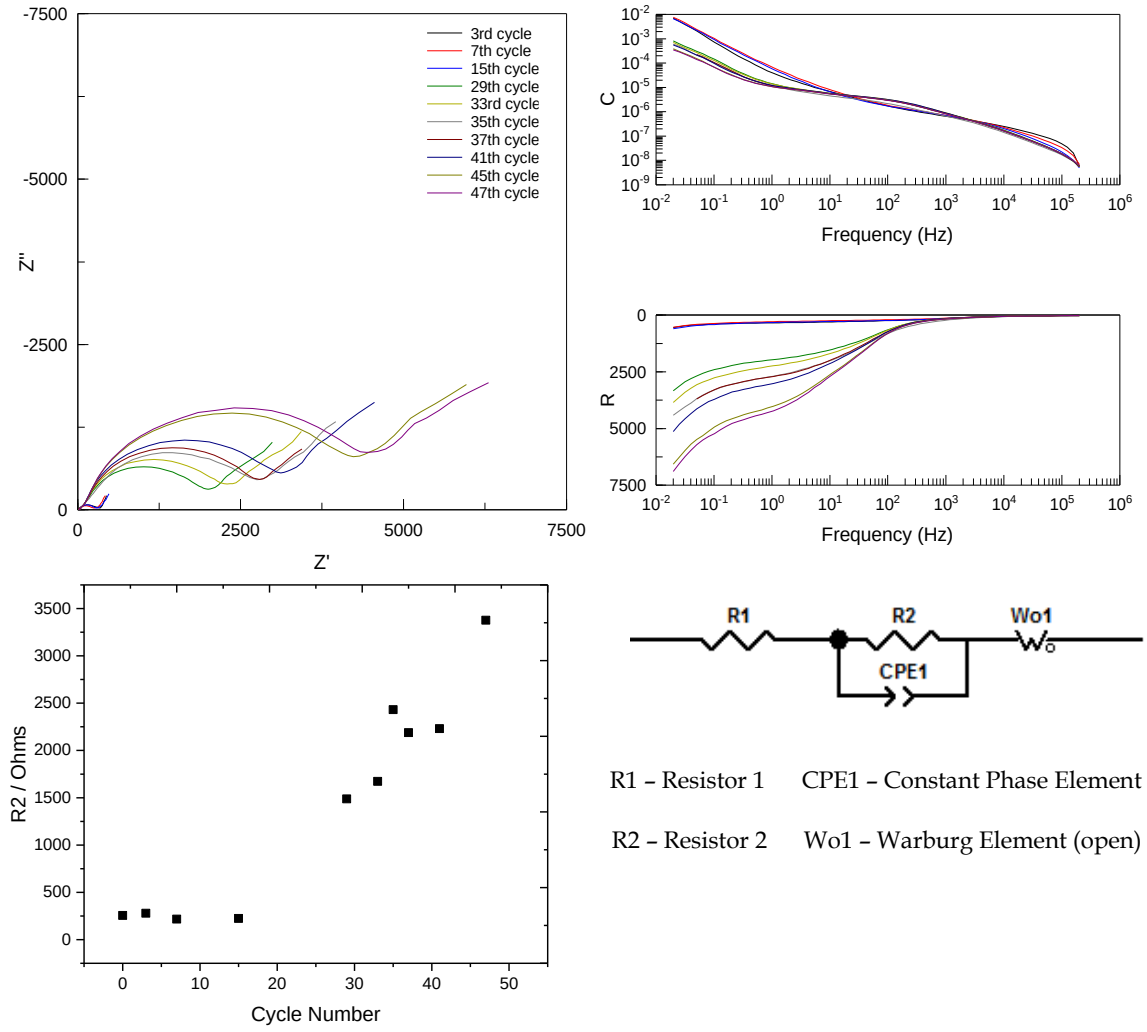

Figure 4.22 - AC impedance plots from the corresponding cycle number highlighted in figure 4-10 along with the associated equivalent circuit for the Z-view™ data fittings.

The impedance measurements were taken using a two electrode cell setup. This means that the counter lithium electrode also acted as the reference electrode, which would have had side reactions occurring such as SEI formation as current is passed through the electrode. The impedance does not take the working electrode ($LiCoPO_4$ composite)

solely into account as with the three electrode impedance data discussed earlier. This could be why no second arc is seen during the impedance of the two electrode cell. However, the overall general increase in the internal resistance of the cell is still relevant, and the reasonable conclusion that the cycle life faded due to increased internal cell resistance is still valid.

4.7 $LiCoPO_4$ Composite Electrode Formulation

The performance of composite electrodes will be sensitive to various ratios of active material, carbon, binder and electrolyte in the voids of the particles. The influence of a change in the percentage of carbon within the composite electrode for the $LiCoPO_4$ system was investigated.

Six different formulations were chosen for the investigation. **Figure 4.23** shows the ternary diagram of the 6 different composite electrodes along with the cycling data within a Swagelok cell under the same conditions.

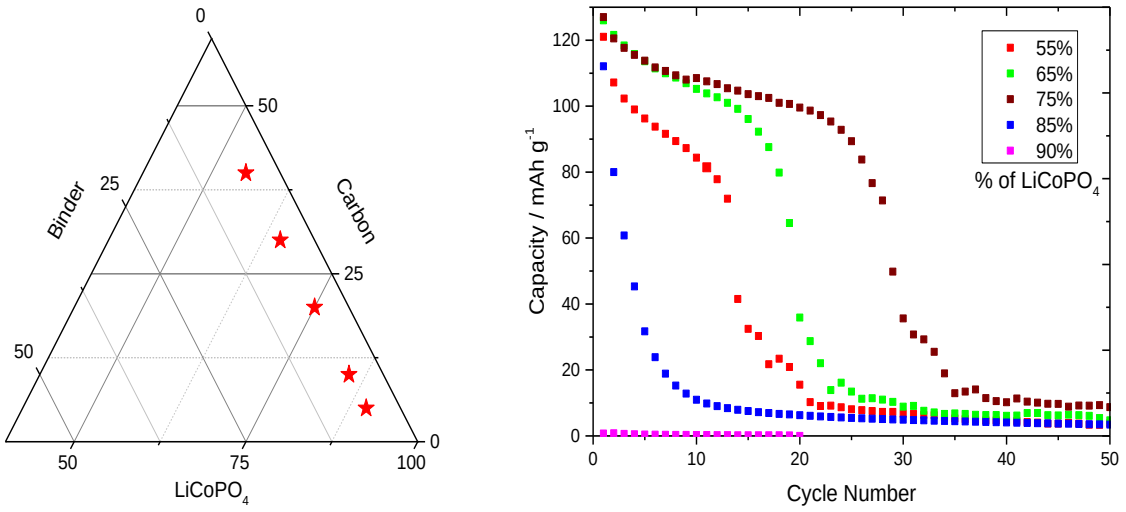

Figure 4.23 - Ternary plot showing the different electrode compositions that were made, with the results shown. The % amount corresponds to $LiCoPO_4$, with all cells at 5 - 3.5 V *vs.* Li/Li^+ at 0.1 C using BASF LP57 1 M $LiPF_6$ EC:EMC (3:7).

The results suggest that 75 % active material within the composite pellet provided the highest discharge capacity on the initial cycle as well as the best cycle life. The formulation of the composite electrode was found to significantly influence the cycle life

performance, and that a minimum amount of carbon is a necessity (at least 10 %) for the electrode to be electrochemically active.

A value of 55 % $LiCoPO_4$ by mass within the electrode produced similar cycling results, with the degradation of the half-cells following the same distinct pattern. Between 15-30 cycles, the discharge capacity drops off rapidly for each electrode composition above 55 % $LiCoPO_4$. A trade-off between the surface area and the conductivity of the electrode may explain the cycling results, with a large surface area resulting in a higher resistance due to the increased electrolyte breakdown on the particle surface. The results suggest that there is an optimum level of carbon that needs to be in the pellet to achieve the best performance. However if there is not enough carbon present, the conductivity across the bulk of the electrode is poor and the loss of contact between the particles results in rapid capacity fade.

Figure 4.24 shows the BET (Brunauer-Emmett-Teller) results from the different composite electrodes. The surface area increased as more carbon was present, which supports the conclusions drawn relating the different performances in cycle life to the surface area.

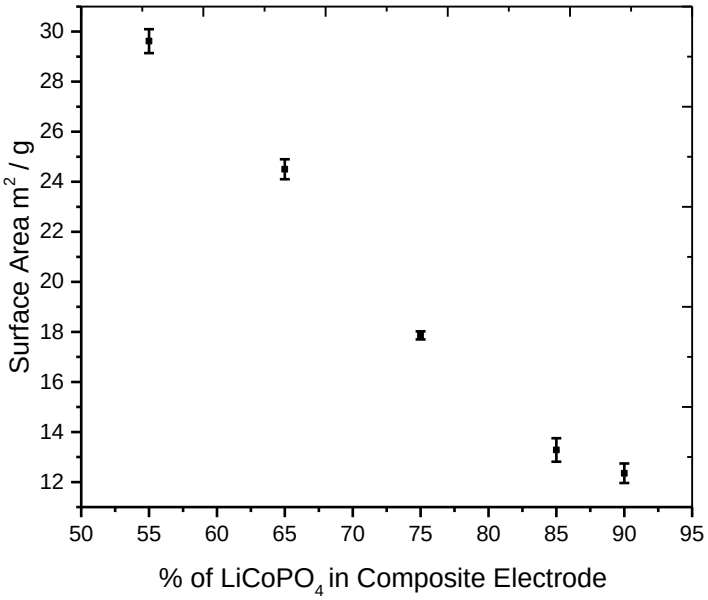

Figure 4.24 - BET results from the different $LiCoPO_4$ composite electrodes.

4.8 Particle Coating

Introducing an artificial physical conducting barrier between the electrochemically active particles and the electrolyte is a common strategy used within battery research. The role of a surface coating could be to increase the intra-particle conductivity, as well as minimise capacity losses by preventing side reactions occurring on the particle surface.

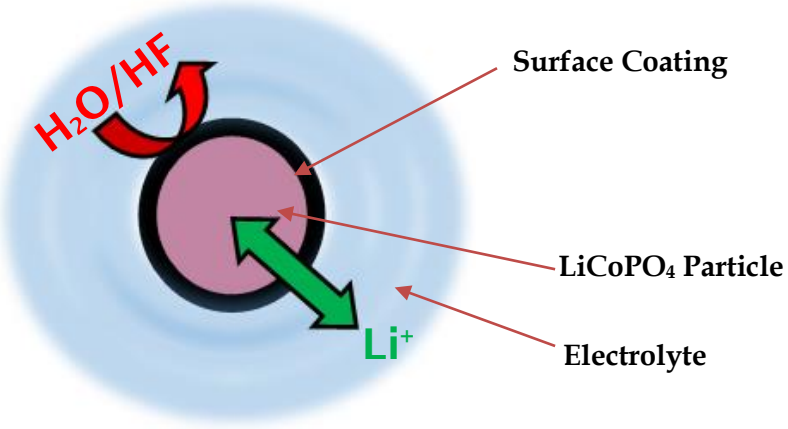

Figure 4.25 - The possible effect of surface coatings on a $LiCoPO_4$ coated particle.

By utilising thin surface coatings, the $LiCoPO_4$ particles are effectively isolated from the electrolyte, whilst still facilitating the solid state diffusion of lithium ions through the coating barrier, allowing the insertion/extraction to proceed as normal. An inactive, impermeable coating would protect the particles from any acidic species in the electrolyte such as hydrogen fluoride (HF), formed due to the hydrolysis of hexafluorophosphate anions (PF_6^-) by traces amounts of water present in the electrolyte.

Surface coatings have been successful in improving the electrochemical performance of many lithium-ion cathode materials, and are widely acknowledged as a method to improve thermal stability, rate capability and capacity retention of electrodes. There are a wide range of coating materials previously investigated including metal oxides,[9] metal phosphates,[10] metal hydroxides,[11] metal carbonates,[12] and metal fluorides[13] which have all shown to increase the cycle life of several cathode materials.

Generally, to coat the particles, mechanical mixing of the coating precursors and the active material is required. A heat treatment at elevated temperatures then breaks down the precursor, and a rough coating of the product over the particles is produced. Within

this method, some areas of the bulk material will be heavily coated compared to others. Excess coating can lead to low rate capabilities and a reduction in capacity, due to blocking effects of lithium intercalation.

4.8.1 Carbon Coatings

The use of carbon to coat the particle surface of many cathode materials has many benefits. Using carbon improves the electronic conductivity of many electrode materials, which reduces the resistance and ohmic drop at elevated current densities. In cases where the electronic conductivity of the bulk is lower than the ionic conductivity, ambipolar diffusion can only proceed at an area of point contact between the active material, conducting additive and electrolyte. Carbon coating would increase the contact network between the particles across the bulk, which can improve the electron pathway while remaining permeable to lithium ions.

Different carbon coated loadings on the $LiCoPO_4$ particles was explored by thermal decomposition of glucose. Thermogravimetric analysis (TGA) is a method of thermal analysis in which changes in physical or chemical properties can be measured as a function of increasing temperature. This technique allowed for the conversion percentage of glucose into carbon, so that a range of different percentage loading could be applied to the $LiCoPO_4$ particles. **Figure 4.26** displays the TGA results from the thermal decomposition of glucose, which as a percentage by mass is an 18% conversion rate of glucose into carbon.

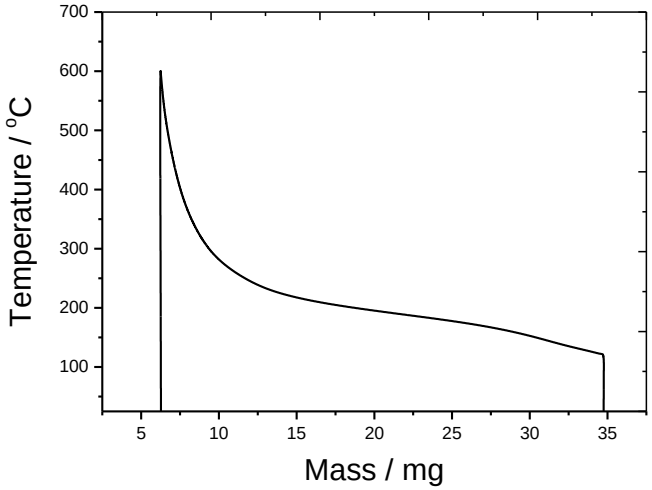

Figure 4.26 - TGA results from the thermal decomposition of glucose from 25 °C to 600 °C.

The $LiCoPO_4$ powder was manually ground in a pestle and mortar with glucose to obtain a uniform mix. The mixture was then transferred to a crucible and heated to 600 °C for 3 hours under argon.

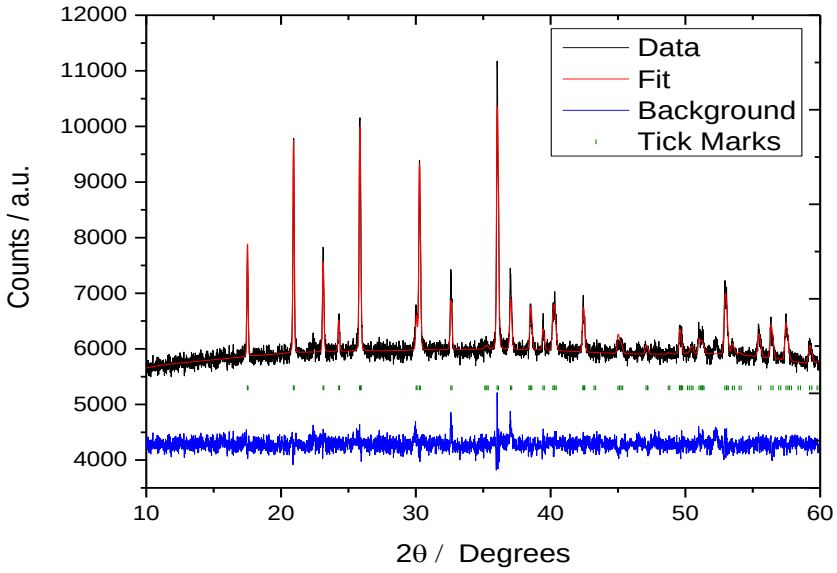

Figure 4.27 - X-ray diffractiogram of 5 % carbon coated $LiCoPO_4$ refined against data from the ICSD database.[1] Lattice constants: a = 10.20542(1), b = 5.92822(4) and c = 4.70177(7), α = β = γ = 90°, wRp 1.59 % Rp 1.23 %.

Figure 4.28 shows cycling data from different carbon coating particle loadings under the same conditions at 0.1 C.

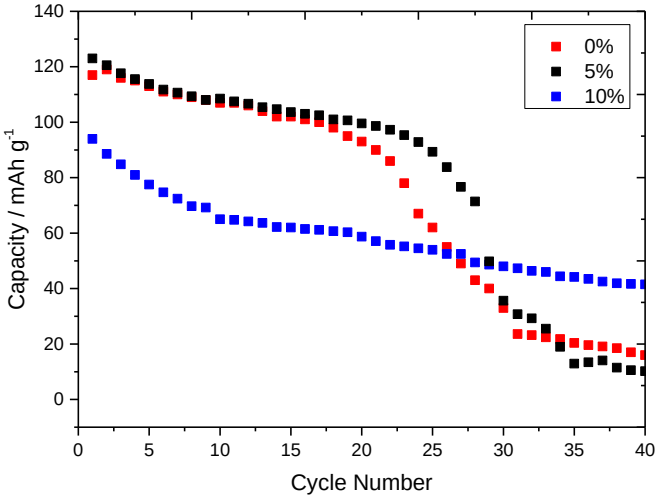

Figure 4.28 - Cycle life performance of $LiCoPO_4$ at different percentages of carbon coated loading conducted in a lithium half-cell at 0.1 C with BASF LP57 1 M $LiPF_6$ EC:EMC (3:7) electrolyte.

The results suggest that carbon coating may improve the cycling performance. Initial cycling has a slight improvement in terms of capacity retention on discharge, and the cycling behaviour has been slightly improved. A 10 % carbon coat layer reduces the

discharge capacity values obtained, suggesting that the carbon coated later is too thick, and that the coating layer may actually be blocking lithium intercalation. The cycle life however is relatively stable; this could be because the particles do not have as much volume expansion as less lithium is intercalated, and also the layer may protect against particle corrosion caused by HF.

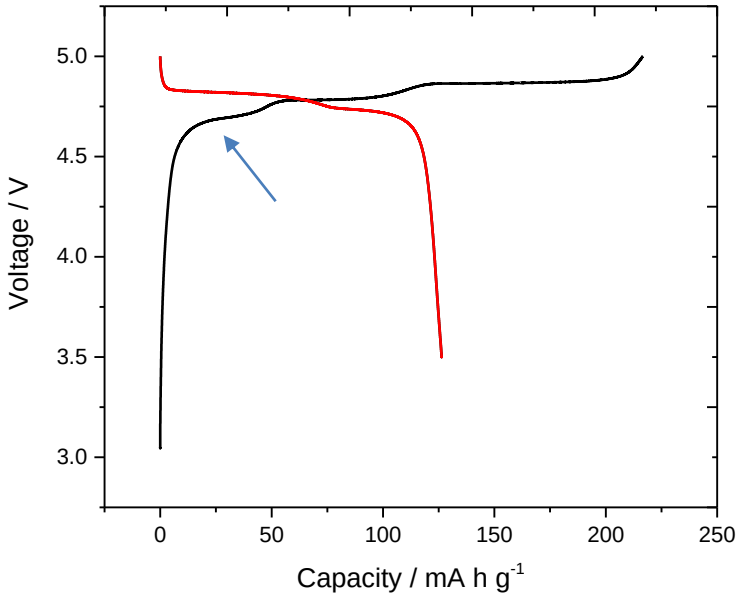

Figure 4.29 - The first cycle of 5 % carbon coated $LiCoPO_4$ conducted in a lithium half-cell with BASF LP57 1 M $LiPF_6$ EC:EMC (3:7) electrolyte.

Figure 4.29 displays galvanostatic cycling of 5 % carbon coated $LiCoPO_4$ at 0.1 C. The highlighted region (blue arrow) shows an additional plateau that is not present when the sample is not carbon coated. This would suggest that the carbon surface layer is being oxidised upon the first cycle, and that a very thin layer of carbon has been coated onto the surface of the particles in order to observe this plateau. This side reaction is not observed on the reverse cycle or any subsequent cycles and adds additional capacity of ~50 mA h g^{-1} on the first cycle.

The dQ/dE plot in **Figure 4.30** shows the additional side reaction from the carbon coating at ~4.65 V. The other asymmetric peaks can be associated to the reversible lithium intercalation process as described previously.

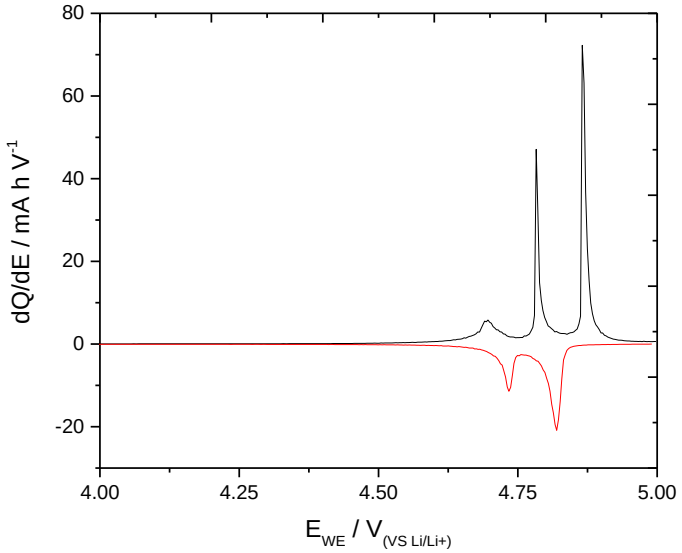

Figure 4.30 – A dQ/dE plot of the $LiCoPO_4$ 5 % carbon coated composite electrode conducted in a lithium half-cell with BASF LP57 1 M $LiPF_6$ EC:EMC (3:7) electrolyte.

Figure 4.31 displays the second cycle, showing that the initial side reaction is not seen, and only the electroactive regions of lithium intercalation of $LiCoPO_4$ are observed.

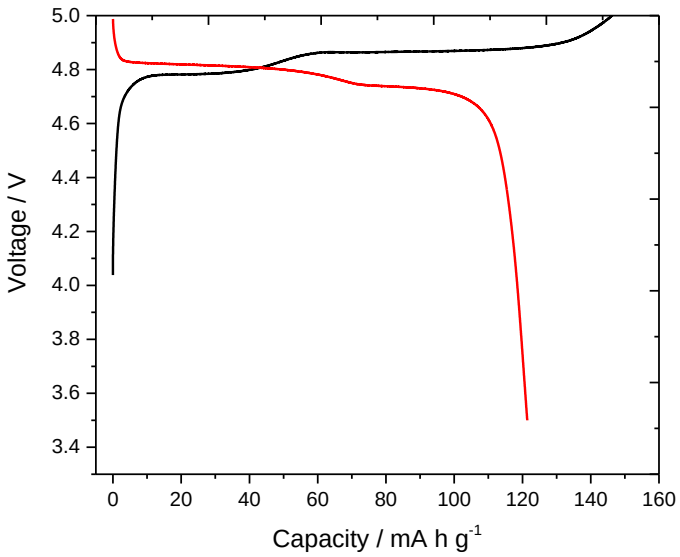

Figure 4.31 – Second cycle of the $LiCoPO_4$ 5 % carbon coated composite electrode conducted in a lithium half-cell with BASF LP57 1 M $LiPF_6$ EC:EMC (3:7) electrolyte.

Carbon coating the material appears to have minimal effect on the cell performance in terms of capacity retention, with similar discharge capacities reported for the uncoated material.

4.8.2 RuO_2 Coating

Moving away from carbon, rutile oxide (RuO_2) was also considered as a particle coating due to its high electrochemical stability. A 5 % RuO_2 coating was applied to the $LiCoPO_4$ particles under the same conditions as for the carbon coat, but using ruthenium chloride hydrate (Sigma Aldrich 99.98 %) as the substrate (instead of glucose). **Figure 4.32** shows the XRD pattern that was refined, RuO_2 was also included in the refinement.

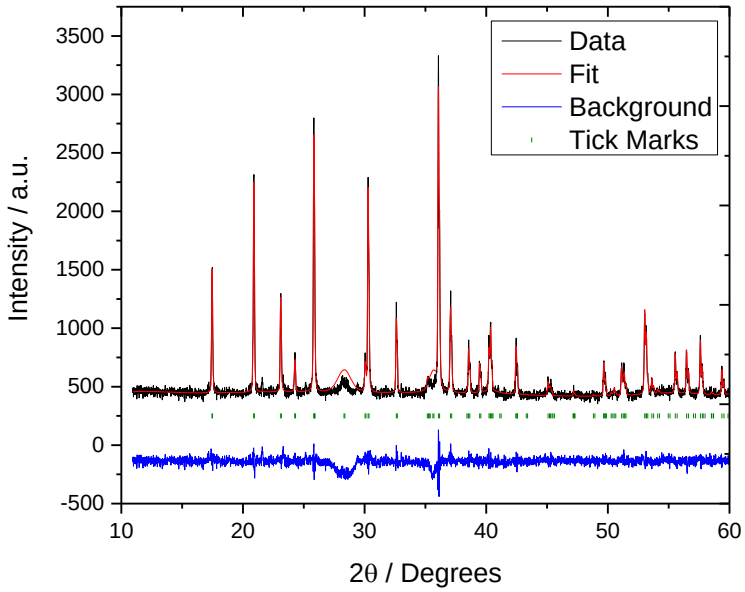

Figure 4.32 - X-ray diffractiogram of 5 % RuO_2 coated $LiCoPO_4$ refined against data from the ICSD database.[1,14] Lattice constants: a = 10.16681(0), b = 5.90241(4) and c = 4.68641(3), α = β = γ = 90°, wRp 6.84 % Rp 4.94 %.

Figure 4.33 displays the first cycle under the same conditions for the 5 % RuO_2 coated $LiCoPO_4$ (at 0.1 C using BASF LP57). The additional capacity that was obtained on the initial charge of the carbon coated material is not present, which further suggests the extra irreversible capacity is due to the carbon coating. A similar voltage profile is seen on charge and discharge, and the different phase transition regions are observed. The discharge capacity obtained on the first cycle is 135 mA h g^{-1}, giving 81 % of the theoretical discharge.

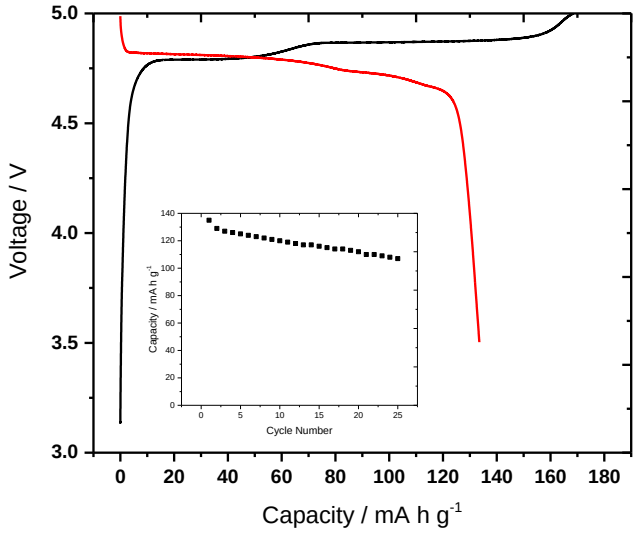

Figure 4.33 –a) Initial cycle of $LiCoPO_4$ 5 % RuO_2 coated composite electrode b) cycling results conducted in a lithium half-cell at 0.1 C with BASF LP57 1 M $LiPF_6$ EC:EMC (3:7) electrolyte.

The cycle life was also relatively stable compared to the other $LiCoPO_4$ composite electrodes. No data was recorded after 25 cycles due to a power cut, so it is unknown as to whether the composite electrode will degrade rapidly as shown previously for the uncoated $LiCoPO_4$ composite electrodes.

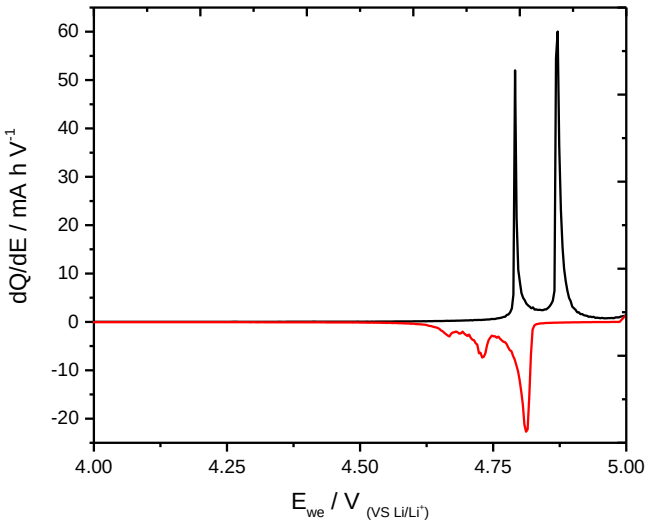

Figure 4.34 – A dQ/dE plot of the 5 % RuO_2 coated $LiCoPO_4$ composite electrode conducted in a lithium half-cell with BASF LP57 1 M $LiPF_6$ EC:EMC (3:7) electrolyte.

The dQ/dE plot in **Figure 4.34** shows typical asymmetric peaks can be associated to the reversible lithium intercalation process. A very small irreversible peak on discharge can be observed, which maybe due to the presence of RuO_2.

4.9 Rate Testing

Rate testing is a method used to assess the effect of applied current density on the charge/discharge performance at different timescales. The cells were charged at 0.1 C and discharged at a range of different rates. **Figure 4.35** shows the results from uncoated $LiCoPO_4$ and a 5 % coating of either carbon or RuO_2 on the $LiCoPO_4$ particle surface at various different C-rates. The charging rate was fixed at 0.1 C and the different discharge rates were repeated for three cycles.

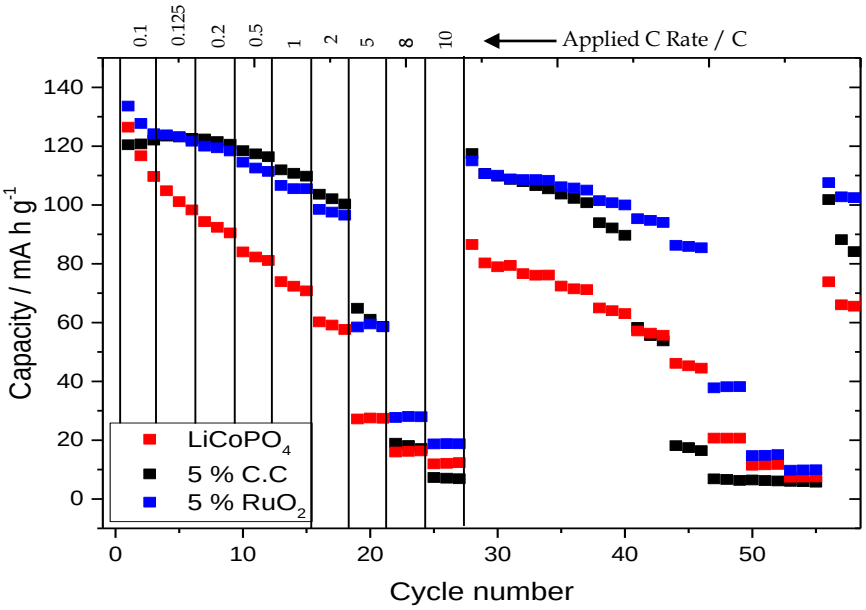

Figure 4.35 - Discharge capacities of coated and uncoated $LiCoPO_4$ charged at 0.1 C and discharged at various C-rates. Rate testing was conducted in a lithium half-cell with BASF LP57 1 M $LiPF_6$ EC:EMC (3:7) electrolyte.

The coated and uncoated $LiCoPO_4$ could reach ~50 % of its practical capacities at 2 C (30 minutes charge/discharge) on the initial cycle. The uncoated material did not perform as well as the coated material, especially at faster rates and on the second set of rate testing cycling. Overall, coating the particles with RuO_2 appears to enhance the rate testing capabilities the most, although the carbon coating did produce a similar positive result.

Within each test material, increasing the C-rate results in smaller discharge capacities. The reduction in capacity at these higher rates will be due to limitations in the rate of solid state diffusion of lithium within the active material, polarisation of the electrodes and lack of compensation in the voltage cut off to compensate for the potential drop due to the increasing current.

As the rate of discharged is increase there is a decrease in the potential of discharge of the cell. Much of this potential decrease can be attributed to IR drop, as a result of the increased current passed through the cell which effectively has a fixed resistance for a given degree of charge. As the current density of the discharge is increased, the discharge profiles become more sloping. This effect could be due to polarisation of the electrodes at larger current densities impacting the measured potential of the cell. **Figure 4.36** shows the discharge profiles at the initial repeat of each C-rate for the 5 % carbon coated $LiCoPO_4$.

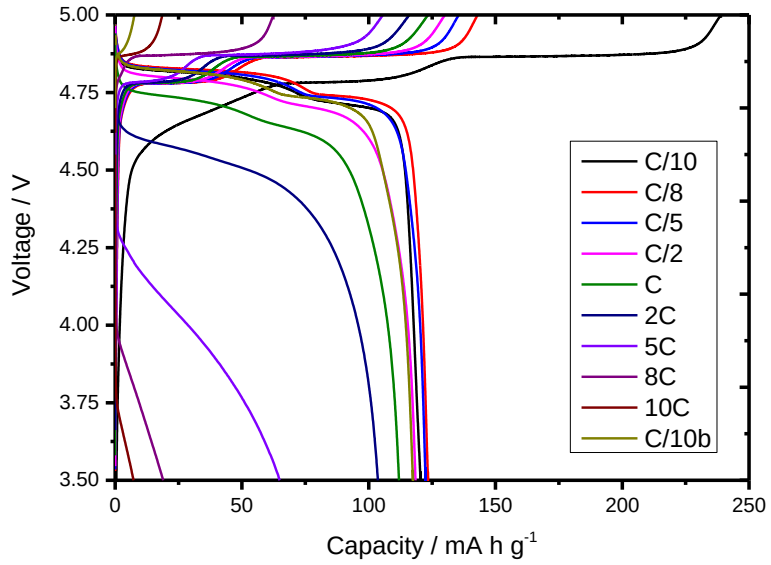

Figure 4.36 - Discharge profiles of 5 % carbon coated $LiCoPO_4$, charged at 0.1 C. Rate testing was conducted in a lithium half-cell with BASF LP57 1 M $LiPF_6$ EC:EMC (3:7) electrolyte.

The effect of the rate of discharge on capacity is more easily visualised in **Figure 4.37** which is data collected from the 5 % RuO_2 of $LiCoPO_4$. Increasing the current density from a rate corresponding to 0.1 C to a rate of 1 C does not have a large impact on the discharge capacity. At a rate of 1 C, the material still produces a discharge capacity of 107 mA h g^{-1} down from 134 mA h g^{-1} produced at 0.1 C.

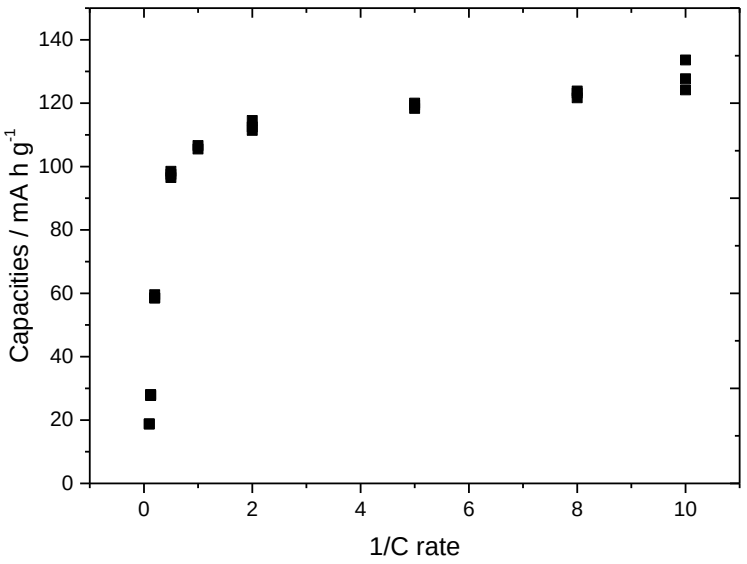

Figure 4.37 - Discharge capacity of 5 % RuO_2 coated $LiCoPO_4$. Rate testing was conducted in a lithium half-cell with BASF LP57 1 M $LiPF_6$ EC:EMC (3:7) electrolyte.

As the current density is increased beyond the rate of 1 C, the discharge capacity begins to decrease exponentially. The reduction of discharge capacity at these high rates will be due to limitations from the rate of solid state diffusion in the active material, polarisation of the electrodes and lack of compensation in the voltage cut off to compensate from the potential drop due to the increasing current.

4.10 References

1 P. A, J. Pizarro, A. Goni, T. Rojo and M. Arriortua, 1998, An. Quim., **94**, 383–387.

2 M. K. Devaraju and I. Honma, Adv. Energy Mater., 2012, 2, 284–297.

3 F. Zhou, P. Zhu, X. Fu, R. Chen, R. Sun and C. Wong, CrystEngComm, 2014, **16**, 766.

4 J. Wolfenstine, U. Lee, B. Poese and J. L. Allen, J. Power Sources, 2005, **144**, 226–230.

5 J. Yang, H. Liu, W. N. Martens and R. L. Frost, J. Phys. Chem. C, 2010, **114**, 111–119.

6 A. Rajalakshmi, V. D. Nithya, K. Karthikeyan, C. Sanjeeviraja, Y. S. Lee and R. Kalai Selvan, J. Sol-Gel Sci. Technol., 2013, **65**, 399–410.

7 E. Nanini-Maury, J. Świątowska, A. Chagnes, S. Zanna, P. Tran-Van, P. Marcus and M. Cassir, Electrochim. Acta, 2014, **115**, 223–233.

8 X. Qi, B. Blizanac, A. DuPasquier, P. Meister, T. Placke, M. Oljaca, J. Li and M. Winter, Phys. Chem. Chem. Phys., 2014, **16**, 25306–25313.

9 Z. Chen and J. R. Dahn, Electrochem. Solid-State Lett., 2003, **6**, A221.

10 A. T. Appapillai, A. N. Mansour, J. Cho and Y. Shao-Horn, Chem. Mater., 2007, **19**, 5748–5757.

11 S. B. Jang, S.-H. Kang, K. Amine, Y. C. Bae and Y.-K. Sun, Electrochim. Acta, 2005, **50**, 4168–4173.

12 J. Zhang, Y. . Xiang, Y. Yu, S. Xie, G. . Jiang and C. . Chen, J. Power Sources, 2004, **132**, 187–194.

13 Y. Sun, J. Han, S. Myung, S. Lee and K. Amine, Electrochem. commun., 2006, **8**, 821–826.

14 C.-E. Boman, J. Danielsen, A. Haaland, B. Jerslev, C. E. Schäffer, E. Sunde and N. A. Sørensen, Acta Chem. Scand., 1970, **24**, 116–122.

Chapter 5:

Influence of Electrolyte and Metal Doping on the $LiCoPO_4$ System

5.1 Introduction

Within the previous chapter, optimisation and detailed analysis of the best performing $LiCoPO_4$ electrode. This chapter looks at different electrolyte formulations, and how they affect the cell performance of the best performing electrode. A wide range of different electrolytes were made up in house and incorporated into Swagelok cells. Improvements in the electrochemical performance have been reported due to the formation of improved passivation layers at the surface of the active material particles. To dope manganese into $LiCoPO_4$ a manganese metal salt was used, creating a wide range series of composition $LiCo_{1-x}Mn_xPO_4$.

5.2 The Role of the Electrolyte in High Voltage Systems

5.2.1 Introduction

The practical application of high-voltage lithium-ion batteries remain a challenge, and the role of the electrolyte has the most important impact on the battery systems due to the degradation of electrolytes at high voltages. Several approaches have been explored to develop appropriate electrolyte systems to mitigate the undesirable oxidative decomposition that occurs.

Tris(trimethylsilyl) phosphite (TMSP) is an organophosphorus compound which has been used in high voltage $LiNi_{0.5}Mn_{1.5}O_4$ cathodes as an addictive within electrolytes which gave superior electrochemical cycling. Studies suggest that TMSP eliminates HF after hydrolysis of $LiPF_6$ has occurred and forms a protective layer on the cathode surface to limit severe electrolyte decomposition[1]. **Figure 5.1** suggests a possible mechanisms for the electrochemical oxidative decomposition of TMSP and how this would scavenge HF from the electrolyte.[2]

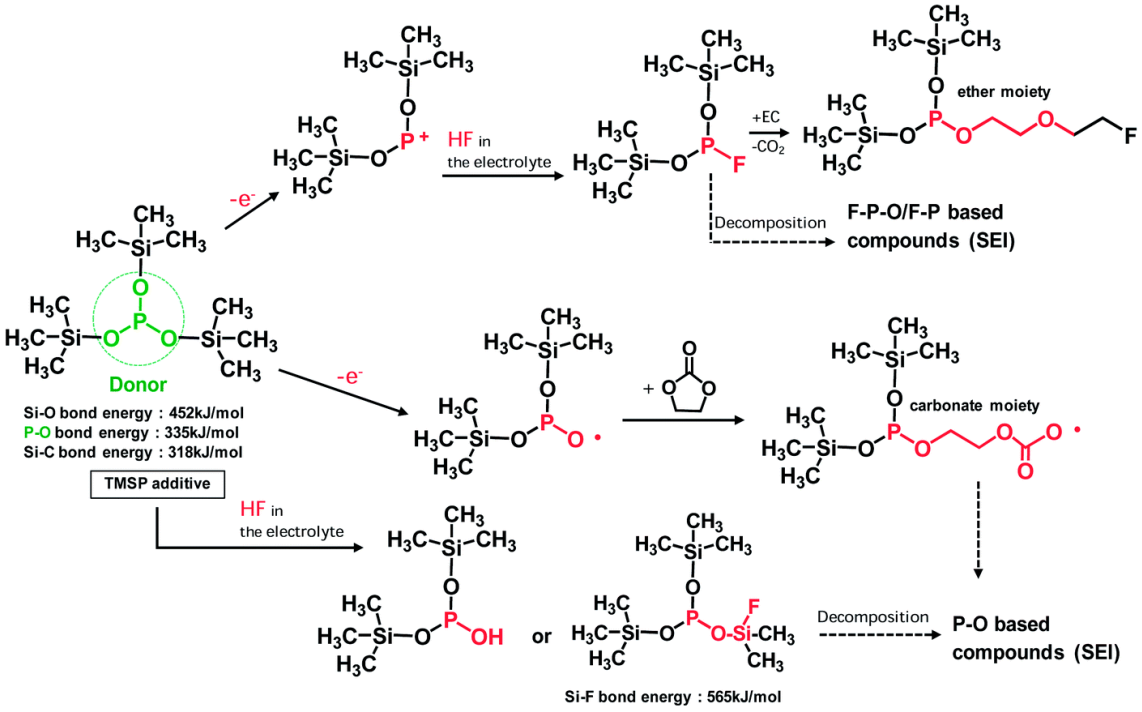

Figure 5.1 - Proposed mechanisms for the electrochemical oxidative decomposition of TMSP. Reproduced with permission from reference.[2]

Another approach to improving high voltage electrolyte stability is use LiBob as a metal salt. LiBob has been used as either the primary salt for lithium-ion battery electrolytes or more commonly utilised on the additive level as a protective film can be produced on the surface of the particles. The structure of LiBob does not have a labile fluorine bond present, therefore no HF can be produced.

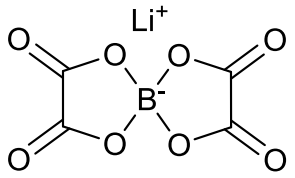

Figure 5.2 - Structure of the electrolyte salt LiBob

In particular, recent studies have reported that using LiBob as an additive improved the performance of $LiNi_{0.5}Mn_{1.5}O_4$ lithium half cells.[3]

Another lithium metal salt, $LiBF_4$ has attracted attention for high power lithium-ion batteries due to its higher conductivity and smaller charge transfer resistance compared to $LiPF_6$.[4,5] However, the salt had been rarely used in recent years because of its electrochemical instability and weak capability of forming a stable SEI layer.[6]

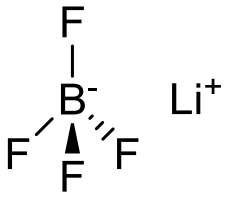

Figure 5.3 - Structure of the electrolyte salt $LiBF_4$.

Fluoroethylene carbonate (FEC) is an electrolyte addictive that has shown improved performance on the negative electrode, most noticeable in silicon based electrodes. FEC has been reported to undergo polymerisation at the surface of silicon particles, the polymerisation process has been suggested to be responsible for the production of a thin SEI layer capable of withstanding the volume changes in silicon and allowing for improved passivation of the electrode during cycling and improved performance.[7,8,9]

FEC has also been recently shown to improve cycling in $LiCoPO_4$ lithium half-cells compared with that of standard EC-based electrodes. The improvement does not come

from lowering the HF content, but rather the formation of a protective surface film on the $LiCoPO_4$ particles.[10]

5.2.2 Cycled Composite Electrodes

Figure 5.4 displays an SEM image of a composite electrode with the $LiCoPO_4$ particles surround carbon agglomerates (left). The carbon has good contact with the $LiCoPO_4$ particle shown, which would increase the particles intra-conductivity.

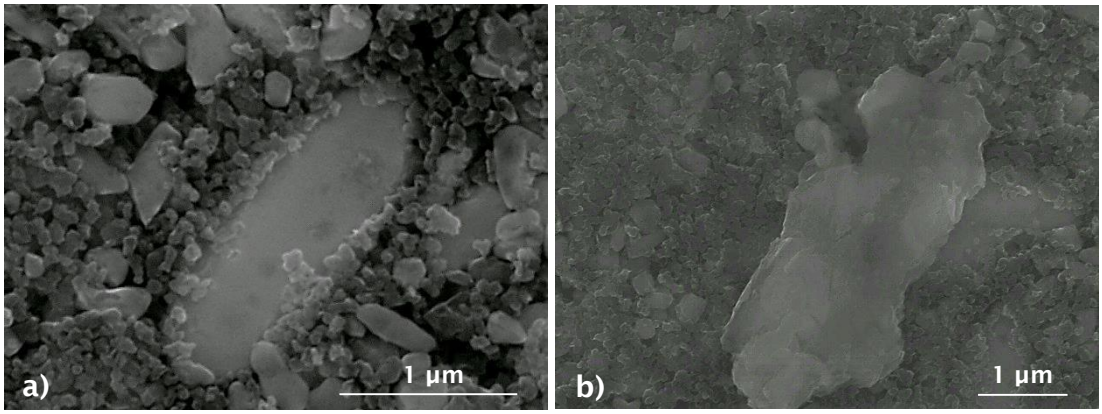

Figure 5.4 – SEM image of a) Pristine composite electrode b) Composite electrode after 10 cycles.

The SEM image on the right shows the same composite electrode after 10 cycles at 0.1 C using BASF LP57 electrolyte. The particle shows high levels of corrosion on the particle surface, which could be due to the HF present. The particles would have undergone expansion and contraction as lithium is removed and re-inserted into the particle, which could also lead to particle deformation. There may be evidence of an SEI layer on the carbon particles, as the carbon particles on b) are not as well defined.

The composite electrode was removed from the cell inside a glovebox, and washed with the solvent EMC. The electrode was then placed on carbon tape and stored in a glove bag during transportation to the SEM instrument. The glove bag was then wrapped around the SEM instruments inlet, and the sample was placed inside the chamber and evacuated as soon as possible to ensure minimal oxidation on the surface of the electrode could occur.

5.3 The Effect of Electrolyte on the $LiCoPO_4$ System

Different electrolyte formulations were made up in-house and incorporated into 5 % carbon coated $LiCoPO_4$ half cells and tested under the same conditions at 0.1 C. The different formulations of each electrolyte had a large impact on the cell performance.

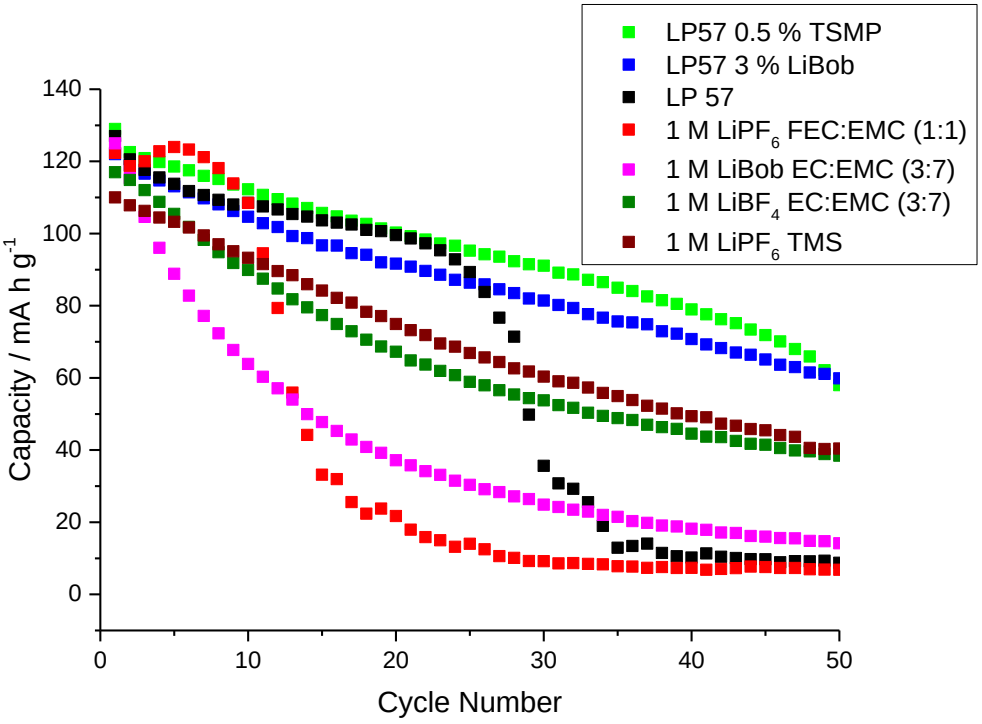

Figure 5.5 – Cycling of $LiCoPO_4$ 5 % carbon coated composite electrodes at 0.1 C using various electrolyte formulations.

LP57

This electrolyte was obtained from BASF directly and was used in obtaining the majority of results in the previous chapters. The cycling results and analysis from this electrolyte has been previously discussed in **Section 4.5**.

LP57 with 0.5 % TMSP

The addition of tris (trimethylsilyl) phosphate (TMSP) at a weight percent of 0.5 % gave the best cycling performance and the highest discharge capacities. This addictive has been used to form a protective film that stabilises the surface of the charged cathode, for reversible Li^+ intercalation in the coveted 5 V region.[11] It is known that the TMSP addictive reacts directly with HF molecules in the electrolyte, which would also help minimise side reactions within the cell.[12]

LP57 with 3 % LiBob

The inclusion of lithium bis(oxlate)borate (LiBob) has been reported to form stable and robust semi-carbonate type SEI layer which is expected to provide necessary protection for the $LiCoPO_4$ particles from the nucleophilic attack of F^- ions from the HF present.[13]

1M $LiPF_6$ FEC:EMC (1:1)

Many studies have been conducted on the effects of FEC on battery performance. It has been reported that adding FEC was beneficial to the formation of desirable SEI layer on the anode, although the decomposition method remains unclear[14]. The use of FEC within this work had a negative impact on the cell cycling. The increased cycling over the first few cycles suggest a protective film was formed, but then the cycling fades rapidly which was surprising. Aurbach *et al.* added 2000 ppm of water to both an EC and FEC based electrolyte under argon, and found that the water reacts faster with $LiPF_6$ and produces more HF in the FEC-based electrolyte solution.[10] It can be assumed that the electrolyte formulation was wet, which is why the capacity faded so readily.

$LiPF_6$ TMS

Sulfone-based electrolytes are of interest in high voltage electrochemistry due to their high electrochemical stability,[15] however they do not form a stable SEI layer on the graphite surface.[16] Tetramethylene sulfone has a low melting point of 27.5 °C and has a high viscosity, which may explain the poor discharge capacity achieved.

Use of LiBob and $LiBF_4$ as electrolyte salts

The labile P-F bonds in $LiPF_6$ are highly reactive towards trace amounts of water within the electrolyte solution. The salt would undergo a hydrolysis reaction which produces HF. Different electrolyte salts were tested in an attempt to move away from the $LiPF_6$ salt, however the discharge capacities obtained were less. LiBob appears to be less stable than $LiPF_6$ at high voltages, which is why using the salt as an addictive was more successful as a thin film of electrolyte breakdown products would be formed initially.

5.3.1 Initial Cycle of Different Electrolytes on the $LiCoPO_4$ System

LP57 with 0.5 % TMSP

The addition of 0.5% TMSP by weight into the LP57 batch improved the cyclability, allowing for ~50% of the discharge capacity to still be obtained after 50 cycles. The initial cycle voltage plateau is very similar to the cycle with no addictive's within the electrolyte, which was described in the previous chapter.

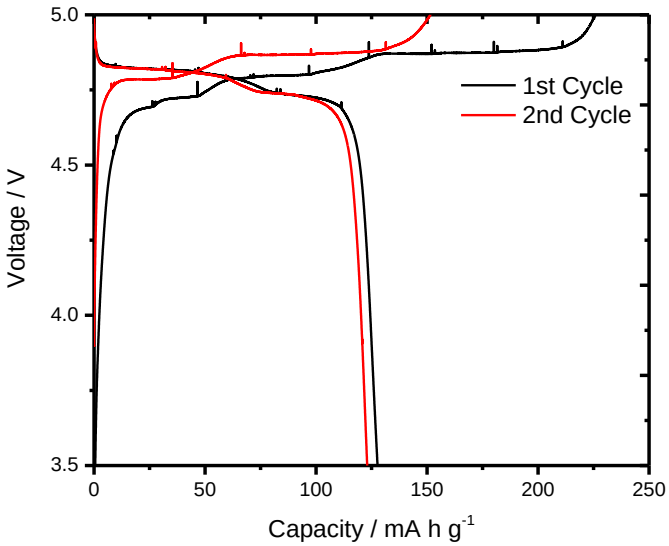

Figure 5.6 - Initial cycle of $LiCoPO_4$ 5 % carbon coated composite electrode at 0.1 C using BASF LP57 with 0.5 % TMSP as the electrolyte.

1 M $LiBF_4$ EC:EMC (3:7)

The initial cycle when using $LiBF_4$ EC:EMC (3:7) as the electrolyte had irreversible oxidation processes occurring above ~ 4.25 V. The processes can be related to the oxidation of the electrolyte and formation of the SEI layer, which can contribute to the large noticeable amount of extra capacity obtained on the initial charge. On the second cycle (and onwards), the system has stabilised, with only the typical voltage plateaus seen from the lithium intercalation of the active material on charge and discharge.

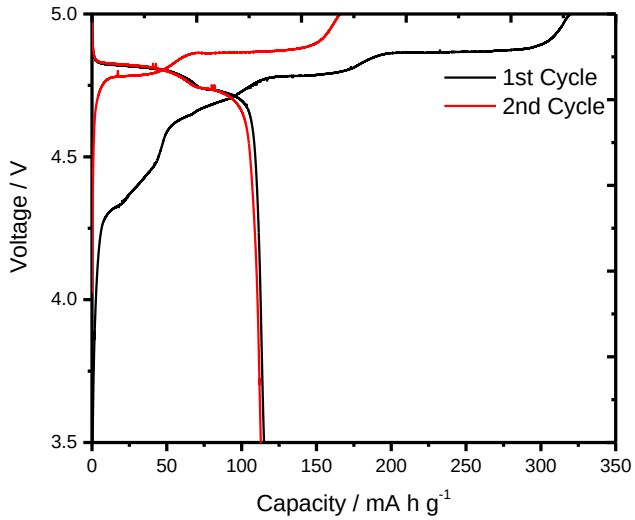

Figure 5.7 - Initial cycle of $LiCoPO_4$ 5 % carbon coated composite electrode at 0.1 C using 1 M $LiBF_4$ EC:EMC (3:7) as the electrolyte.

1 M $LiPF_6$ TMS

The initial cycle from using $LiPF_6$ with TMS did not have the defined typical voltage plateaus that are associated with $LiCoPO_4$ intercalation. The initial irreversible processes are not present after the first cycle, with a similar discharge capacity retained. On the second cycle, the amount of capacity recovered upon charge is less than expected, which could be due to the relatively high viscosity of the electrolyte which may limit the lithium ions solvation ability.

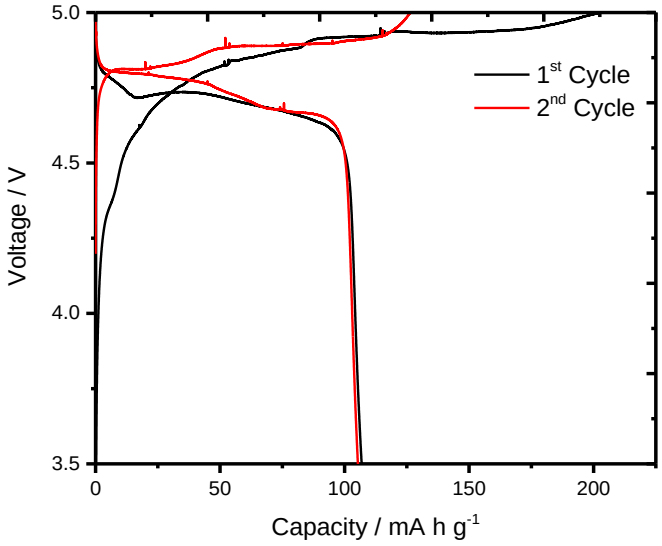

Figure 5.8 - Initial cycle of $LiCoPO_4$ 5 % carbon coated composite electrode at 0.1 C using 1 M $LiPF_6$ TMS as the electrolyte.

1 M LiBob EC:EMC (3:7)

There is a relatively large discharge capacity loss between the first and second cycle when using 1 M LiBob as the electrolyte salt. The initial voltage profile is slightly masked with other irreversible processes occurring during the initial charge step, and the amount of capacity recovered on charge on the second cycle is low. This is a similar result to using TMS as the solvent. LiBob does oxidise at over 4.5 V, which may explain the poor cyclability that was observed. Published data has shown that using LiBob as an addictive does improve the cycle life of high voltage systems, as the borate oxalates that are produced from the initial oxidation form a thin passivation film which inhibits further oxidation of the electrolyte.[17] When used as an addictive in combination with the BASF LP57, improved cycling was observed.

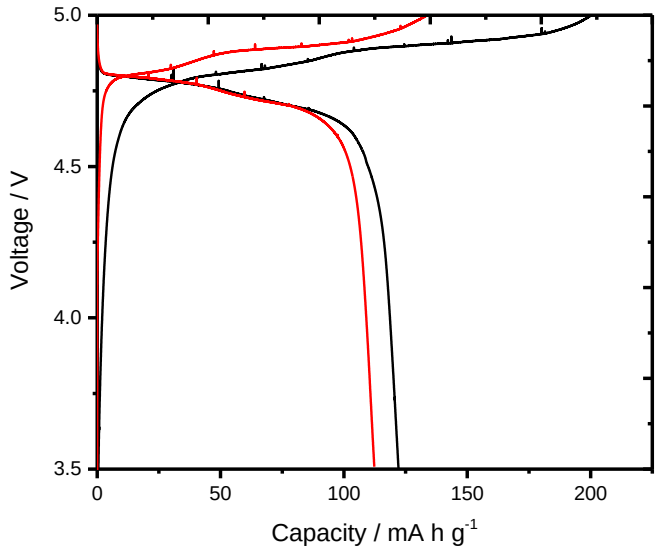

Figure 5.9 - Initial cycle of $LiCoPO_4$ 5 % carbon coated composite electrode at 0.1 C using LiBob EC:EMC (3:7) as the electrolyte.

5.4 Differential Electrochemical Mass Spectrometry

To measure if any gaseous products were being released during battery cycling, a cell was connected to a Differential Electrochemical Mass Spectrometry (DEMS) instrument and argon was passed through the cell.

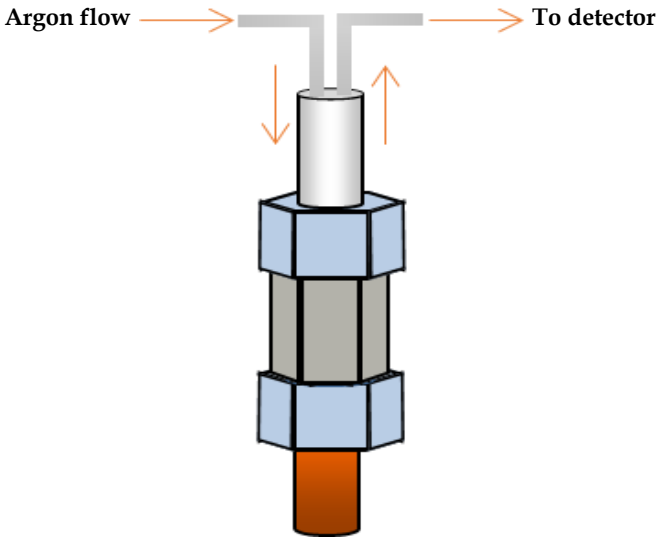

Figure 7.2 – Illustration of altered Swagelok cell that was attached to the DEMS instrument.

A flow meter was used to set the amount of flowing argon to 1 mL min^{-1}. The current collector had holes drilled into it to allow for any gaseous products to flow out of the current collector and into the spacious surround where argon is flowing. Any gaseous products detected could then be detected coherently with the charge/discharge galvanostatic data.

The cell was charged and discharged at 0.1 C using BASF LP57 electrolyte. The results show that on during each charge, CO_2 gas was evolved which is due to the electrolyte being consumed through an oxidative process on the surface of the electrode.

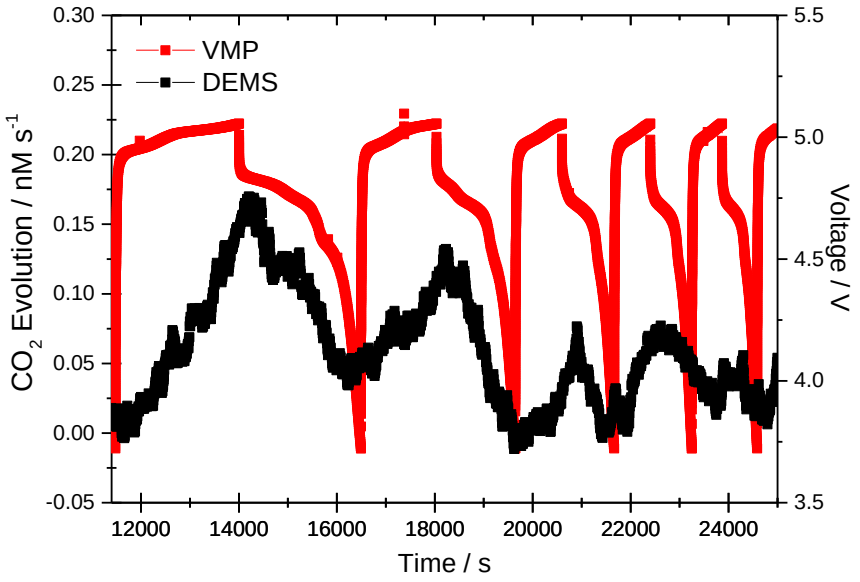

Figure 7.3 - DEMS results from a $LiCoPO_4$ 5 % carbon coated composite electrode using BASF LP57 electrolyte. The black line traces the CO_2 levels inside the cell, and the red line is the galvanostatic charge and discharge data.

5.5 The Effect of Doping on the $LiCoPO_4$ System

5.5.1 Background

A widely adopted method of improving the stability and cycle life performance of a number of lithium insertion materials is to introduce heteroatoms into the electrode materials. Doping of electrode materials via low concentration levels of metal ions to either replace the lithium or the host metal centre can influence the structure and the electronic state of the electrode material. The specific effects of doping are dependent on the heteroatoms introduced; it is important to maintain the iso-structural electrodes ability to reversible intercalate lithium ions.

In this study, the series of manganese doped samples were synthesised, with the aim of reducing the overall active voltage window and increase the capacity retention of the cathode material. A wide range of different compositions of $LiMn_1Co_{1-x}PO_4$ were made and the electrochemical performance was analysed.

5.5.2 $LiCo_{1-x}Mn_xPO_4$ Synthesis

To introduce manganese into the olivine structure, manganese sulphate was used as the metal salt within the synthesis method as described in **Section 4.2**, as well as coating the particles with a 5 % carbon coating layer. In a typical route, 0.01 mol of H_3PO_4 (85 % Sigma Aldrich) and 0.03 mol of LiOH (Sigma Aldrich) were mixed first in 40 ml of the DEG-H_2O mixed solvent (6:1) with strong magnetic stirring for 20 minutes. The appropriate amounts of $CoSO_4 \cdot 7H_2O$ (Sigma Aldrich) and $MnSO_4 \cdot H_2O$ to achieve the correct composition was pre-dissolved in 20 ml of the DEG-H_2O mixed solvent and added slowly. The solution was stirred for another 20 minutes and then transferred to an autoclave and heated at 180 °C for 10 hours and allowed to cool naturally. The resulting solution was filtered, and washed through with ethanol and water subsequently three times via centrifugation. The centrifuge was set at 8500 rpm and was spun for 5 minutes. The powder was then ground using a pestle and mortar nwith glucose to obtain a 5 % carbon coat by mass, before being heated for a second time at 600 °C under argon. The powder was then allowed to cool naturally.

5.5.3 $LiCo_{1-x}Mn_xPO_4$ Characterisation

The range of different $LiCo_{1-x}Mn_xPO_4$ samples were mounted on a Bruker D2 Phaser powder X-ray diffractometer with a copper K_α X-ray source. **Figure 5.10** displays a stack plot of the different XRD patterns collected with the corresponding levels of manganese metal doping.

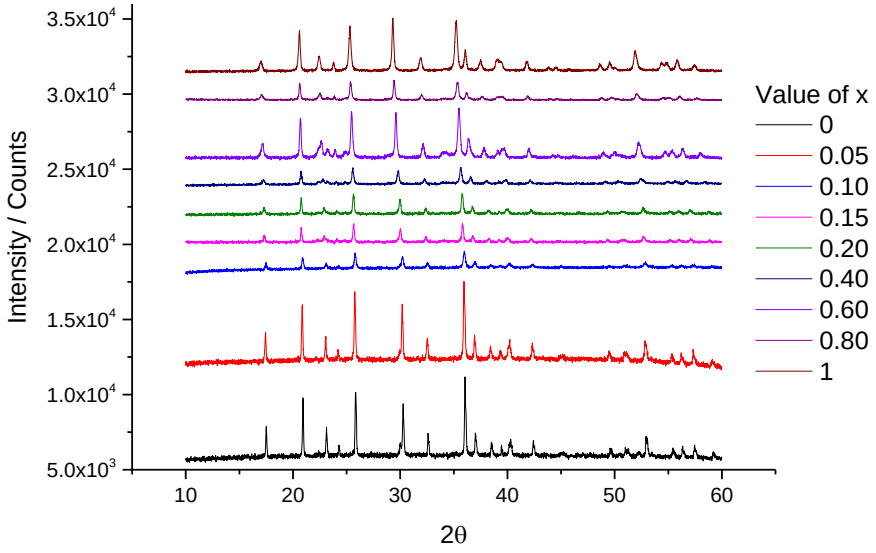

Figure 5.10 – XRD patterns of a range of x values in the series $LiCo_xMn_{1-x}PO_4$.

The range of different manganese doped powders were refined from Reitveld refinement. $LiCo_{0.40}Mn_{0.60}PO_4$ had an impurity of Li_3PO_4 present within the sample. **Figure 5.11** shows the $LiCo_{0.40}Mn_{0.60}PO_4$ refinement with the included also impurity fitted.

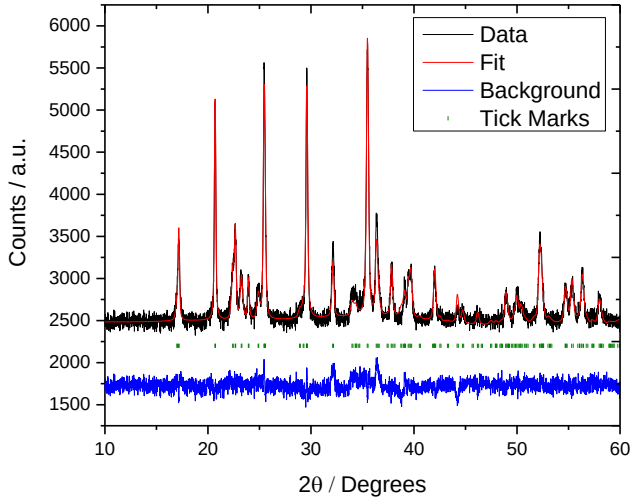

Figure 5.11 – X-ray diffractiogram of $LiCo_{0.40}Mn_{0.60}PO_4$ refined against $LiCoPO_4$ [18] and Li_3PO_4 [19] from the ICSD database. Lattice constants a = 10.36841(7) b = 6.04819(1) c = 4.73351(2), α = β = γ, wRp = 2.48 % Rp = 1.95 %.

Figure 5.12 shows each individual lattice parameter calculated from the refinement of the manganese doped samples across the series, as well as the overall lattice volume changes. A linear relationship can be seen across each lattice parameter, where a Vegard shift can be observed. Vegard's law is an approximate empirical rule which holds that a linear relation exists, at constant temperature, between crystal lattice constants of an alloy and the concentrations of the constituent elements.

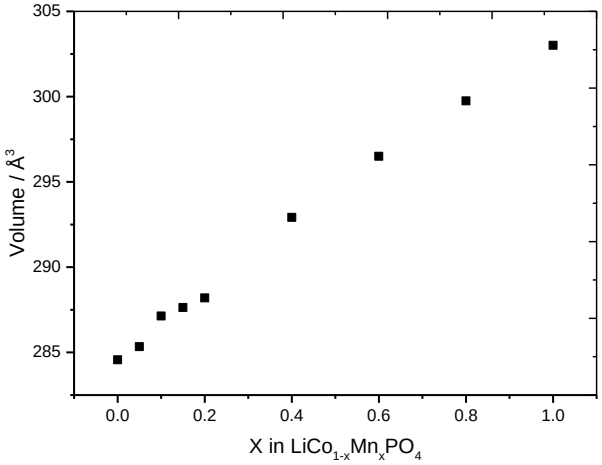

Figure 5.12 - Volume lattice changes across the $LiCo_{1-x}Mn_xPO_4$ series.

An example fit is shown in figure of $LiCo_{0.80}Mn_{0.20}PO_4$. The refinement was completed by adding in the majority phase that was present (in this case $LiCoPO_4$) and adding in an additional atom of manganese into the phase structure in the GSAS package. The occupancy was changed for each metal atom (Co = 0.80, Mn = 0.20) and constraints were added to the cobalt and manganese atoms so that they were refined together and have the same atom positions.

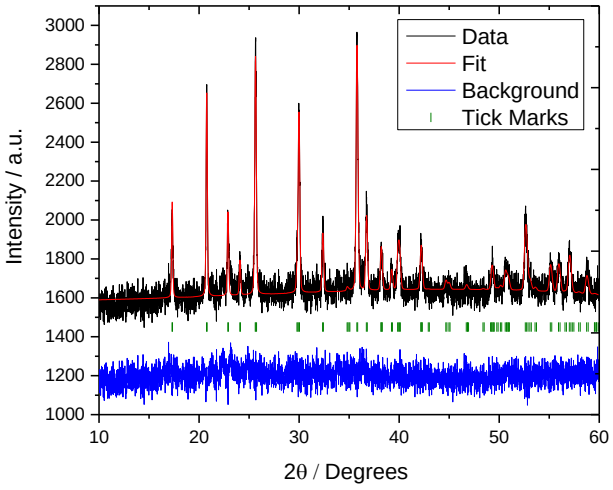

Figure 5.13 – X-ray diffractiogram of $LiCo_{0.80}Mn_{0.20}PO_4$ refined against $LiCoPO_4$ [18] and $LiMnPO_4$ [20] from the ICSD database. Lattice constants a = 10.25624(2) b = 5.96391(6) c = 4.71166(7), α = β = γ, wRp = 2.73 % Rp = 2.16 %.

5.5.4 $LiCo_{1-x}Mn_xPO_4$ Electrochemical Performance

Galvanostatic cycling was used to assess the electrochemical performance of manganese doped samples with a view of observing the discharge capacities obtained and the cyclability. **Figure 5.14** shows the charge and discharge capacities obtained from the initial cycle at 0.1 C.

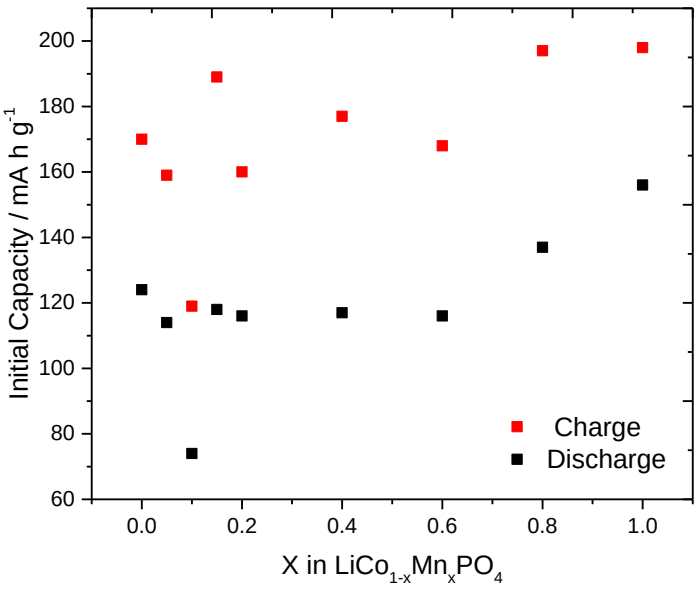

Figure 5.14 – Initial discharge capacities obtained for a range of $LiMn_xCo_{1-x}PO_4$ compositions cycled at 0.1 C using BASF LP57 electrolyte.

As manganese was substituted for cobalt across the series, the charge and discharge capacities generally increased. $LiMnPO_4$ produced a discharge capacity of 156 mA h g^{-1}, which is ~93 % that of the theoretical discharge. **Figure 5.15** shows the first initial cycle, along with the corresponding cycle life at 0.1 C. The cobalt and manganese plateaus matched well with the ratio levels of doping across the series, with the majority of the capacity obtained from the majority metal dopant within each composite electrode.

5.5.5 Initial Cycle of the $LiCo_{1-x}Mn_xPO_4$ Systems

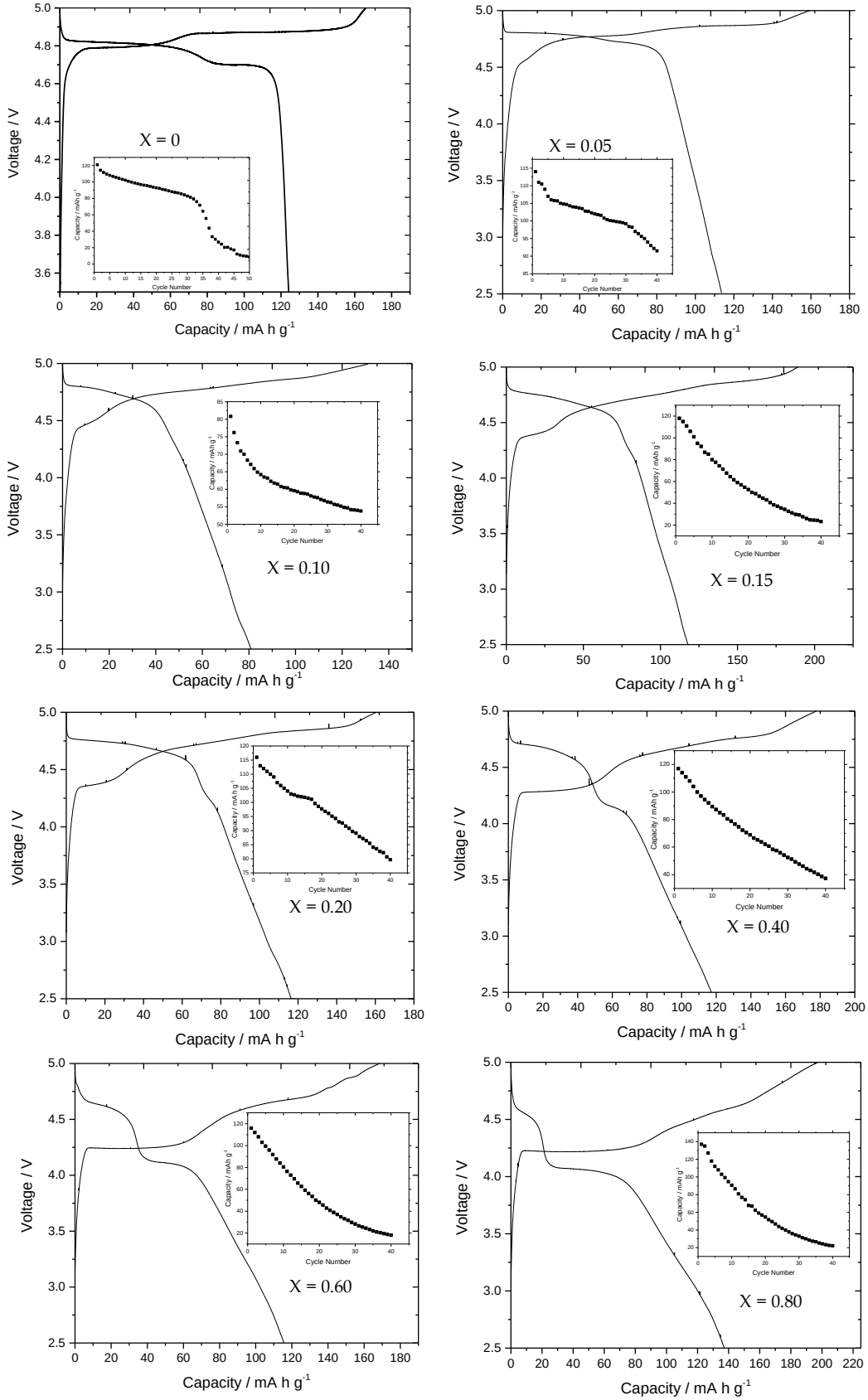

Figure 5.15 – Cycling data obtained for a range of $LiMn_xCo_{1-x}PO_4$ compositions cycled at 0.1 C using BASF LP57 electrolyte.

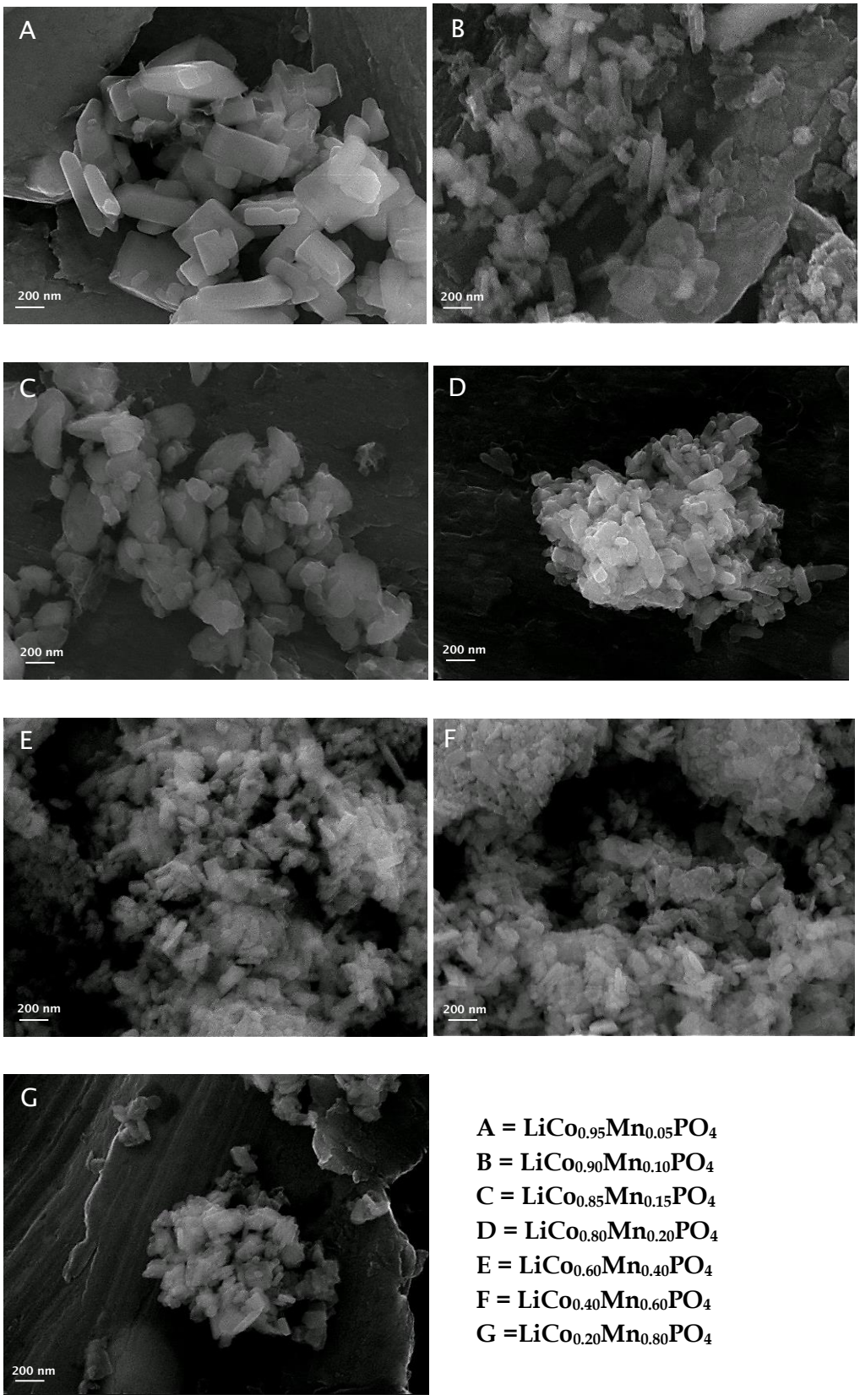

Figure 5.16 – SEM images obtained for a range of $LiMn_xCo_{1-x}PO_4$ particles.

As the levels of manganese content increased across the series, the morphology of the bulk of the particles changed from a rod-like shape to smaller nano-sized plates. Recent computational studies have shown that for olivine systems, the 010 surface plane is at a low energy, and was found to dominate the equilibrium morphology.[21] The exposure of the 010 surface on $LiFePO_4$ platelets is significant as it is the most facile pathway for lithium-ions in the *Pnma* system.[22] The SEM images obtained across the $LiCo_{1-x}Mn_xPO_4$ series may have preferred orientation along the 010 plane, which may explain why the initial capacities obtained were so high (as x increases).

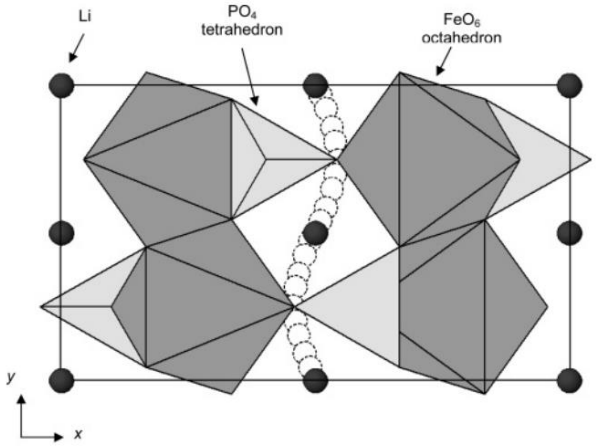

Figure 5.17 – Schematic of the calculated pathway for Li-ion migration down 010 channels of LiFePO4 viewed perpendicular to the *ab* plane. Reprinted with permission from reference.[23] Copyright 2005 American Chemical Society.

It is often assumed that a migrating ion takes the shortest pathway between adjacent sites (a direct linear jump), but detailed simulation analysis has suggested that lithium ions migrate through a wavelike trajectory which results in a lower migration energy than if the lithium ions followed a direct linear path.[23]

The cycle life decreased as more manganese was introduced into the system. The high voltage potential limits of 5 V *vs.* Li/Li^+ may have hindered the electrochemical performance of the nano-sized plates that were being formed; the platelets have a higher surface area than the rods, so the particles may have been exposed to more electrolyte breakdown on the surface which over time. This coupled with particle cracking and corrosion (as shown in **Section 5.2.2**) may explain why the cycle life was decreasing with increased manganese content.

The performance of $LiCo_{0.90}Mn_{0.10}PO_4$ was surprisingly low in terms of the initial discharge capacity obtained. **Figure 5.17** shows that there were large agglomerates formed of the active material which may have contributed to the low capacities obtained.

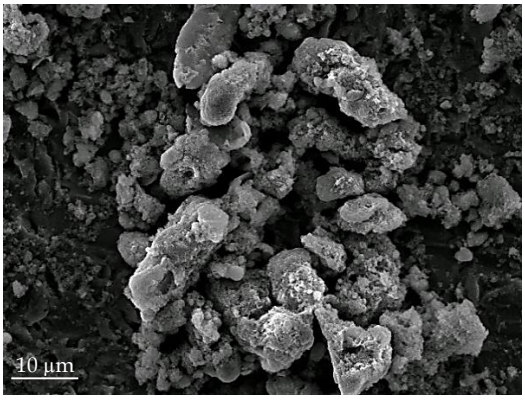

Figure 5.17 – SEM obtained of the $LiCo_{0.10}Mn_{0.90}PO_4$ particles.

5.5.6 $LiMnPO_4$

$LiMnPO_4$ operates at a higher potential than the popular $LiFePO_4$ but it's less used due to its poor conductivity and cycling behaviour. The poor cyclability has been linked to high levels of strain at the phase boundary between adjacent charged ($MnPO_4$) and discharged ($LiMnPO_4$) domains within a single crystallite, and this effect is larger in the manganese phase than for iron due to the Jahn-Teller distortion of the Mn^{3+} ions in $MnPO_4$.

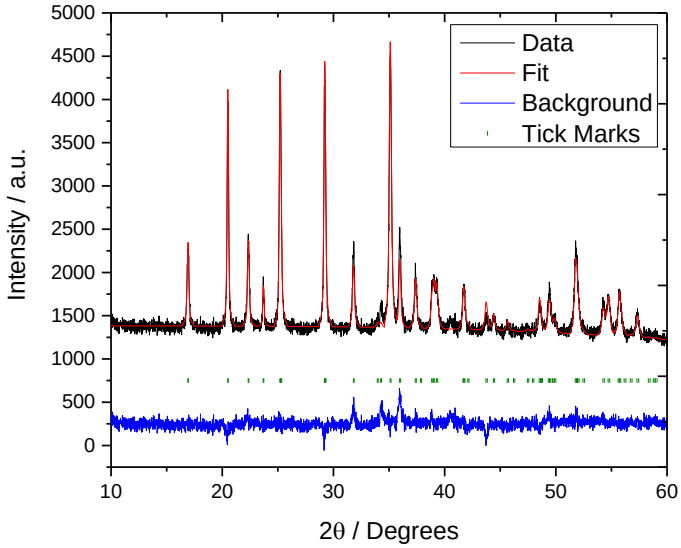

Figure 5.18 – X-ray diffractiogram of $LiMnPO_4$ refined from the ICSD database[20].
Lattice constants a = 6.10457(5) b = 10.45418(9) c = 4.74805(6), α = β = γ = 90°,
wRp = 3.53 % Rp = 2.72 %.

Figure 5.19 shows the SEM image obtained of the $LiMnPO_4$ particles along with the corresponding cycling data. Very thin nano-sized plates were obtained, which were well defined and consistent across the bulk material. A very high initial discharge capacity of 156 mA h g^{-1} was achieved at 0.1 C.

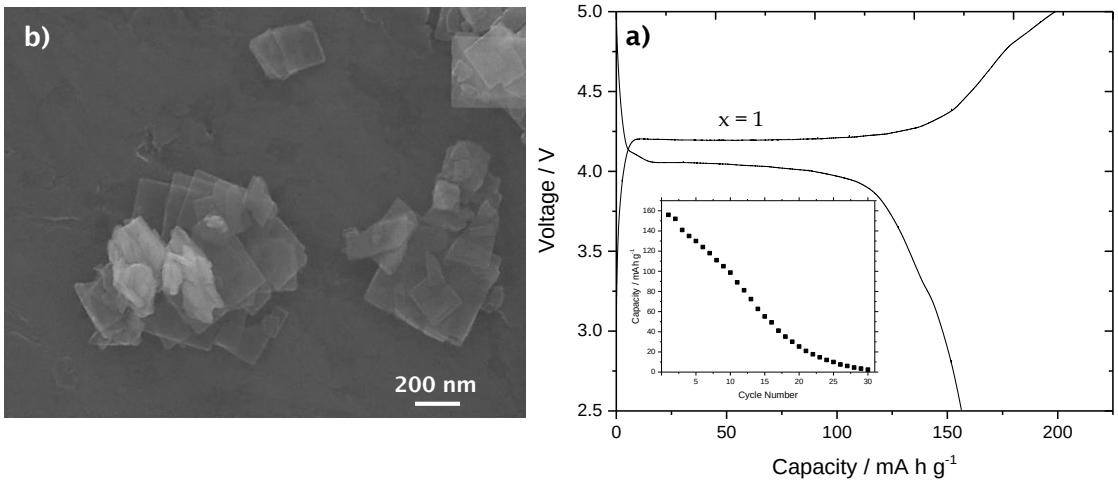

Figure 5.19 – SEM image and electrochemical performance of $LiMnPO_4$ 5 % carbon coated composite electrode in BASF LP57 at 0.1 C a) initial cycle b) cycling data.

On the initial cycle, a well-defined flat region is observed due to $LiMnPO_4$ undergoing a two phase transition during charge/discharge. The cycle life of the material however was poor. Very large capacity losses were observed from the initial cycle onwards. The large surface area of these very small particles would negatively contribute to the cycle life, as the large surface area would allow for a large amount of electrolyte to breakdown across the surface of the bulk material. Even at cycling to 4.5 V *vs.* Li/Li^+ and not the 5.0 V *vs.* Li/Li^+ window shown, the same cycling behaviour was observed.

5.5.7 $LiCo_{1-x}Mn_xPO_4$ Rate Testing

Rate testing was conducted on the $LiCo_{1-x}Mn_xPO_4$ series, using the same C-rate conditions as previously used within this report. Generally, the results suggest that as more manganese is doped into the material, less capacity can be achieved at higher C-rates. From the SEM images, it appears that more nano-plates are produced across the series as more manganese is doped into the structure. The nano-plates are smaller and thinner than the elongated particles formed when using $LiCoPO_4$, so a higher surface area can be assumed within the composite electrode as the manganese is doped across the series, leading to a poorer performance at higher C-rates due to more electrolyte breakdown at the surface and higher levels of particle corrosion.

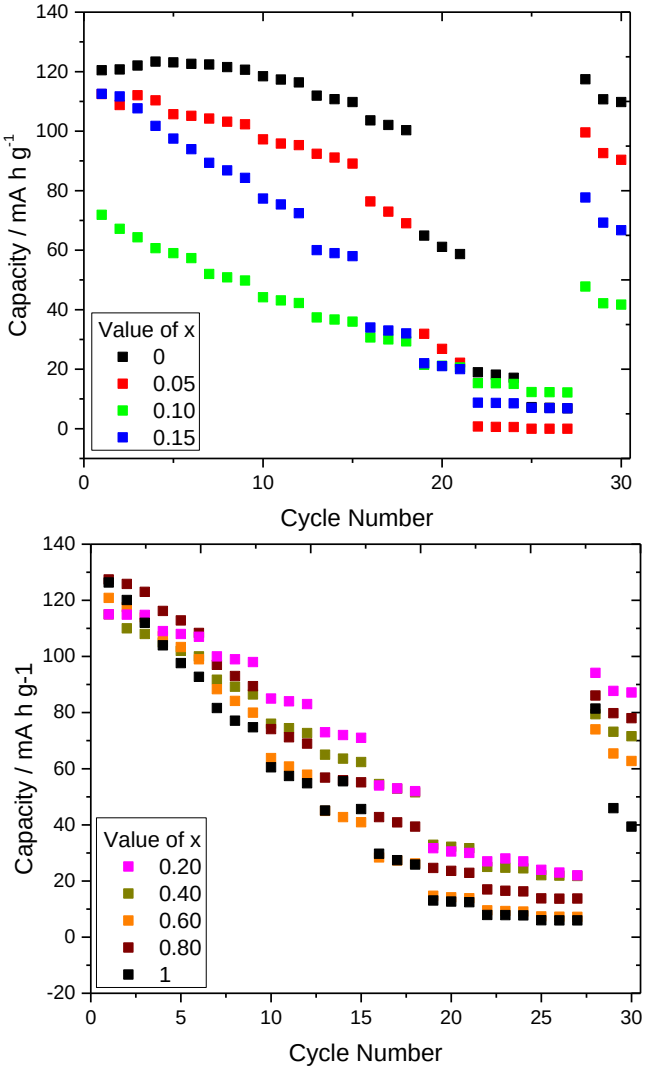

Figure 5.20 - Discharge capacities of different compositions of $LiCo_xMn_{1-x}PO_4$ charged at 0.1 C and discharged at various C-rates. Rate testing was conducted in a lithium half-cell with BASF LP57 1 M $LiPF_6$ EC:EMC (3:7) electrolyte.

5.6 References

1 G. Yan, X. Li, Z. Wang, H. Guo and C. Wang, J. Power Sources, 2014, **248**, 1306–1311.

2 Y.-M. Song, J.-G. Han, S. Park, K. T. Lee and N.-S. Choi, J. Mater. Chem. A, 2014, **2**, 9506.

3 M. Xu, N. Tsiouvaras, A. Garsuch, H. a. Gasteiger and B. L. Lucht, J. Phys. Chem. C, 2014, **118**, 7363–7368.

4 X. Zuo, C. Fan, J. Liu, X. Xiao, J. Wu and J. Nan, J. Electrochem. Soc., 2013, **160**, A1199–A1204.

5 E. Zygadło-Monikowska, Z. Florjańczyk, P. Kubisa, T. Biedroń, A. Tomaszewska, J. Ostrowska and N. Langwald, J. Power Sources, 2010, **195**, 6202–6206.

6 S. S. Zhang, J. Power Sources, 2007, **163**, 713–718.

7 A. M. Chockla, T. D. Bogart, C. M. Hessel, K. C. Klavetter, C. B. Mullins and B. A. Korgel, J. Phys. Chem. C, 2012, **116**, 18079–18086.

8 V. Etacheri, O. Haik, Y. Goffer, G. A. Roberts, I. C. Stefan, R. Fasching and D. Aurbach, Langmuir, 2012, **28**, 965–976.

9 M. Gauthier, D. Reyter, D. Mazouzi, P. Moreau, D. Guyomard, B. Lestriez and L. Roué, J. Power Sources, 2014, **256**, 32–36.

10 E. Markevich, G. Salitra, K. Fridman, R. Sharabi, G. Gershinsky, A. Garsuch, G. Semrau, M. A. Schmidt and D. Aurbach, Langmuir, 2014, **30**, 7414–24.

11 J.-G. Han, S. J. Lee, J. Lee, J.-S. Kim, K. T. Lee and N.-S. Choi, ACS Appl. Mater. Interfaces, 2015, **7**, 8319–8329.

12 Y.-K. Han, J. Yoo and T. Yim, J. Mater. Chem. A, 2015, **3**, 10900–10909.

13 V. Aravindan, Y. L. Cheah, W. C. Ling and S. Madhavi, J. Electrochem. Soc., 2012, **159**, A1435–A1439.

14 H. Shin, J. Park, A. M. Sastry and W. Lu, J. Electrochem. Soc., 2015, **162**, A1683–A1692.

15 K. Xu, J. Electrochem. Soc., 1998, **145**, L70.

16 X.-G. Sun and C. A. Angell, Electrochem. commun., 2005, **7**, 261–266.

17 M. Xu, N. Tsiouvaras, A. Garsuch, H. A. Gasteiger and B. L. Lucht, J. Phys. Chem. C, 2014, **118**, 7363–7368.

18 P. A, J. Pizarro, A. Goni, T. Rojo and M. Arriortua, 1998, An. Quim., **94**, 383–387.

19 C. Keffer, A. D. Mighell, F. Mauer, H. E. Swanson and S. Block, Inorg. Chem., 1967, **6**, 119–125.

20 S. Geller and J. L. Durand, Acta Crystallogr., 1960, **13**, 325–331.

21 L. Wang, F. Zhou, Y. S. Meng and G. Ceder, Phys. Rev. B, 2007, **76**, 165435.

22 M. S. Islam and C. A. J. Fisher, Chem. Soc. Rev., 2014, **43**, 185–204.

23 M. S. Islam, D. J. Driscoll, C. A. J. Fisher and P. R. Slater, Chem. Mater., 2005, **17**, 5085–5092.

Chapter 6:

In-situ XRD and XANES Analysis

6.1 Introduction

In-situ XRD studies on lithium insertion materials allow for the opportunity to study the desired electrode material whilst within the operating environment of the cell. The deconvolution of the crystal lattice during lithium insertion/extraction can be monitored constantly, allowing for direct comparisons to be made between the electrochemical features seen and any changes in the crystal structure that are recorded.

The number of *in-situ* structural studies of battery electrodes in real working cells is small. Typically they are carried out in transmission mode with coffee-bag type cells.[1] Within this chapter, a cell was used which has been designed previously and used successfully for *in-situ* studies on $LiFePO_4$.[2]

Within this chapter, the *in-situ* cells were cycled under galvanostatic and GITT conditions, specifically looking at the current pulses corresponding to lithium insertion/extraction and observing any structural relaxation during open circuit voltage. XANES data was also collected, in an attempt to monitor the cobalt metal redox centre during charge.

6.2 The *In-situ* Cell

The electrochemical *in-situ* cell used for this work is based on the commonly used Swagelok cell design. The aluminium foil doubled up as both the positive current collector and the X-ray window. The cell consists of three main sections as shown in **Figure 6.1**.

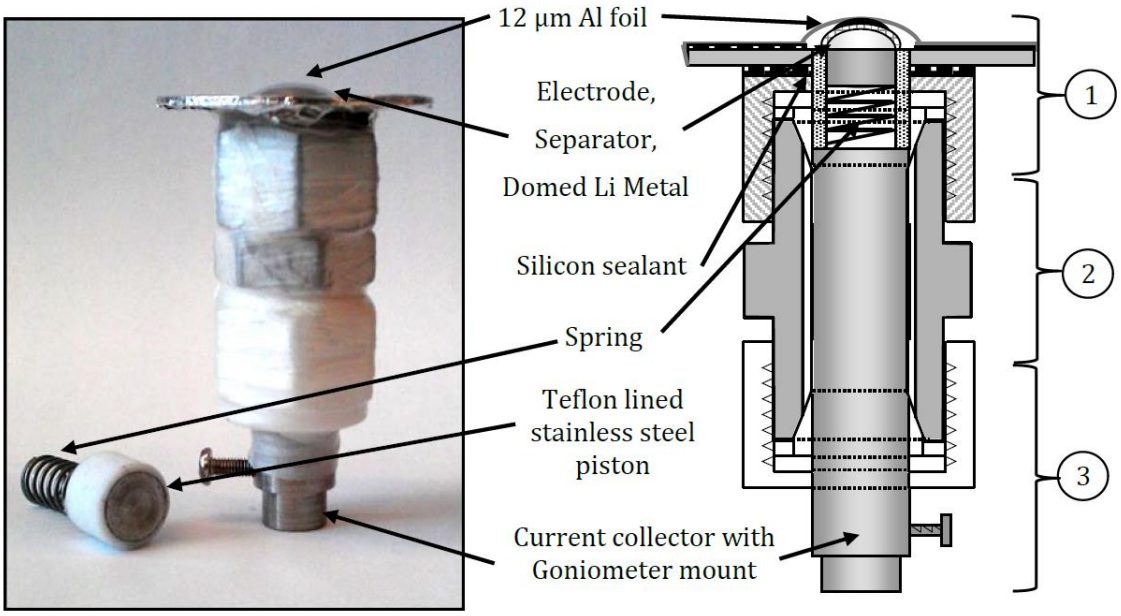

Figure 6.1 - Image and schematic of the *in-situ* electrochemical cell.

A 12 µm thick sheet of aluminium foil was glued onto the stainless steel support with black silicone rubber adhesive (Type 5910, Loctite). A 12.7 mm diameter stainless steel piston lined with a PTFE sheath (to avoid internal cell-shorting) was used as the current collector. Domed lithium was used as the negative electrode to allow for an even pressure to be applied across the stack when compressed via the spring.

The main body of the cell was a 12.7 mm diameter PTFE lined stainless steel connector with PTFE front and back ferrules used to seal the cell. To avoid external shorting when handling the cell, a PTFE nut was used for the lower part of the cell. A stainless steel rod was used as a connector to the negative electrode which was machined to fit into a standard goniometer head for mounting the cell onto the beamline. This was in turn mounted on an electrically insulated block so that the cell did not short via the instrument earthing.

6.3 Galvanostatic Cycling

Figure 6.2 shows the galvanostatic cycling of an *in-situ cell* containing $LiCoPO_4$ at 0.1 C using BASF LP57 electrolyte.

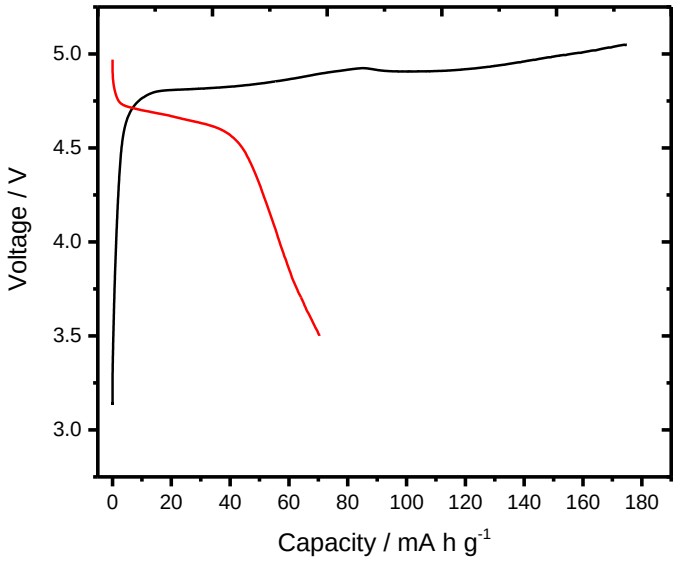

Figure 6.2 - Initial galvanostatic cycle data conducted in the lithium *insitu-cell* with BASF LP57 1 M $LiPF_6$ EC:EMC (3:7) electrolyte.

A charge capacity of ~180 mA h g^{-1} suggests that the majority of the lithium has been extracted. The charge voltage profile is less distinct than in a standard Swagelok cell, potentially due to loss of contact or a higher resistance within the *in-situ* cell. Upon discharge, the amount of capacity that was obtained was less than expected, strengthening further the possibility of loss of contact between the pellet and the separators.

Figure 6.3 shows a contour profile map tracing the peak intensity within a specific 2-theta range with XRD frame number (essentially with time). On charge, $LiCoPO_4$ undergoes a two two-phase transformation via an intermediate phase to obtain $CoPO_4$. Upon discharge, the reversible phase change transformations are observed, the peak intensities have been lost due to peak broadening from loss of long range order and poor discharge capacity. However the XRD patterns obtained follow the charge/discharge profile reasonably well suggesting the X-ray beam was being fired onto an electroactive region of the pellet.

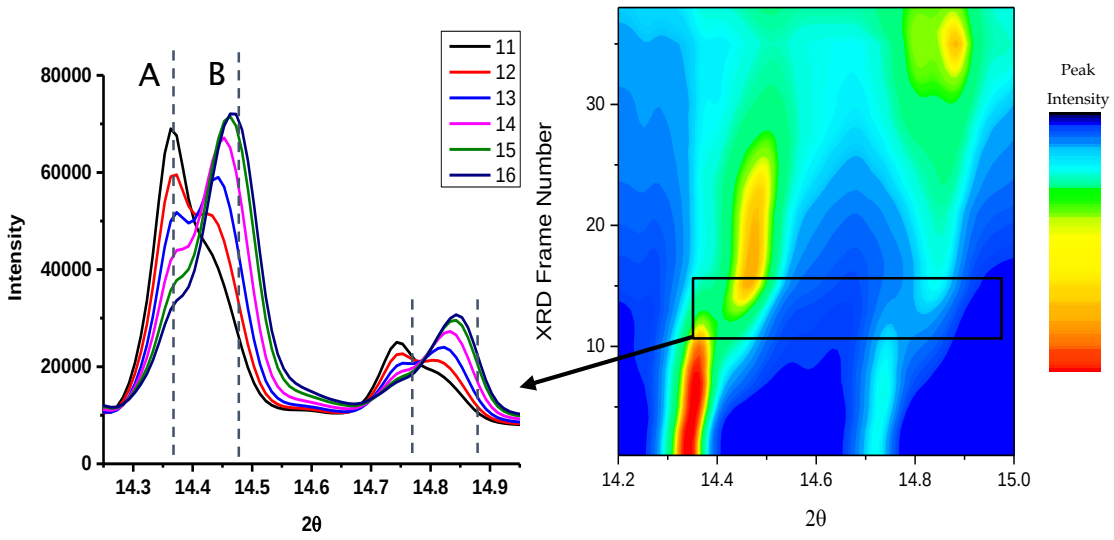

Figure 6.3 - Contour profile map of the collected galvanostatic data.

At the initial stage of charging, the lattice parameters of the $LiCoPO_4$ (phase A) are shifting to higher 2-theta values during lithium extraction. A shift to higher 2-theta values is expected as this indicates that the lattice parameters are shrinking. This shift continues until the concentration limits (in terms of lithium) are reached in the $LiCoPO_4$ phase, and then the new $Li_{2/3}CoPO_4$ (phase B) starts to grow after scan 14. During consumption of phase A, the peaks gradually diminish without a shift in the lattice parameters. However during the growth of the phase B, there is a clear Vegard shift in the peak positions to higher 2-theta values.

This Vegard shift suggests that there is a concentration gradient in $Li_{2/3}CoPO_4$ but not in the $LiCoPO_4$ phase during charge. The data suggests that a concentration gradient in $Li_{2/3}CoPO_4$ to extract lithium is a consequence of the diffusion field driving the interface into the middle of the particle prescribed by Fick's laws of diffusion.

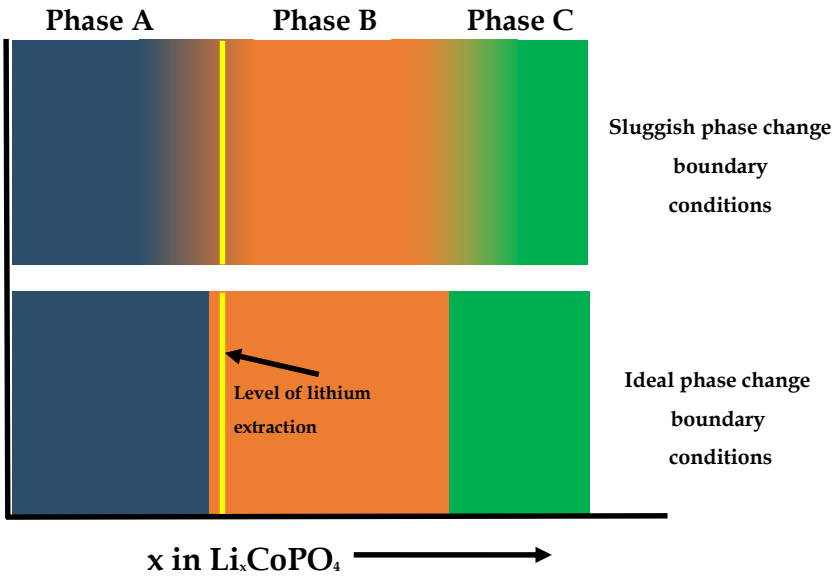

Figure 6.4 – Illustration to demonstrate how sluggish phase boundary conditions may leave to the co-existence of different phases.

The observed phases continuously changed lattice parameters suggesting the phase changes at the boundaries of A/B and B/C are so sluggish that even at these charge rates of 0.2 C there is still a co-existence of phases and significant variability in lattice parameters. This would be consistent with the observation of A, B and C present in some patterns.

Figure 6.5 displays the fitted lattice parameters of each different phase across the charge profile. The values were obtained from fitting each XRD pattern with GSAS. A two phase refinement was used, refining one phase first, before fixing these parameters to refine the other phase. The instrument parameters were fixed at all times, and were found from fixing a well-known crystalline reference sample. Phases A and B are very similar, and there is no known published structure of phase B, so they were fitted independently against the $LiCoPO_4$ phase. Phase A was fitted first, and then these values were fixed for the fitting of phase B. Phase C does have a known structure from theoretical calculations, so that was fitted against it.[3]

The lattice parameters decreased during charge, which was expected due to the extraction of lithium from the host lattice. Phase C has a small lattice volume compared to phases A and B, which has been known before from previous *in-situ* data.[4]

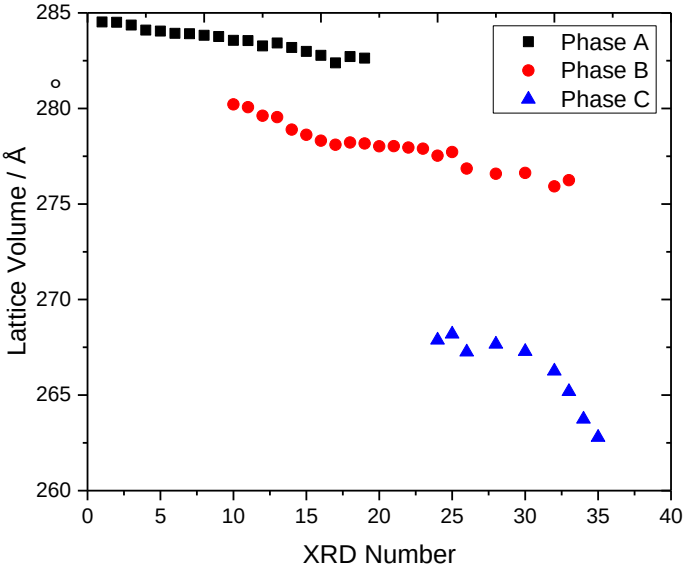

Figure 6.5 - Lattice parameters from the reitveld refinements of the galvanostatic charge data.

The lattice parameters of all three phases were shown to decrease upon lithium extraction. Phases A and B are relatively similar in lattice volume size compared to phase C. At the phase boundary condition of B/C the XRD patterns were very difficult to refine due to the existence of all three phases being present. The lattice parameters were observed to change by 1.0 % in phase A, 1.5 % in phase B and 2 % in phase C.

6.4 GITT Analysis of $LiCoPO_4$ in a Swagelok cell

An overpotential was required to observe a phase transformation in the *in situ* cell compared to a typical Swagelok cell. Only the transformation from $LiCoPO_4$ (phase A) to $Li_{2/3}CoPO_4$ (phase B) was observed at 5.1 V (which normally occurs at ~4.87 V), which indicates a high resistance from the *in-situ* cell. **Figure 6.6** shows the electrochemical data from the six pulses and the region the GITT charge profile is in in comparison to a full galvanostatic charge in a typical Swagelok cell.

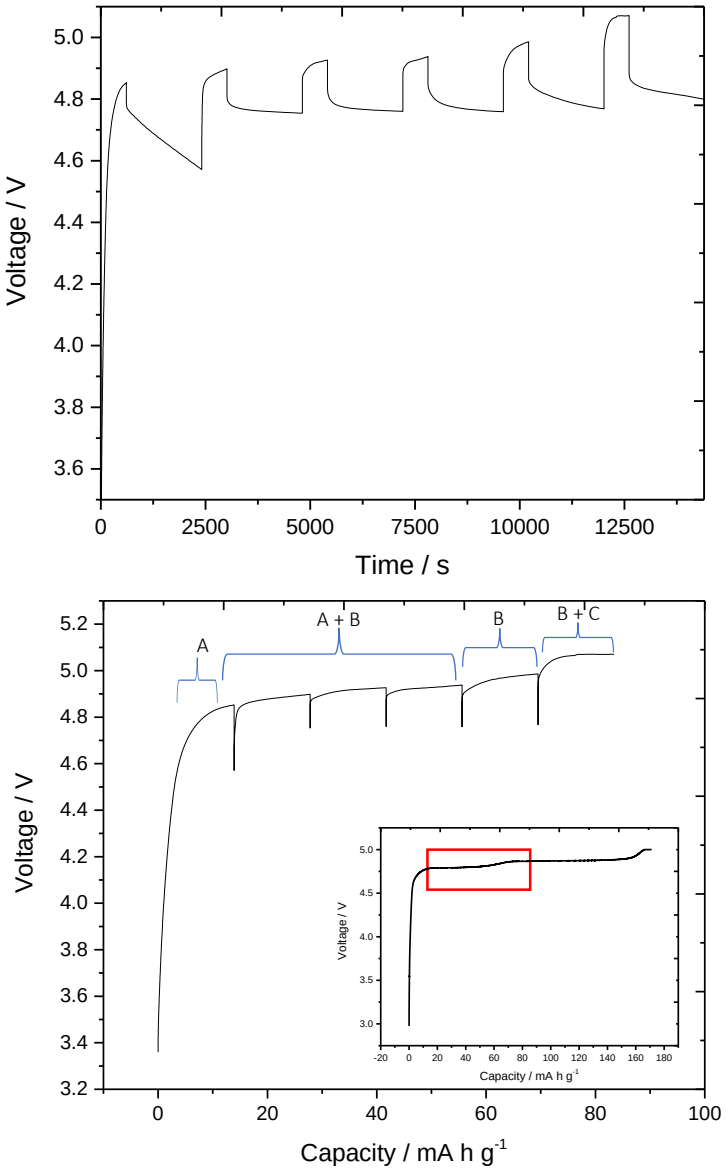

Figure 6.6 - Graphs showing the GITT data collected with respect to time, and the corresponding plot of the capacity observed. Conducted in the lithium *in-situ* cell with BASF LP57 1 M $LiPF_6$ EC:EMC (3:7) electrolyte.

The pulses were applied so that the current was on for 10 minutes with a 30 minute relaxation period (when the current is off). A rate equivalent of 0.5 C was applied when the current was turned on.

Figure 6.8 shows the XRD patterns monitoring the 020 reflection obtained during the 3rd, 4th, 5th and 6th pulse at 0.5 C (6 pulses in total). As before, the peaks shifted to higher 2θ values, but only during the pulses for lithium extraction. The growth of the $Li_{2/3}(Co^{2+})_{2/3}(Co^{3+})_{1/3}PO_4$ phase and depletion of $LiCoPO_4$ are indicated during the 3rd pulse, although the changes are partially reversed during the following relaxation. The new phase is more noticeably visible during the 4th pulse, while the $LiCoPO_4$ phase becomes completely depleted before the 5th pulse. During the regrowth of $LiCoPO_4$ phase with the current off, a Vegard shift of the peaks is observed, indicating a concentration gradient is required for movement of the diffusion boundary, as described earlier.

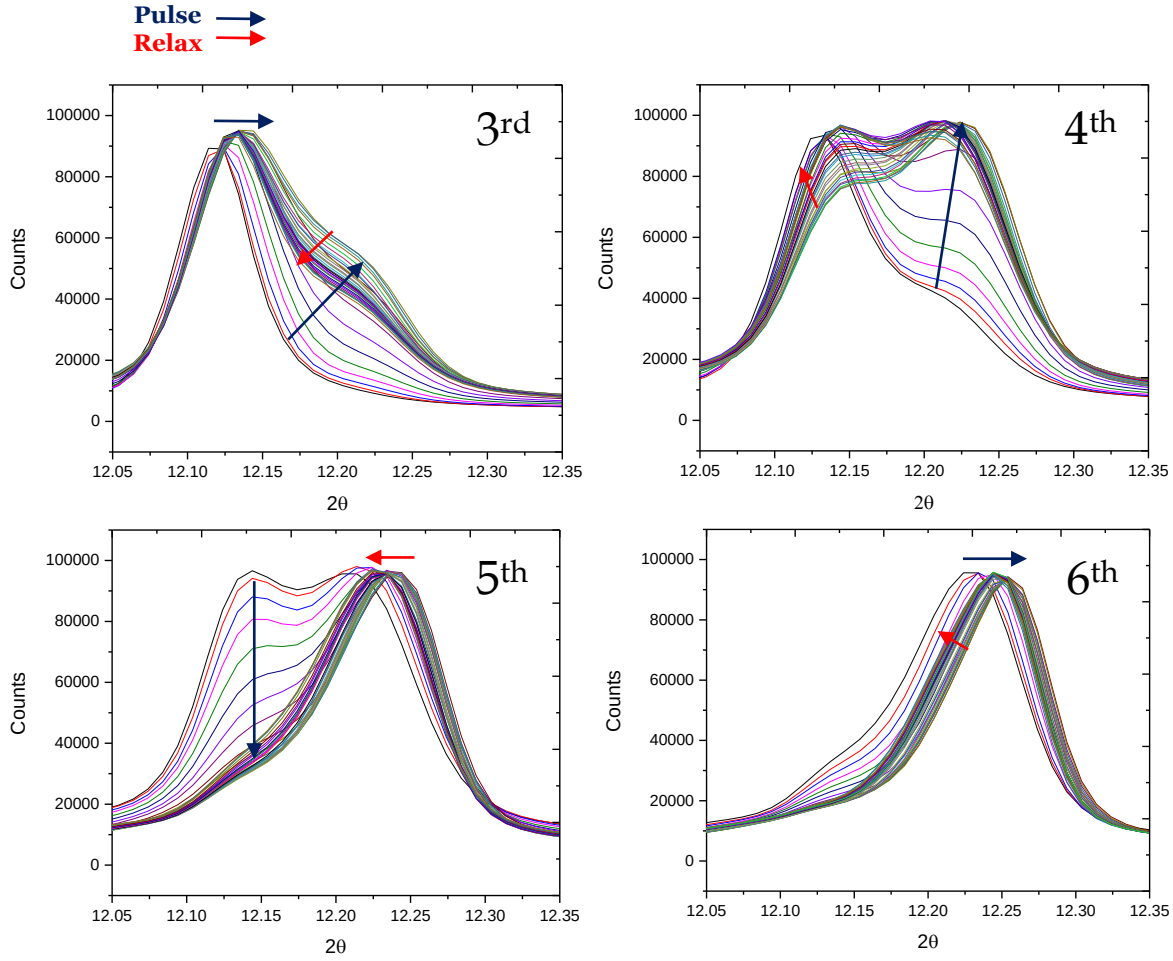

Figure 6.7 - Monitoring the peak positions of the 020 reflection on the 3rd, 4th, 5th and 6th pulse of the GITT data.

Figure 6.8 displays a contour profile map observing the peak position changes in the 020 plane across all 6 pulses on charge. The voltage profile has been overlaid, with the sections of charge highlighted. The graph shows that during the pulse (current on), phase A moves to higher 2θ values (indicating a lower lattice volume) until phase A reaches its concentration limits and the two phase boundary is reached and a phase B nucleates through continued pulsing. On relaxation, both phases should flatten out as both phases exist as they reach equilibrium. On pulse 6 a flat plateau is observed, indicating a two phase region, however the XRD patterns do not show the existence of phase C. The X-ray collection technique might not be sensitive enough to pick up the structural relaxations on the nanoscale that are occurring within a particle, however the electrochemistry directly measures the energy of the system and will be sensitive enough to pick up any phase changes in the nanoscale region.

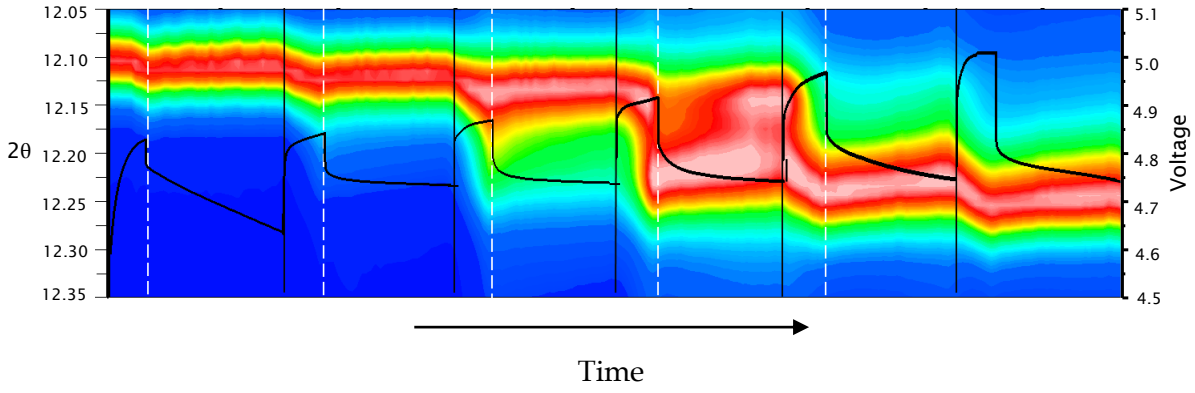

Figure 6.8 - contour profile map stitching the peak position changes of the 020 reflection with the voltage profile observed on charge.

The XRD patterns from the GITT data were then refined using Rietveld refinement, to monitor how the lattice parameters of phase A and B change during the charge pulsing. **Figure 6.9** display the results, along with the phase weight percentage fraction of each phase present within each XRD pattern. The lattice parameters decrease when the current is on (during pulse) and increase when the current is off (during the relaxation period).

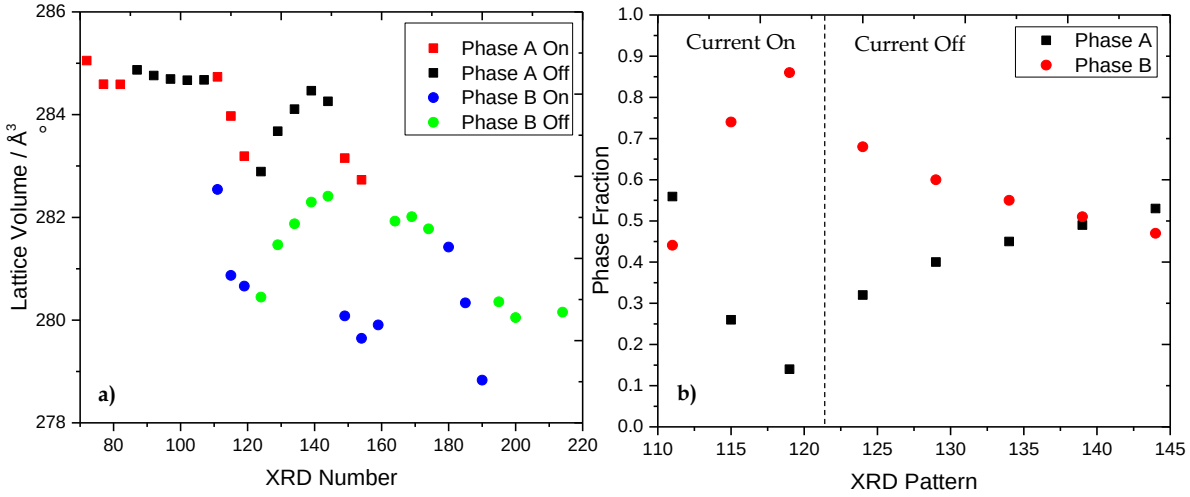

Figure 6.9 – a) Monitoring lattice parameters changes through the charge profile of the GITT data. b) Phase fraction of phases A and B through the 4th pulse. 'On' defines when the current was on and 'Off' defines when the current was off.

Figure 6.10 displays an example fit of the GITT data. The refinements were very difficult to fit to a high standard, as there were aluminium peaks to remove and difficulty obtaining a smooth background. The peaks were broad, and in some cases there was the existence of all three phases at once.

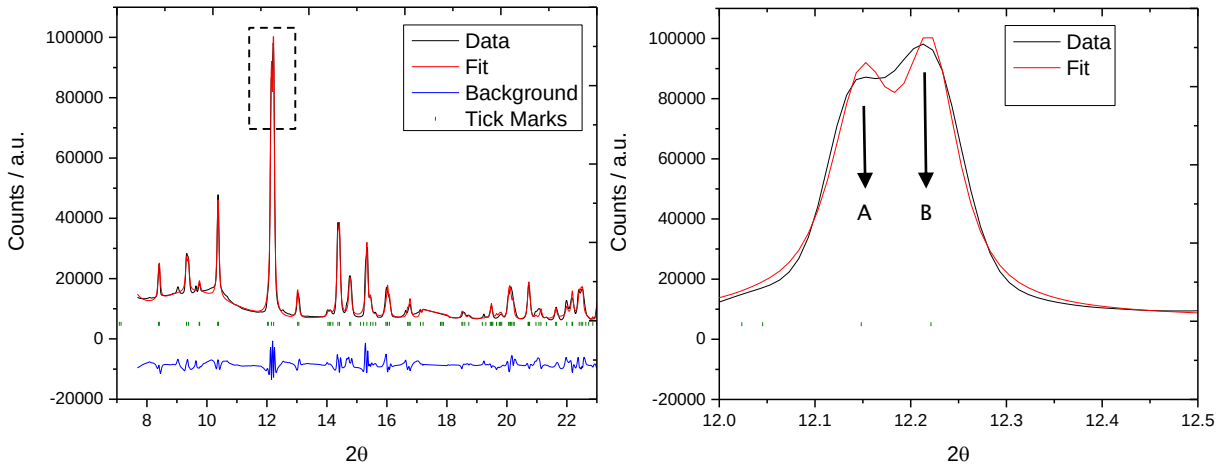

Figure 6.10 – Example fit of an XRD pattern with highlighted region magnified showing the peak positions of phase A and phase B.

6.5 XANES transmission measurements

6.5.1 Data analysis

The data was processed and analysed using a software program called ATHENA, which is part of the IFEFFIT software suite.[5] Within ATHENA, the raw data files can be normalised, calibrated and background subtracted, but for the XANES data only the normalisation step was required. To improve the signal-to-noise ratio, several scans for each measurement were merged using the sample processing parameters.

6.5.2 Ex-Situ $LiCoPO_4$

Ex-situ XANES spectra was collected from different $LiCoPO_4$ pellets that were charged to different potentials (**Figure 6.11**). The spectra was then compared to different cobalt standards of cobalt(II) oxide, cobalt(II,III) oxide and cobalt(III) acetate.

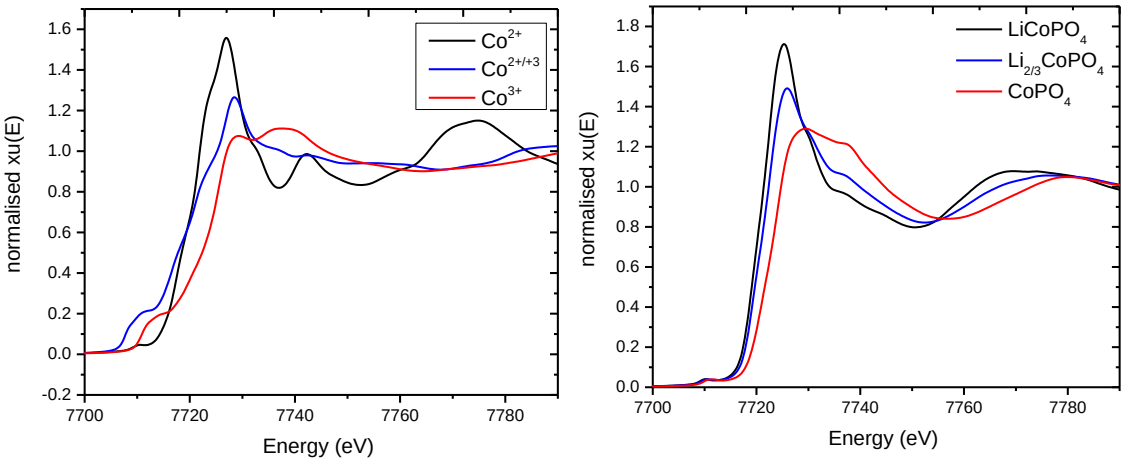

Figure 6.11 - Graphs displaying the collected XANES data. The graph on the left shows the results from the reference standards and the graph on the right shows the *ex-situ* XANES data from the composite electrode at different charge stages

XANES data was collected at 3.5 V, 4.87 V and 5.0 V *vs.* Li/Li^+. A shift to higher energies through the charging process was observed, indicating the oxidation of the cobalt metal centre from Co^{2+} to Co^{3+}.

6.6 References

1 H.-H. Chang, C.-C. Chang, H.-C. Wu, M.-H. Yang, H.-S. Sheu and N.-L. Wu, Electrochem. commun., 2008, **10**, 335–339.

2 M. R. Roberts, A. Madsen, C. Nicklin, J. Rawle, M. G. Palmer, J. R. Owen and A. L. Hector, J. Phys. Chem. C, 2014, **118**, 6548–6557.

3 H. Ehrenberg, N. N. Bramnik, A. Senyshyn and H. Fuess, Solid State Sci., 2009, **11**, 18–23.

4 M. Kaus, I. Issac, R. Heinzmann, S. Doyle, S. Mangold, H. Hahn, V. S. K. Chakravadhanula, C. Kübel, H. Ehrenberg and S. Indris, J. Phys. Chem. C, 2014, **118**, 17279–17290.

5 B. Ravel and M. Newville, J. Synchrotron Radiat., 2005, **12**, 537–541.

Chapter 7

Conclusions and Further Work

7.1 Conclusions

A wide range of initial high voltage materials were explored within this thesis, before focusing on $LiCoPO_4$ as a high voltage cathode material. $LiCoPO_4$ was synthesised and characterised within this report, and competitive capacities were given over a range of C-rates that are comparable with published literature. It was surprising to note that the material was active (at least initially) without the presence of a carbon coating. The plateaus obtained through galvanostatic cycling were well defined and could be assigned to the different expected processes occurring within the composite electrode.

A variety of different solvents were used within the solvo-thermal synthesis, and a range of different particle size and shapes were formed. The performance of these different particles could be related to a trade-off in terms of particle size and the surface area of the composite electrode. The best performing material was selected and further tests were attempted. The composite electrode that gave the best performance was a 75: 20: 5 ratio of $LiCoPO_4$: Carbon :PTFE, and the best performing composite electrode was with a 5 % coating of RuO_2, due to its high conductivity and stability.

Impedance was used to determine the origins of cycle life degradation, where it was found that large increases in the internal resistance of the cell directly related to the rapid decay in cycle life. It would be a rational argument to suggest that high voltage lithium-ion technology is limited by the electrolyte, and that a stable electrolyte with the important criteria of having a good ionic conductivity is a necessity to obtain good cycle life.

Different electrolytes were self-made in the lab and tested. The electrolytes were made up under dry conditions, and solvents were distilled when necessary. The electrolyte tests did show that the cyclability could be improved, but not to a significant standard. Minimising the HF content may have contributed to the improved performance, and also the production of a thin layer over the particles from electrolyte breakdown, however this has not been characterised and can only be maintained as speculation.

Manganese was then used to dope into the $LiCoPO_4$ across a $LiCo_{1-x}Mn_1PO_4$ series. A wide selection of compositions with varied stoichiometric ratios of cobalt:manganese was synthesised and tested. From this investigation, a promising cathode material,

$LiMnPO_4$ was produced which gave a very high discharge capacity at 0.1 C. The $LiMnPO_4$ particles were very well defined and consistent throughout the bulk material.

The experiments carried out at Diamond Light Source (UK synchrotron) proved to be successful, with important information extracted about the three different phases that are present during the charge profile of $LiCoPO_4$. The three phases were distinguishable and could be isolated during refinement fittings to produce reasonable lattice parameters that followed expected trends during the initial cycle. The different shifts in peaks seen could be related to lithium-ion shrinking core model theory, where the observation of phase B peaks shifting (in the galvanostatic cycling) due to the concentration gradient in terms of lithium being a consequence of the diffusion field driving the interface into the middle of the particle.

GITT data did show the progression of phase A into phase B during pulses. When the current was on, the depletion of A (within its concentration limits) occurred until the two phase boundary was reached, and a new phase was nucleated (phase B) during the pulse. During the relaxation, both phases should exist and begin to balance out as there is no driving force to remove lithium, which was observed.

7.2 Future Work

The impedance studies of the first cycle of $LiCoPO_4$ within this work need further studies. Going to much broader frequency ranges may give more insight into the processes occurring at slower frequencies. Collecting more than one cycle of the impedance data may also provide useful information as the SEI layer would have been stabilised from the first cycle and the impedance data may become less complex to analyse.

In depth Differential Electrochemical Mass Spectroscopy (DEMS) studies could be very useful investigating different electrolyte stabilities at high potentials. Different gaseous products produced from a battery could be detected, and analysed at different current rates. In order to detect if oxygen is being released from $LiCoPO_4$ the material could be heated in O^{18} and oxygen exchange may occur, so that if any O^{18} is detected then it must have come from the $LiCoPO_4$ structure.

Focussing on high voltage lithium containing cathode materials in general, there is still a limited understanding on what the SEI layers on particles consist of, and by what mechanisms they are formed. Information of how these breakdown products influence the battery performance are a crucial aspect that needs to be considered. There are many experimental techniques that can be used to examine the SEI layer, such as AFM (atomic force microscopy), FTIE (Fourier transform infrared spectroscopy) and XPS. *Ex-situ* XPS on cycled cathode pellets may shed some light on the breakdown products that may be produced on the surface of the electrode.

Electrolytes containing organic solvents have been shown to be unstable at high voltages. New generation electrolytes (other ionic liquids and additives) need to be considered, as well as solid state electrolytes (polymer electrolytes).

The in depth $LiCoPO_4$ analysis within this report has all been performed using PTFE binder, creating thin pellets of composite electrodes. It would be useful to analyse the data by preparing the electrodes through a commercially recognised ink method, using PVDF binder. The high levels of mixing may improve the homogeneity of the electrodes and could improve the battery performance.